



HORIZON 2020

HORIZON 2020 RESEARCH AND INNOVATION FRAMEWORK PROGRAMME OF THE EUROPEAN ATOMIC ENERGY COMMUNITY

Nuclear Fission and Radiation Protection 2018 (NFRP-2018-4)

Project acronym: **SANDA**
Project full title: **Solving Challenges in Nuclear Data for the Safety of European Nuclear facilities**
Grant Agreement no.: **H2020 Grant Agreement number: 847552**

Workpackage N°: **WP5**
Identification N°: **D5.7**
Type of document: **Deliverable**
Title: **Report on reactor and shielding C/E validation and nuclear data trends**
Dissemination Level: **PP**
Reference: **UPM/SANDA20240613**
Status: **VERSION 1.0**
Comments:

	Name	Partner	Date	Signature
Prepared by:	N. García-Herranz	UPM	18-06-2024	
WP leader:	R. Jacqmin	CEA		
IP Co-ordinator:	E. González	CIEMAT		

LIST OF AUTHORS

Nuria García Herranz	UPM
Oscar Cabellos	UPM
Antonio Jiménez Carrascosa	UPM ¹
David Bernard	CEA/DES
Ivo Kodeli	UKAEA/JSI
Gaspar Zerovnik	JSI
Steven van der Marck	NRG

ABBREVIATIONS AND ACRONYMS

ALFRED	Advanced Lead-cooled Fast Reactor European Demonstrator
ASTRID	Advanced Sodium Technological Reactor for Industrial Demonstration
CE	Continuous Energy
ESFR	European Sodium Fast Reactor
ESFR-SMART	European Sodium Fast Reactor Safety Measures Assessment and Research Tools
ESNII	European Sustainable Nuclear Industrial Initiative
FNS	Fusion Neutron Source
ICSBEP	International Criticality Safety Benchmark Evaluation Project
IRPHEP	International Reactor Physics Evaluation Project
ISC	Integrated Sensitivity Coefficients
JEFF	Joint Evaluated Fission and Fusion
LWR	Light Water Reactors
MG	Multi Group
MOX	Mixed OXide
MYRRHA	Multi-purpose Hybrid Research Reactor for High-tech Applications
PIE	Post-Irradiation Experiments
PNFS	Prompt Fission Neutron Spectra
PWR	Pressurized Water Reactor
SDF	Sensitivity Data File
SEFOR	South-West Experimental Fast Oxide Reactor
SINBAD	Shielding Integral Benchmark Archive and Database
SFR	Sodium-cooled Fast Reactor
S/U	Sensitivity and Uncertainty
TOF	Time-of-Flight
TSL	Thermal Scattering Libraries
WPEC	Working Party on International Nuclear Data Evaluation Co-operation

¹ Paul Scherrer Institute (PSI) since March 2023.

EXECUTIVE SUMMARY

This Deliverable 5.7 of the EC SANDA project “Supplying Accurate Nuclear Data for Energy and non-Energy Applications” (H2020 Grant Agreement number 847552) addresses Task 5.2 “Validation studies using existing experiments”, Subtask 5.2.2 “*C/E* validation and trends”. It reports on validation of JEFF nuclear data files by comparing Calculations (*C*) with experimental measurements (*E*) for reactor physics experiments and shielding benchmarks, encompassing representative experiments from different facilities, neutron spectra, and integral quantities of interest. Integral experiments have been mainly sourced from IRPhEP, ICSBEP and SINBAD international databases, although other legacy experiments have also been examined. Concerning reactors, the selected benchmarks cover advanced LMFR reactors, thermal experimental reactors and commercial Light-Water Reactors. Regarding shielding benchmarks, Time-of-Flight integral benchmarks and neutron transmission experiments are examined.

Systematic use of JEFF-3.3 and new evaluations as they have become available has been done, including the recently JEFF-4T3 test evaluation. Comparison between benchmark values and calculated values show in general improved performance with JEFF-4T3 compared to JEFF-3.3. Conclusions on validation and nuclear data trends are included in Deliverable D5.9 which compiles findings related to *C/E* validation across reactor, shielding and criticality benchmarks.

KEYWORDS

JEFF; nuclear data validation; advanced fast reactors; thermal reactors; commercial PWR; shielding benchmarks; weighted bias; perturbation analysis; nuclear data trends

Table of contents

LIST OF AUTHORS	2
ABBREVIATIONS AND ACRONYMS.....	2
EXECUTIVE SUMMARY.....	3
KEYWORDS	3
TABLE OF CONTENTS.....	1
LIST OF TABLES.....	2
LIST OF FIGURES	3
1. INTRODUCTION	7
2. CONSIDERATIONS ABOUT METHODOLOGIES FOR NUCLEAR DATA VALIDATION.....	7
2.1. METRICS FOR EVALUATING BIASES	8
2.2. CODES EMPLOYED FOR VALIDATION	9
3. ADVANCED FAST REACTORS <i>C/E</i> VALIDATION AND NUCLEAR DATA TRENDS (UPM)	10
3.1. EXPERIMENTAL DATABASE BASED ON SIMILARITY INDEXES.....	10
3.2. ANALYSIS OF FAST-SPECTRUM SELECTED BENCHMARKS FROM ICSBEP AND IRPHEP	13
3.3. ANALYSIS OF SEFOR EXPERIMENTS	22
4. THERMAL REACTORS <i>C/E</i> VALIDATION AND NUCLEAR DATA TRENDS (UPM, NRG)	27
4.1. ANALYSIS PERFORMED AT UPM: KRITZ BENCHMARKS.....	27
4.2. ANALYSIS PERFORMED AT NRG: CREOLE AND KRITZ BENCHMARKS.....	34
5. COMMERCIAL LIGHT WATER REACTORS <i>C/E</i> VALIDATION AND NUCLEAR DATA TRENDS.....	37
5.1. ANALYSIS OF THE CRITICAL BORON LETDOWN CURVE (UPM)	37
5.2. ANALYSIS OF POST-IRRADIATION EXPERIMENTS (CEA/DES)	41
6. SHIELDING BENCHMARKS <i>C/E</i> VALIDATION AND NUCLEAR DATA TRENDS	45
6.1. SHIELDING BENCHMARKS FOR VALIDATION OF IRON EVALUATIONS (JSI/UKAEA).....	45
6.2. KFK γ -RAY LEAKAGE BENCHMARK (JSI/UKAEA).....	48
6.3. SHIELDING TIME-OF-FLIGHT BENCHMARKS IN SINBAD: OKTAVIAN AND FNS (UPM)	51
6.3.1. <i>FNS/TOF</i>	52
6.3.2. <i>OKTAVIAN</i>	58
6.4. NEUTRON TRANSMISSION EXPERIMENTS IN ICSBEP: FUND-JINR-1/E-MULT-TRANS-001 (UPM).....	63
7. SUMMARY AND CONCLUSIONS	65
8. ACKNOWLEDGEMENTS	65
9. REFERENCES	66

List of Tables

Table 1. Selected integral experiments in ICSBEP database useful for SFR validation.	12
Table 2. Selected experiments in IRPhEP useful for LMFR validation.	13
Table 3. Other selected experiments useful for LMFR validation: SEFOR experiments.	13
Table 4. Metrics for nuclear data library performance for the ICSBEP benchmark dataset.....	17
Table 5. Metrics for nuclear data library performance for the IRPhEP benchmark dataset.....	17
Table 6. Main contributors to deviations of multiplication factors between JEFF-3.3 and JEFF-3.1.1 for MIX-COMP-FAST experiments series. Energy-integrated isotope-reaction contribution to $\Delta k/k$ (in pcm).....	18
Table 7. Main contributors to deviations of multiplication factors between JEFF-3.3 and JEFF-3.1.1 for selected LMFR arrangements. Energy-integrated isotope-reaction contribution to $\Delta k/k$ (in pcm).....	19
Table 8. Main contributors to deviations of sodium void effect between JEFF-3.3 and JEFF-3.1.1 for selected LMFR arrangements. Energy-integrated isotope-reaction contribution to $\Delta\rho/\rho$ (in%).....	19
Table 9. Analysis of differences between JEFF-4T3 and ENDF/B-VII.1 for SNEAK configurations.....	20
Table 10. Results for SEFOR Doppler benchmark for Core II-E (R-Z model). Doppler effect from 677 K to 1365 K....	23
Table 11. Results for SEFOR Doppler benchmark for Core I-E (Detailed model). Doppler effect from 449K to 677K.24	24
Table 12. EALF values (keV) as reflector segment is moving upward.	26
Table 13. Summary of analyzed KRITZ-LWR-RESR- benchmarks.	27
Table 14. Summary of results for KRITZ-2:19 (KRITZ-LWR-RESR-001) and C/E biases	28
Table 15. Summary of results for KRITZ-2:1 (KRITZ-LWR-RESR-002) and C/E biases	29
Table 16. Summary of results for KRITZ-2:13 (KRITZ-LWR-RESR-003) and C/E biases	29
Table 17. Uncertainties in keff (in pcm) due to ND uncertainties in ^{235}U , ^{238}U and ^{239}Pu (except for nubar and PFNS) for JEFF-3.3 (J33) and ENDF/B-VIII.0 (E80)	29
Table 18. Δkeff due to perturbations in nuclear data (J33/E71) data for KRITZ4/Case25 and Case27.....	32
Table 19. Δkeff due to perturbations in nuclear data (E80/E71) data for KRITZ4/Case25 and Case27.....	33
Table 20. Δkeff due to perturbations in nuclear data (J33/J311) data for KRITZ4/Case25 and Case27	33
Table 21. Results for the fitted trend of C-E reactivity values for CREOLE-PWR-EXP-001.	35
Table 22. Results for the fitted trend of C-E reactivity values for kritz-lwr-resr-001 through -004.	36
Table 23. Biases (C/E) of isotopic concentrations using JEFF-x libraries (fluences are estimated by using each nuclear data library, i.e. respective to their own neodymium fission yields).....	43
Table 24. Summary of analyzed SINBAD benchmarks for validation of iron evaluations.	45
Table 25. Computational nuclear data uncertainties vs. measurement uncertainties for ASPIS-Iron88.....	48
Table 26. Computational nuclear data uncertainties vs. measurement uncertainties for PCA Replica.	48
Table 27. KFK benchmark: contribution of neutron-induced gammas and ^{252}Cf gamma source terms to the 0.5 - 2 MeV gamma flux in the detector for the spheres of different radii.	50
Table 28. Uncertainty in the 0.5 to 2 MeV gamma flux due to the uncertainty in ^{252}Cf PFNS and prompt and delayed gamma source spectra.	51
Table 29. FNS-ToF Benchmarks (17 cases x 5 angles)	52
Table 30. OKTAVIAN ToF Benchmarks (15 cases) Ref.: F. Maekawa et al., Collection of Exper. Data for Fusion Neutronics Benchmark, JAERI, 1994.	59
Table 31. Samples of highly enriched uranium for FUND-JINR-1/E-MULT-TRANS-001: 235U.....	63

List of Figures

Figure 1. Similarity matrix between the ICSBEP dataset and the selected SFR designs, for the multiplication factor.	11
Figure 2. Similarity matrix between the IRPhEP dataset and the selected SFR designs, ESFR and ASTRID, for the multiplication factor.....	11
Figure 3. Similarity matrix between the IRPhEP dataset and the selected SFR designs, ESFR and ASTRID, for the sodium voiding effect.....	12
Figure 4. Illustration of reactor experiments in used for SFR validation.....	14
Figure 5. Computational biases in k-eff for the selected ICSBEP integral benchmark datasets (uncertainties account for both evaluated benchmark uncertainties and Monte Carlo statistical errors).	15
Figure 6. Computational biases in k-eff for the selected IRPhEP reactor physics benchmarks (uncertainties account for both evaluated benchmark uncertainties and Monte Carlo statistical errors).	15
Figure 7. Computational biases in reactivity effects for the selected IRPhEP reactor physics benchmarks (uncertainties account for both evaluated benchmark uncertainties and Monte Carlo statistical errors).	16
Figure 8. Comparison of C-E biases in the multiplication factor for JEFF-4T3 to nuclear data induced-uncertainties due to JEFF-3.3 covariance data.....	16
Figure 9. Comparison of C-E biases in reactivity effects for JEFF-4T3 to nuclear data induced-uncertainties due to JEFF-3.3 covariance data.	17
Figure 10. Sensitivity profiles for SNEAK configurations. Differences in the ^{238}U elastic cross section and angular distributions in JEFF-4T3 and ENDF/B-VII.1	20
Figure 11. Biases in ZPPR-2 experiments with different quantities of sodium removed.	21
Figure 12. Main sensitivity profiles for sodium void (left) and multiplication factor (right) for ZPPR-2.	21
Figure 13. Sensitivity profile for ZPPR-2 sodium void to Pu-239 capture, ratio of the Pu-239 capture between JEFF-3.3 and JEFF-3.1.1 and impact of the perturbation on the sodium void worth.	22
Figure 14. Schematic top view of SEFOR Core I-E (left) and KENO-VI model (right).	23
Figure 15. Schematic top view of Sensitivity of Doppler effect to ^{238}U (n,γ).....	24
Figure 16. Perturbation of ^{238}U (n,γ) cross sections between JEFF-3.3 and JEFF-3.1.1.	24
Figure 17. Change in Doppler reactivity due to the ^{238}U (n,γ) perturbation.	24
Figure 18. ^{238}U (n,γ) cross sections in the range around 800 eV.	25
Figure 19. C/E for reflector worth in SEFOR Core I-E configuration.	25
Figure 20. Calibration curves for movable fine reflector R3 in SEFOR Core I-E configuration. Initial position of reflector corresponds to 0 cm (left) and 8.73 cm (right).	26
Figure 21. Schematic top and side views of the KRITZ core [Kodeli, 2009].....	28
Figure 22. KRITZ-2:19 sensitivity coefficients (left).	29
Figure 23. Relative standard deviation for ^{239}Pu (n,γ).	30
Figure 24. Relative Schematic top and side views of the core are presented [Mennerdahl, 2020]	31
Figure 25. C/E for KRITZ4/Series1.	31
Figure 26. C/E for KRITZ4/Series2	31
Figure 27. C/E for KRITZ4/Series3	31
Figure 28. C/E for KRITZ4/Series4	31
Figure 29. Sensitivity analysis in KRITZ4/Series4 – Case 25 and Case 37. Ratios of $^{235}\text{U}(n,f)$ cross sections in JEFF-3.3 and ENDF/B-VIII.0 with respect to ENDF/B-VII.1 (top) and sensitivity profiles of the multiplication factor to $^{235}\text{U}(n,f)$ for Cases 25 and 37.	33
Figure 30. Cumulative Δk_{eff} plot for KRITZ4/Series4 – Case 25 and Case 37.	34
Figure 31. Input model for CREOLE.	35
Figure 32. Results with JEFF-4T3 for CREOLE benchmark.	35
Figure 33. Results for KRITZ benchmark.	36
Figure 34. Boron letdown in a typical 1000MWe Westinghouse-type PWR, cycle 5.....	37
Figure 35. Difference (Calculated – Measurement) in critical Boron let-down in a typical 1000MWe Westinghouse-type PWR, cycle 5, for different libraries (ENDF/B-VIII.0 is highlighted).....	38
Figure 36. Critical boron modifications (in ppm) at reactor level. Calculations performed with SEANAP system (COBAYA/2D code) for a typical 1000MWe- PWR Westinghouse.	38
Figure 37. Critical boron differences “Experimental – Calculation” (in ppm) for the Almaraz II, Cycle 1. Calculation performed with SEANAP system.	39
Figure 38. Critical boron modifications (in ppm) in NPP Almaraz II, cycle 1. Calculations performed with COBAYA/2D code.....	39

Figure 39. Critical boron modifications (in ppm) in NPP Almaraz II, cycle 1. Calculations performed with COBAYA/2D code.....	40
Figure 40. Critical boron modifications (in ppm) in NPP Almaraz II, cycle 1. Calculations performed with COBAYA/2D code.....	40
Figure 41. Modification reactivity (in pcm) in a typical PWR Fuel Assembly 17x17 at 4.8w/o. Calculations performed with WIMSD5b lattice code.	41
Figure 42. Modification reactivity (in pcm) in typical PWR Fuel Assembly 17x17 at 4.8w/o. Calculations performed with WIMSD5b lattice code.	41
Figure 43. Sketch of the radial position of the analyzed fuel rods.....	42
Figure 44. Sketch of the axial position of the analyzed rod cuts.....	42
Figure 45. Biases C/E in S(n,p) for ASPIS Fe-88.	46
Figure 46. Biases C/E in Al(n,a) for ASPIS Fe-88.	46
Figure 47. Biases C/E in S(n,p) for PCA Replica.	46
Figure 48. Biases C/E in Al(n,a) for PCA.....	46
Figure 49. Biases C/E for reaction rates measured in ASPIS Fe-88 benchmark obtained using recent nuclear data.	47
Figure 50. Sensitivities for ASPIS Fe-88.	47
Figure 51. Sensitivities for PCA.....	47
Figure 52. Sensitivities for PCA Replica.	48
Figure 53. KFK set-up and ²⁵² Cf source.....	49
Figure 54. Comparison between the measured neutron and gamma spectra from KFK iron spheres of different diameters and those calculated using the MCNP and PARTISN codes and FENDL-3.2a nuclear data. Note that electrons were not transported in MCNP.	49
Figure 55. KFK set-up: Sensitivity of the total gamma flux to the ⁵⁶ Fe elastic and inelastic neutron cross sections and to the incoherent gamma scattering data for iron spheres with the radius of 12.5, 15, and 17.5 cm.....	50
Figure 56. Screen-shot SG47 GitLab showing UPM Suite of OKTAVIAN and FNS Benchmarks.....	51
Figure 57. FNS/TOF setup	52
Figure 58. Angular neutron leakage spectra at 0 degrees for the 5CM(Z) FNS-TOF iron FNS-TOF experiment: JEFF-4T2.	53
Figure 59. Angular neutron leakage spectra at 0 degrees for the 20CM(Z) FNS-TOF iron FNS-TOF experiment: JEFF-4T2.	53
Figure 60. Angular neutron leakage spectra at 0 degrees for the 40CM(Z) FNS-TOF iron FNS-TOF experiment: JEFF-4T2.	53
Figure 61. Angular neutron leakage spectra at 0 degrees for the 60CM(Z) FNS-TOF iron FNS-TOF experiment: JEFF-4T2.	53
Figure 62. Angular neutron leakage spectra at 0 degrees for the 5CM(Z) FNS-TOF iron FNS-TOF experiment: ENDF/B-VIII.1b2.	53
Figure 63. Angular neutron leakage spectra at 0 degrees for the 20CM(Z) FNS-TOF iron FNS-TOF experiment: ENDF/B-VIII.1b2.	53
Figure 64. Angular neutron leakage spectra at 0 degrees for the 40CM(Z) FNS-TOF iron FNS-TOF experiment: ENDF/B-VIII.1b2.	54
Figure 65. Angular neutron leakage spectra at 0 degrees for the 60CM(Z) FNS-TOF iron FNS-TOF experiment: ENDF/B-VIII.1b2.	54
Figure 66. Angular neutron leakage spectra at 0 degrees for the 5.08CM(Z) FNS-TOF beryllium FNS-TOF experiment: : JEFF-4T2.....	54
Figure 67. Angular neutron leakage spectra at 0 degrees for the 15.24CM(Z) FNS-TOF beryllium FNS-TOF experiment: : JEFF-4T2.....	54
Figure 68. Angular neutron leakage spectra at 0 degrees for the 5.08CM(Z) FNS-TOF beryllium FNS-TOF experiment: ENDF/B-VIII.1b2.....	54
Figure 69. Angular neutron leakage spectra at 0 degrees for the 15.24CM(Z) FNS-TOF beryllium FNS-TOF experiment: ENDF/B-VIII.1b2.....	54
Figure 70. Angular neutron leakage spectra at 0 degrees for the 5.06CM(Z) FNS-TOF carbon FNS-TOF experiment: ENDF/B-VIII.1b2.	55
Figure 71. Angular neutron leakage spectra at 0 degrees for the 20.24CM(Z) FNS-TOF carbon FNS-TOF experiment: ENDF/B-VIII.1b2.	55
Figure 72. Angular neutron leakage spectra at 0 degrees for the 5.06CM(Z) FNS-TOF carbon FNS-TOF experiment: JEFF-4T.	55
Figure 73. Angular neutron leakage spectra at 0 degrees for the 20.24CM(Z) FNS-TOF carbon FNS-TOF experiment: JEFF-4T2.	55

Figure 74. Angular neutron leakage spectra at 0 degrees for the 40.48CM(Z) FNS-TOF carbon FNS-TOF experiment: ENDF/B-VIII.1b2.	55
Figure 75. Angular neutron leakage spectra at 0 degrees for the 40.48CM(Z) FNS-TOF carbon FNS-TOF experiment: JEFF-4T2.	55
Figure 76. Angular neutron leakage spectra at 0 degrees for the 5.06CM(Z) FNS-TOF lead FNS-TOF experiment: ENDF/B-VIII.1b2.	56
Figure 77. Angular neutron leakage spectra at 0 degrees for the 40.64CM(Z) FNS-TOF lead FNS-TOF experiment: ENDF/B-VIII.1b2.	56
Figure 78. Angular neutron leakage spectra at 0 degrees for the 5.06CM(Z) FNS-TOF lead FNS-TOF experiment: JEFF-4T2.	56
Figure 79. Angular neutron leakage spectra at 0 degrees for the 40.64CM(Z) FNS-TOF lead FNS-TOF experiment: JEFF-4T2.	56
Figure 80. Angular neutron leakage spectra at 0 degrees for the 203.2CM(Z) FNS-TOF lead FNS-TOF experiment: ENDF/B-VIII.1b2.	56
Figure 81. Angular neutron leakage spectra at 0 degrees for the 203.2CM(Z) FNS-TOF lead FNS-TOF experiment: JEFF-4T2.	56
Figure 82. Angular neutron leakage spectra at 0 degrees for the SLAB FNS-TOF oxygen FNS-TOF experiment: ENDF/B-VIII.1b2.	57
Figure 83. Angular neutron leakage spectra at 0 degrees for the SLAB FNS-TOF nitrogen FNS-TOF experiment: ENDF/B-VIII.1b2.	57
Figure 84. Angular neutron leakage spectra at 0 degrees for the SLAB FNS-TOF oxygen FNS-TOF experiment: JEFF-4T2.	57
Figure 85. Angular neutron leakage spectra at 0 degrees for the SLAB FNS-TOF nitrogen FNS-TOF experiment: JEFF-4T2.	57
Figure 86. Angular neutron leakage spectra at 0 degrees for the 4.08CM(Z) FNS-TOF Li2O FNS-TOF experiment: ENDF/B-VIII.1b2.	57
Figure 87. Angular neutron leakage spectra at 0 degrees for the 20.00CM(Z) FNS-TOF Li2O FNS-TOF experiment: ENDF/B-VIII.1b2.	57
Figure 88. Angular neutron leakage spectra at 0 degrees for the 4.08CM(Z) FNS-TOF Li2O FNS-TOF experiment: JEFF-4T2.	58
Figure 89. Angular neutron leakage spectra at 0 degrees for the 20.00CM(Z) FNS-TOF Li2O FNS-TOF experiment: JEFF-4T2.	58
Figure 90. Angular neutron leakage spectra at 0 degrees for the 40.00CM(Z) FNS-TOF Li2O FNS-TOF experiment: ENDF/B-VIII.1b2.	58
Figure 91. Angular neutron leakage spectra at 0 degrees for the 40.00CM(Z) FNS-TOF Li2O FNS-TOF experiment: JEFF-4T2.	58
Figure 92. Example of OKTAVIAN pulsed sphere 61 cm: Type I.	58
Figure 93. Neutron leakage for the OKTAVIAN Zr-61cm: JEFF-4T2.	59
Figure 94. Neutron leakage for the OKTAVIAN Al-40cm: JEFF-4T2.	59
Figure 95. Neutron leakage for the OKTAVIAN Zr-61cm: ENDF/B-VIII.1b2.	59
Figure 96. Neutron leakage for the OKTAVIAN Al-40cm: ENDF/B-VIII.1b2.	59
Figure 97. Neutron leakage for the OKTAVIAN Mo-61cm: JEFF-4T2.	60
Figure 98. Neutron leakage for the OKTAVIAN Cu-61cm: JEFF-4T2.	60
Figure 99. Neutron leakage for the OKTAVIAN Mo-61cm: ENDF/B-VIII.1b2.	60
Figure 100. Neutron leakage for the OKTAVIAN Cu-61cm: ENDF/B-VIII.1b2.	60
Figure 101. Neutron leakage for the OKTAVIAN Co-40cm: JEFF-4T2.	60
Figure 102. Neutron leakage for the OKTAVIAN W-40cm: JEFF-4T2.	60
Figure 103. Neutron leakage for the OKTAVIAN Co-40cm: ENDF/B-VIII.1b2.	60
Figure 104. Neutron leakage for the OKTAVIAN W-40cm: ENDF/B-VIII.1b2.	60
Figure 105. Neutron leakage for the OKTAVIAN Ti-40cm: JEFF-4T2.	61
Figure 106. Neutron leakage for the OKTAVIAN Teflon-40cm: JEFF-4T2.	61
Figure 107. Neutron leakage for the OKTAVIAN Ti-40cm: ENDF/B-VIII.1b2.	61
Figure 108. Neutron leakage for the OKTAVIAN Teflon-40cm: ENDF/B-VIII.1b2.	61
Figure 109. Neutron leakage for the OKTAVIAN Si-60cm: JEFF-4T2.	61
Figure 110. Neutron leakage for the OKTAVIAN Nb-28cm: JEFF-4T2.	61
Figure 111. Neutron leakage for the OKTAVIAN Si-60cm: ENDF/B-VIII.1b2.	61
Figure 112. Neutron leakage for the OKTAVIAN Nb-28cm: ENDF/B-VIII.1b2.	61
Figure 113. Neutron leakage for the OKTAVIAN Mn-61cm: JEFF-4T2.	62

Figure 114. Neutron leakage for the OKTAVIAN Cr-40cm: JEFF-4T2.....	62
Figure 115. Neutron leakage for the OKTAVIAN Mn-61cm: ENDF/B-VIII.1b2.....	62
Figure 116. Neutron leakage for the OKTAVIAN Cr-40cm: ENDF/B-VIII.1b2.....	62
Figure 117. Neutron leakage for the OKTAVIAN LiF-61cm: JEFF-4T2.....	62
Figure 118. Neutron leakage for the OKTAVIAN As-40cm: JEFF-4T2.....	62
Figure 119. Neutron leakage for the OKTAVIAN LiF-61cm: ENDF/B-VIII.1b2.....	62
Figure 120. Neutron leakage for the OKTAVIAN As-40cm: ENDF/B-VIII.1b2.....	62
Figure 121. Values (C/E-1) in % of ²³⁵ U-Total Transmission Function for sample 1(0.002574 atm/b).....	63
Figure 122. Values (C/E-1) in % of ²³⁵ U-Fission Transmission Function for sample 1(0.002574 atm/b).....	63
Figure 123. Values (C/E-1) in % of ²³⁵ U-Total Transmission Function for sample 7(0.17160 atm/b).....	64
Figure 124. Values (C/E-1) in % of ²³⁵ U-Fission Transmission Function for sample 7(0.17160 atm/b).....	64

1. Introduction

SANDA Subtask 5.2.2 “*C/E* validation and trends” aims to contribute to the validation of JEFF nuclear data files by comparing Calculations (*C*) with experimental measurements (*E*) and analysing biases to identify possible trends and gaps in the validation domain. This deliverable reports on *C/E* validation activities for reactor physics experiments and shielding benchmarks, encompassing representative experiments from different facilities, neutron spectra, and integral quantities of interest. Integral experiments have been sourced from IRPhEP [IRPhEP, 2019], ICSBEP [ICSBEP, 2020] and SINBAD [SINBAD, 2021] international databases, as well as from other legacy experiment data and participants’ own databases.

Systematic use of JEFF-3.3 and new WP4 evaluations up to JEFF4T3 (made available in February 2024) has been done. JEFF-based *C/E* results have been analyzed to identify biases, investigate the reasons for the differences and infer trends, using different validation methodologies.

The deliverable is structured as follows. First, methodologies and metrics for nuclear data validation are presented. Second, validation for liquid metal fast reactors is addressed (UPM). Then, validation of thermal reactors is presented (UPM, CEA/DEN and NRG), with particular attention to LWR. Finally, nuclear data validation using selected shielding benchmarks, known to be more sensitive to scattering reactions than criticality experiments, is discussed (UPM and JSI in cooperation with UKAEA).

2. Considerations about methodologies for nuclear data validation

Following [Ivanova, 2017], a robust nuclear data validation process requires the following:

- A statistically significant number of integral experiments to be used.
- Experimental data used for validation should differ from the data used for nuclear data evaluation or nuclear model calibration.
- Biases and uncertainties in the application domain must be quantified, and a clear understanding of the origin of such biases and uncertainties is sought.

Different widely applied types of validation methodologies or V&UQ (Validation and Uncertainty Quantification) strategies can be distinguished, differing in how they use the calculated *C/E* ratios and incorporate the available information:

- **The first approach consists of evaluating the mean bias or weighted mean bias.** It aims to characterize an entire library for a given domain of applicability (such as all fast reactors, all thermal systems, systems containing Plutonium, etc.) by using a large number of integral experiments, involving many nuclides and reactions. Different metrics can be applied, considering correlations among experimental uncertainties or not. The biases obtained strongly depend on the metrics used, the number of benchmarks, and whether correlations are considered or not.
- **The second approach relies on perturbation analysis.** It aims to evaluate the impact of nuclear data perturbations. This can be done by replacing an individual nuclide or cross section in a library by data in other library to analyse the origin of individual biases. New calculations can be performed with the tuned library or, if sensitivity vectors to nuclear data are available, they can be used to estimate the impact of the nuclear data perturbation on the bias. NDaST tool from NEA/OECD provides this capability and the accuracy of results strongly depends on how close to linearity is the system behaviour, so this analysis aims to provide qualitative conclusions. NDaST allows to evaluate the impact of a particular cross section via replacing this quantity with the corresponding cross section vector provided by other nuclear data library. The change of the calculated value as a result of the perturbation is estimated by NDaST as follows (where P_i is the energy-dependent perturbation ratio between the considered libraries -being g the energy groups- and $S_{C,i}$ is the sensitivity vector):

$$\frac{\Delta C}{c} \approx \sum_{i=1}^g (P_i - 1) S_{C,i} \quad (\text{eq. 1})$$

- **The third approach is the trend analysis.** It involves comparisons with trending parameters (e.g., EALF², enrichment, fuel diameter/pitch, ...) and may conduct extrapolations along specified trending variables. This method aims to validate individual nuclear data, focusing on identifying specific needs through the use of selected sets of integral experiments.
- **The four approach is the Bayesian-based analysis, deterministic or stochastic.** This kind of techniques are based on Bayes theorem to find an optimal solution using mathematical statistics while making the most of all the information provided by the experimental measurements. The ratios C/E for Bayesian approaches do not differ from other techniques, but data assimilation can provide ranking tables characterizing similarity between integral experiments and applications, biases and uncertainties that can be used as a basis for recommendations for nuclear data improvement.

The different approaches are not mutually exclusive and provide complementary information, with the ultimate goal of identifying the sources of deviation. They have been employed for validation purposes in this work.

2.1. Metrics for evaluating biases

To evaluate the overall performance of a library within a given validation domain, different metrics can be used [Ivanova, 2003] [Zwermann and Hill, 2022] [Cabellos, 2022], providing different information. The ones used in this deliverable are presented as follows.

Let us consider N experimental benchmarks and calculations, being $\{\Delta_i = C_i - E_i\}_{i=1,N}$ the bias between the calculated and measured values. Then, for each experiment, the uncertainty associated to the $C_i - E_i$ deviation due to the experimental uncertainty, σ_{E_i} , and computational uncertainty, σ_{C_i} (statistical independent) is computed as $\sigma_{\Delta_i} = \sqrt{\text{var}(C_i - E_i)} = \sqrt{\text{var}(C_i) + \text{var}(E_i)} = \sqrt{\sigma_{C_i}^2 + \sigma_{E_i}^2}$

The uncertainty in the experiment is usually much higher than the model calculational uncertainty, that can be neglected in practice when using high-fidelity Monte Carlo computational tools with very low statistical errors (< 10 pcm).

2.1.1. If experiments are not correlated:

MEAN SIGNED DEVIATION (MSD) AND ITS STANDARD DEVIATION OR UNCERTAINTY:

$$MSD = \frac{1}{N} \sum_{i=1}^N (C_i - E_i) \quad \sigma_{MSD} = \frac{1}{\sqrt{\sum_{i=1}^N \frac{1}{\sigma_{E_i}^2}}} \quad (\text{eq. 2})$$

MEAN ABSOLUTE DEVIATION (MAD):

$$MAD = \frac{1}{N} \sum_{i=1}^N |C_i - E_i| \quad \sigma_{MAD} = \frac{1}{\sqrt{\sum_{i=1}^N \frac{1}{\sigma_{E_i}^2}}} \quad (\text{eq. 3})$$

MEAN SIGNED DEVIATION (MSD) DIVIDED BY BENCHMARK UNCERTAINTY:

$$MSD_{\sigma} = \frac{1}{N} \sum_{i=1}^N \frac{(C_i - E_i)}{\sigma_{E_i}} \quad \sigma_{MSD} = \frac{1}{\sqrt{\sum_{i=1}^N \frac{1}{\sigma_{E_i}^2}}} \quad (\text{eq. 4})$$

² EALF: Energy corresponding to the Average Lethargy of neutronics causing Fission.

MEAN ABSOLUTE DEVIATION (MAD) DIVIDED BY BENCHMARK UNCERTAINTY:

$$MAD_{\sigma} = \frac{1}{N} \sum_{i=1}^N \frac{|C_i - E_i|}{\sigma_{E_i}} \quad \sigma_{MAD} = \frac{1}{\sqrt{\sum_{i=1}^N \frac{1}{\sigma_{E_i}^2}}} \quad (\text{eq. 5})$$

CHI SQUARED VALUE:

$$\chi^2 = \frac{1}{N} \sum_{i=1}^N \frac{(C_i - E_i)^2}{\sigma_{E_i}^2} \quad (\text{eq. 6})$$

MEAN WEIGHTED DEVIATION (MWD) AND ITS STANDARD DEVIATION:

$$MWD = \frac{\sum_{i=1}^N \frac{(C_i - E_i)}{\sigma_{E_i}^2}}{\sum_{i=1}^N \frac{1}{\sigma_{E_i}^2}} \quad \sigma_{MWD} = \frac{1}{\sqrt{\sum_{i=1}^N \frac{1}{\sigma_{E_i}^2}}} \quad (\text{eq. 7})$$

The mean signed deviation (MSD) quantifies the difference between benchmark and calculated values, while the mean absolute deviation (MAD) focuses on the absolute differences in magnitude, allowing to understand the nature of the deviations. The corresponding quantities divided by the benchmark uncertainties are insightful to evaluate the deviations in terms of the benchmark standard deviations, that can be significant for some experiments. If obtained values are lower than 1, on average, calculations match benchmarks to within one experimental standard deviation.

2.1.2. If uncertainties of experiments are correlated:

In this case, the average deviation of all N experiments should be defined taking into account the uncertainty covariance matrix U , where each element of the matrix is equal to $U_{i,j} = \sigma_{E_i} \sigma_{E_j} \text{corr}_{ij}$.

MEAN WEIGHTED DEVIATION (MWD) AND ITS STANDARD DEVIATION:

$$MWD_{corr} = \frac{\sum_{i=1}^N \sum_{j=1}^N U_{ij}^{-1} (C_i - E_i)}{\sum_{i=1}^N \sum_{j=1}^N U_{ij}^{-1}} \quad \sigma_{MWD_{corr}} = \frac{1}{\sqrt{\sum_{i=1}^N \sum_{j=1}^N U_{ij}^{-1}}} \quad (\text{eq. 8})$$

In D5.6 it was shown that correlations between uncertainties of experimental values strongly influence the quantitative information obtained from the mean weighted deviation. In this deliverable, the used metrics do not consider experiment correlations.

2.2. Codes employed for validation

Both Monte Carlo neutron transport codes and deterministic codes have been employed in this report for validation purposes. Two Monte Carlo neutron transport codes, which allow minimize methodological errors, were used:

- The Monte Carlo N-Particle (MCNP), a general purpose Monte Carlo transport code developed at Los Alamos National Laboratory (LANL) in New Mexico, USA. Versions used for the calculations reported here are Version 5 [Goorley, 2004] and Version 6 [Goorley 2012], subversions 6.1 [Goorley, 2013] and 6.2 [Werner 2018].
- The Monte Carlo code KENO-VI from SCALE code system, developed and maintained by Oak Ridge National Laboratory. Release SCALE6.2.3 was used [Rearden, 2016].

Concerning deterministic codes, PARTISN [Alcouffe, 2009] and SUSD-3D [Kodeli, 2022] were used for shielding benchmarks. SEANAP system [Ahnert, 1988] and APOLLO2 [Santamarina, 2009] were employed for the analysis in commercial LWR. Details are given in the corresponding sections.

3. Advanced fast reactors C/E validation and nuclear data trends (UPM)

Liquid Metal Fast Reactors (LMFRs) have been recognized as one of the most promising technologies within Generation-IV nuclear systems. Consequently, nuclear data validation efforts for advanced reactors must be addressed. To assess the accuracy of JEFF-evaluations in that specific application domain, first, a list of the most informative experiments for validation was obtained. Then, different validation approaches based on determining C/E bias were applied to draw conclusions.

3.1. Experimental database based on similarity indexes

In order to select integral experiments useful for LMFR, not only for core multiplication factor, but also for other responses such as reactivity effects, similarity between targeted applications and potential experiments in ICSBEP and IRPhEP was assessed to establish the degree of shared information. Two Sodium-Cooled Fast Reactors were chosen as application objects: the ESFR core design (European Sodium Fast Reactor) and ASTRID core design, both described in Deliverable D5.2. Sensitivities for these reactors can be found in [García-Herranz, 2022].

Two representative factors were used, the factor c_k and the index E (used by DICE NEA tool):

$$c_k = \frac{S_R^T V_\alpha S_E}{\sqrt{(S_R^T V_\alpha S_R)(S_E^T V_\alpha S_E)}} \quad (\text{eq. 9})$$

$$E = \frac{S_R^T S_E}{\sqrt{(S_R^T S_R)(S_E^T S_E)}} \quad (\text{eq. 10})$$

Where S_R and S_E correspond to the sensitivity vectors for the application of interest and experiment under evaluation respectively and V_α is the 33g JEFF-3.3 covariance matrix. While E index evaluates the similarity in terms of shared important characteristics, in c_k the basis for similarity also included the shared unknown information.

The similarity analysis using ICSBEP database led to identify a set of useful experiments. The c_k similarity index with ESFR and ASTRID is shown in Figure 1:

- A dataset of 34 integral experiments of ICSBEP (Table 1) have been identified as able to provide relevant information for SFR. Representative experiments correspond to benchmarks with plutonium (PU) and mixed plutonium-uranium (MIX) fissile materials, with a physical form of compound (COMP) or metal/alloy (MET) and with a FAST neutron spectrum.

The similarity analysis using IRPhEP database led to identify a potential list of experiments. The c_k similarity indexes with ESFR and ASTRID for the multiplication factor and for the sodium voiding effect are shown in Figure 2 and Figure 3. Moreover, other fast systems in IRPhEP were considered, such as the UO₂-fueled EBR2 reactor or lead-cooled systems, that could be helpful for biases identification. From the potential list, the integral experiments in Table 2 have been retained as useful for nuclear data validation, based upon: *i*) the availability of a MCNP input either found in the open documents or provided by other researchers [Winfried, 2024]; *ii*) a reliable representation of the models of the real arrangements (as-built models or close to the real arrangements):

- A dataset of 16 integral experiments for the multiplication factor from facilities in Figure 4.
- A dataset of 7 experiments for sodium void worth and 5 experiments for control rod worth (although these were discarded as useful for nuclear data validation due to high experimental uncertainties).

A lack of experiments in the IRPhEP database regarding Doppler measurements for fast spectrum systems was found. Then, the SEFOR experiment, that is being evaluated by L. Buiron in the framework of SFR-

UAM benchmark [Cervantes, 2024], has been identified as a key experimental program for the evaluation of Doppler effect and reflector worth, and therefore selected as part of the validation suite in Table 3.

Compared to other databases for nuclear data validation, reactor physics experiments in IRPhEP handbook provide: *i)* other integral responses apart from k-eff, that can provide insight into potential deviations in different reaction channels and energy groups; *ii)* as-built models (or very close to the real world), avoiding potential biases arising when transforming an experimental configuration into a simplified model; *iii)* experiments not used in evaluation/calibration of nuclear data libraries. It is worth it to mention that, although they are not very clean experiments, since they involve many different physical aspects, they are highly valuable to assess the predictive capability of an evaluation for real complex reactors.

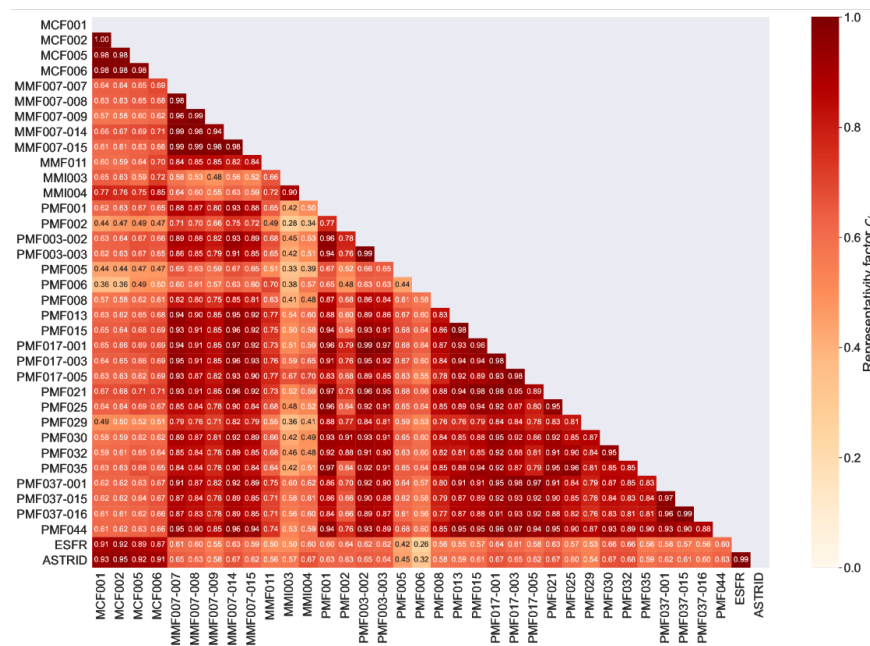
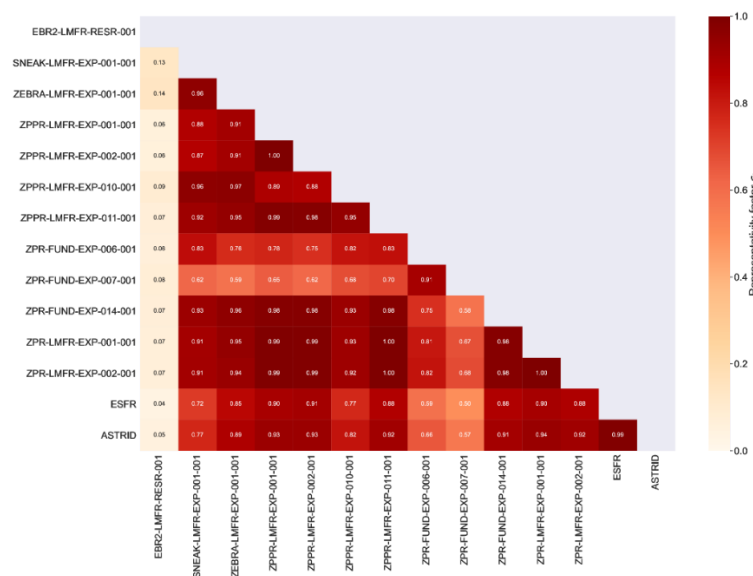


Figure 1. Similarity matrix between the ICSBEP dataset and the selected SFR designs, for the multiplication factor.



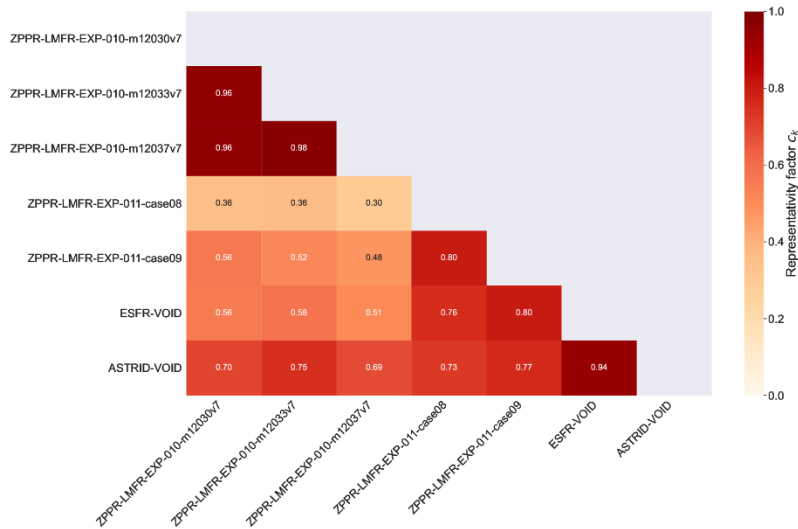


Figure 3. Similarity matrix between the IRPhEP dataset and the selected SFR designs, ESFR and ASTRID, for the sodium voiding effect.

Table 1. Selected integral experiments in ICSBEP database useful for SFR validation.

#	Experiment	Identifier	Experimental facility	Laboratory
1	MIX-COMP-FAST-001-001	MCF001	ZPR-6/7	ANL, USA
2	MIX-COMP-FAST-002-001	MCF002	ZPR-6/7 high ²⁴⁰ Pu	ANL, USA
3	MIX-COMP-FAST-005-001	MCF005	ZPR-9/31	ANL, USA
4	MIX-COMP-FAST-006-001	MCF006	ZPPR-2	ANL, USA
5	MIX-MET-FAST-007-007	MMF007-007	Spherical composite core	LLNL, USA
6	MIX-MET-FAST-007-008	MMF007-008	Spherical composite core	LLNL, USA
7	MIX-MET-FAST-007-009	MMF007-009	Spherical composite core	LLNL, USA
8	MIX-MET-FAST-007-014	MMF007-014	Spherical composite core	LLNL, USA
9	MIX-MET-FAST-007-015	MMF007-015	Spherical composite core	LLNL, USA
10	MIX-MET-FAST-011-001	MMF011	ZPPR-21B	ANL, USA
11	MIX-MET-INTER-003-001	MMI003	ZPR-3/54	ANL, USA
12	MIX-MET-INTER-004-001	MMI004	ZPR-3-/53	ANL, USA
13	PU-MET-FAST-001-001	PFM001	JEZEBEL	LANL, USA
14	PU-MET-FAST-002-001	PFM002	ZPR-6/7 ²⁴⁰ Pu	LANL, USA
15	PU-MET-FAST-003-002	PFM003-002	Pu metal button array	LLNL, USA
16	PU-MET-FAST-003-003	PFM003-003	Pu metal button array	LLNL, USA
17	PU-MET-FAST-005-001	PFM005	Pu sphere reflected by W	LANL, USA
18	PU-MET-FAST-006-001	PFM006	Flatop	LANL, USA
19	PU-MET-FAST-008-001	PFM008	Pu sphere reflected by Th	LANL, USA
20	PU-MET-FAST-013-001	PFM013	Pu fuel rods w/Cu-reflector	IPPE, Russia
21	PU-MET-FAST-015-001	PFM015	Pu fuel rods w/Fe-reflector	IPPE, Russia
22	PU-MET-FAST-017-001	PFM017-001	Pu metal cylinders array	LLNL, USA
23	PU-MET-FAST-017-003	PFM017-003	Pu metal cylinders array	LLNL, USA
24	PU-MET-FAST-017-005	PFM017-005	Pu metal cylinders array	LLNL, USA
25	PU-MET-FAST-021-001	PFM021	Pu cylinders w/ Be/BeO reflector	VNIIEF, Russia
26	PU-MET-FAST-025-001	PFM025	Spherical Pu assembly	VNIIEF, Russia
27	PU-MET-FAST-029-001	PFM029	Bare spherical ²³⁹ Pu assembly	VNIIEF, Russia
28	PU-MET-FAST-030-001	PFM030	Spherical Pu assembly	VNIIEF, Russia
29	PU-MET-FAST-032-001	PFM032	Spherical Pu assembly	VNIIEF, Russia
30	PU-MET-FAST-035-001	PFM035	Spherical Pu assembly Pb reflector	VNIIEF, Russia
31	PU-MET-FAST-037-001	PFM037-001	Arrays of Pu metal cylinders	CML, USA
32	PU-MET-FAST-037-015	PFM037-015	Arrays of Pu metal cylinders	CML, USA
33	PU-MET-FAST-037-016	PFM037-016	Arrays of Pu metal cylinders	CML, USA
34	PU-MET-FAST-044-001	PMF044	Pu metal sphere	LANL, USA

Table 2. Selected experiments in IRPhEP useful for LMFR validation.

#	Experiment	Identification	Fuel/Other	Parameter	Laboratory
1	BFS-97-1	BFS1-FUND-EXP-001-001	Pu, Depleted UO ₂ , poly	keff	IPPE, Russia
2	BFS-49-1	BFS1-FUND-EXP-004-001	Pu, Depleted UO ₂ , poly	keff	IPPE, Russia
3	BFS1-61-0	BSF-LMFR-EXP-002-001	Metal Pu-Depleted U/Lead	keff	IPPE, Russia
4	EBR-II	EBR2-LMFR-RESR-001	Metal U with 67% U ²³⁵ /Sodium	keff	ANL, USA
5	FFTF	FFTF-LMFR-RESR-001-001	MOX/Sodium	keff	Hanford, USA
6	SNEAK-7A	SNEAK-LMFR-EXP-001	MOX/Sodium	keff	KFK, Germany
7	SNEAK-7B	SNEAK-7B	MOX and UO ₂ /Sodim	keff	KFK, Germany
8	ZEBRA-22	ZEBRA-LMFR-EXP-001-001	Pu metal-UO ₂ /Sodium	keff	AEEW, UK
9	ZEBRA-23	ZEBRA-LMFR-EXP-001-002	Pu metal-UO ₂ /Sodium	keff	AEEW, UK
10	ZPPR-10A L07	ZPPR-LMFR-EXP-001-001	MOX/Sodium	keff	ANL, USA
11	ZPPR-9 L13	ZPPR-LMFR-EXP-002-001	MOX/Sodium	keff	ANL, USA
12	ZPPR-13A L24	ZPPR-LMFR-EXP-007-001	MOX/Sodium	keff	ANL, USA
13	ZPPR-12 L09	ZPPR-LMFR-EXP-010-001	MOX/Sodium	keff	ANL, USA
14	ZPPR-2 L90	ZPPR-LMFR-EXP-011-001	MOX/Sodium	keff	ANL, USA
15	ZPR-6/7 L99	ZPR-LMFR-EXP-001-001	MOX/Sodium	keff	ANL, USA
16	ZPR-6/7 L41	ZPR-LMFR-EXP-002-001	MOX/Sodium	keff	ANL, USA
17	ZPPR-12	ZPPR-LMFR-EXP-010-m12030	Loading 30	Sodium void	ANL, USA
18	ZPPR-12	ZPPR-LMFR-EXP-010-m12033	Loading 33	Sodium void	ANL, USA
19	ZPPR-12	ZPPR-LMFR-EXP-010-m12037	Loading 37	Sodium void	ANL, USA
20	ZPPR-2	ZPPR-LMFR-EXP-011-case06	Loading 181	Sodium void	ANL, USA
21	ZPPR-2	ZPPR-LMFR-EXP-011-case07	Loading 183	Sodium void	ANL, USA
22	ZPPR-2	ZPPR-LMFR-EXP-011-case08	Loading 184	Sodium void	ANL, USA
23	ZPPR-2	ZPPR-LMFR-EXP-011-case09	Loading 185	Sodium void	ANL, USA
24	FFTF	FFTF-LMFR-RESR-001-Case22	Primary Bank worth	Control worth	Hanford, USA
25	FFTF	FFTF-LMFR-RESR-001-Case23	Secondary Bank worth	Control worth	Hanford, USA
26	FFTF	FFTF-LMFR-RESR-001-Case30	Shutdown margin	Control worth	Hanford, USA
27	FFTF	FFTF-LMFR-RESR-001-Case31	Shutdown margin	Control worth	Hanford, USA
28	FFTF	FFTF-LMFR-RESR-001-Case32	Excess reactivity	Control worth	Hanford, USA

Table 3. Other selected experiments useful for LMFR validation: SEFOR experiments.

#	Experiment	Fuel/Other	Type	Facility	Laboratory
1	SEFOR Isothermal cases	MOX/Sodium	Doppler	SEFOR	GE, USA & KFK, Germany
2	SEFOR Calibration curves	MOX/Sodium	Reflector worth	SEFOR	GE, USA & KFK, Germany

3.2. Analysis of fast-spectrum selected benchmarks from ICSBEP and IRPhEP

Criticality calculations were performed with Monte Carlo neutron transport codes MCNP6 and KENO-VI/SCALE6.2.3 (in continuous energy mode) with $5 \cdot 10^8$ active neutron histories, being statistical uncertainties in k-eff of about 2-3 pcm, lower than benchmark uncertainties (larger than 70 pcm in all cases). Sensitivities were computed with KSEN/MCNP6 or TSUNAMI-3D/SCALE6.2.3 in 33 energy groups. Uncertainty analysis were performed using JEFF-3.3 COVERX-formatted matrix processed with AMPX in 33 energy groups.

Nuclear data libraries used for MCNP6:

- JEFF-3.1.1: ACE files NJOY99.040_up259, NEA_Dic2008
- JEFF-3.3: ACE files, NDEC-njoy 2016.42 at NEA on 2018-10-01
- JEFF-4T3: ACE files, NJOY2016.56 processed at NEA on 2024-02
- ENDF/B-VII.1: ACE files provided with MCNP6.1

Nuclear data libraries used for KENO-VI:

- ENDF/B-VII.1-based library provided with SCALE6.2.3
- JEFF-x libraries processed with AMPX code within SCALE-6.3b11 version: JEFF-3.1.1, JEFF-3.3, JEFF-4T1, JEFF-4T3.

It is worth it to mention that sensitivities for the analysed systems are significant in the URR range, i.e., for Pu-239 (ENDF/B-VII.1: URR between 2.5 keV and 30 keV; JEFF3.3: URR between 4 keV and 30 keV), for U-238 (ENDF/B-VII.1 and JEFF-3.3: URR between 20 keV and 149 keV).

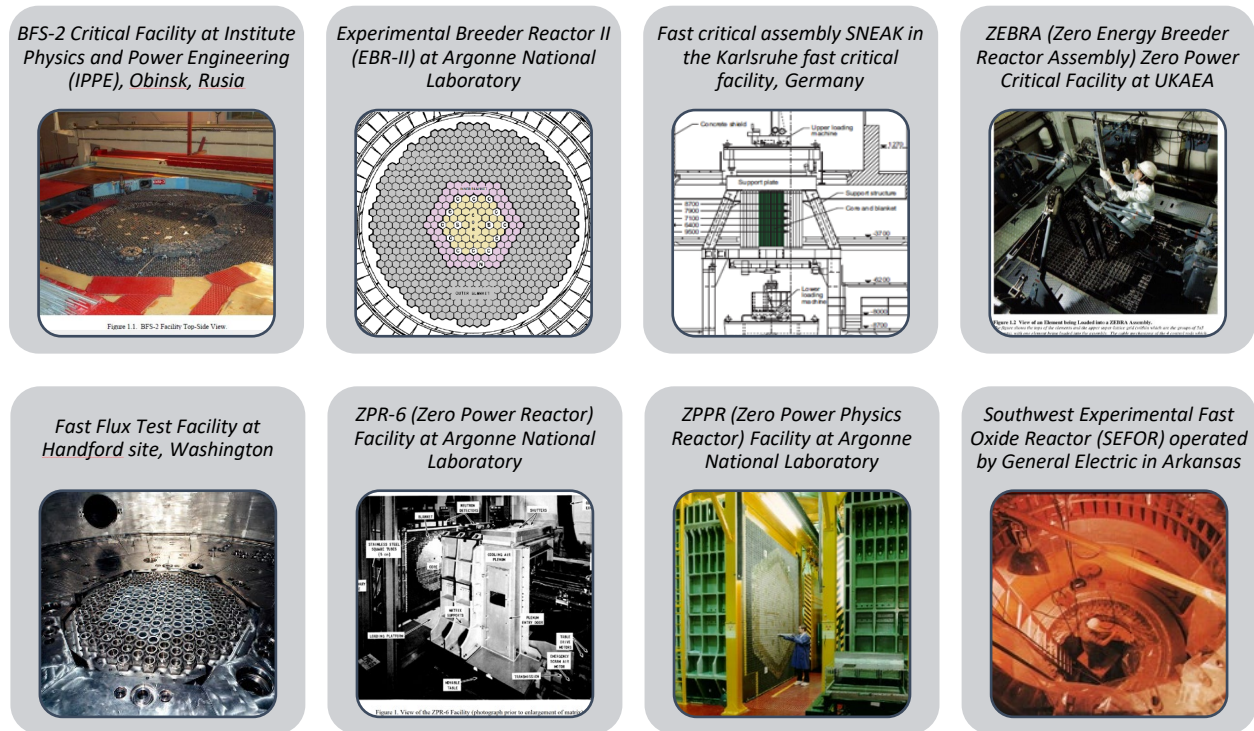


Figure 4. Illustration of reactor experiments in used for SFR validation.

3.2.1. Bias C-E analysis

Figure 5 and Figure 6 display C-E deviations of the multiplication factors for the selected ICSBEP and IRPhEP benchmarks respectively (in the latter, EALF range from 0.11 MeV to 0.36 MeV). In Figure 7 the deviations of the reactivity coefficients are given. As it can be seen, the benchmark uncertainties vary significantly among the different experiments, ranging from less than 100 pcm to 618 pcm for the EBR-II.

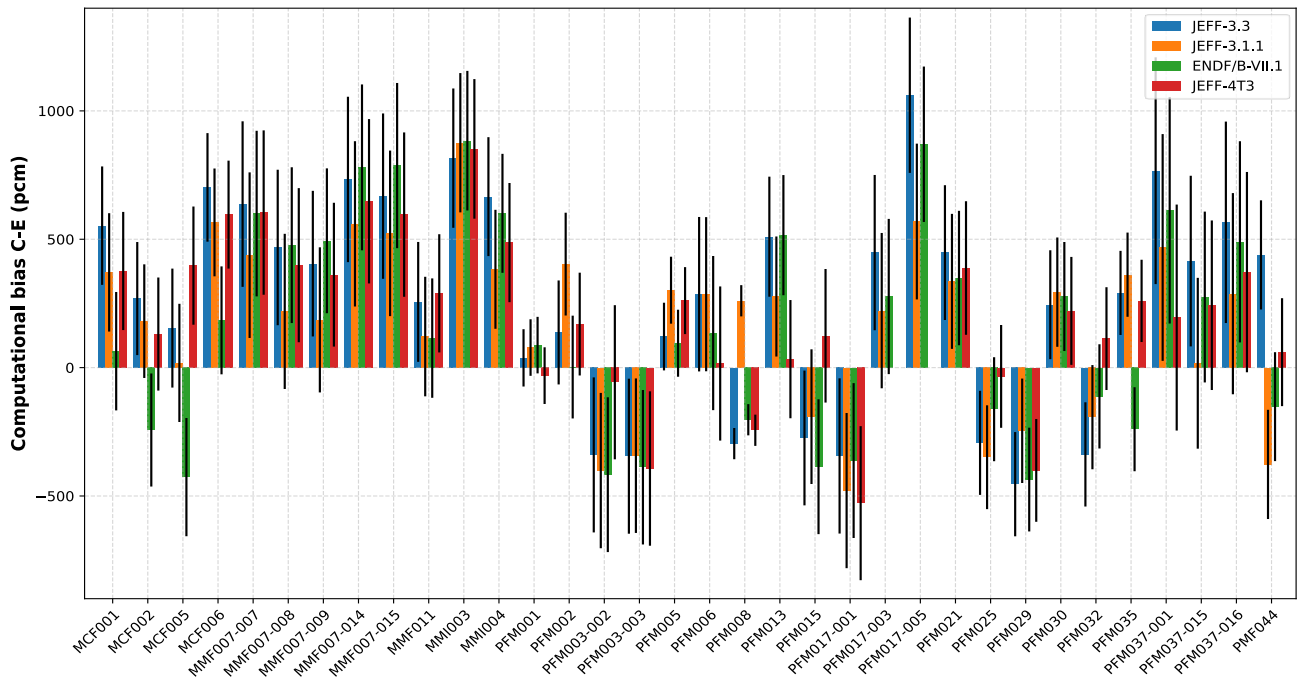


Figure 5. Computational biases in k -eff for the selected ICSBEP integral benchmark datasets (uncertainties account for both evaluated benchmark uncertainties and Monte Carlo statistical errors).

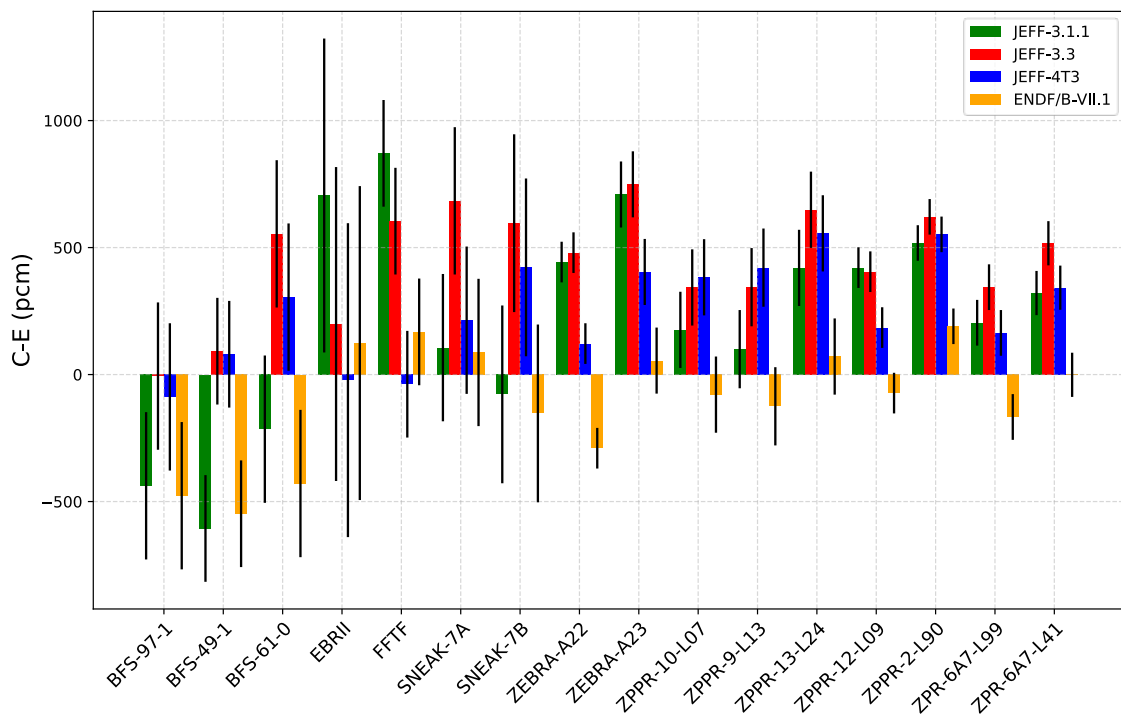


Figure 6. Computational biases in k -eff for the selected IRPhEP reactor physics benchmarks (uncertainties account for both evaluated benchmark uncertainties and Monte Carlo statistical errors).

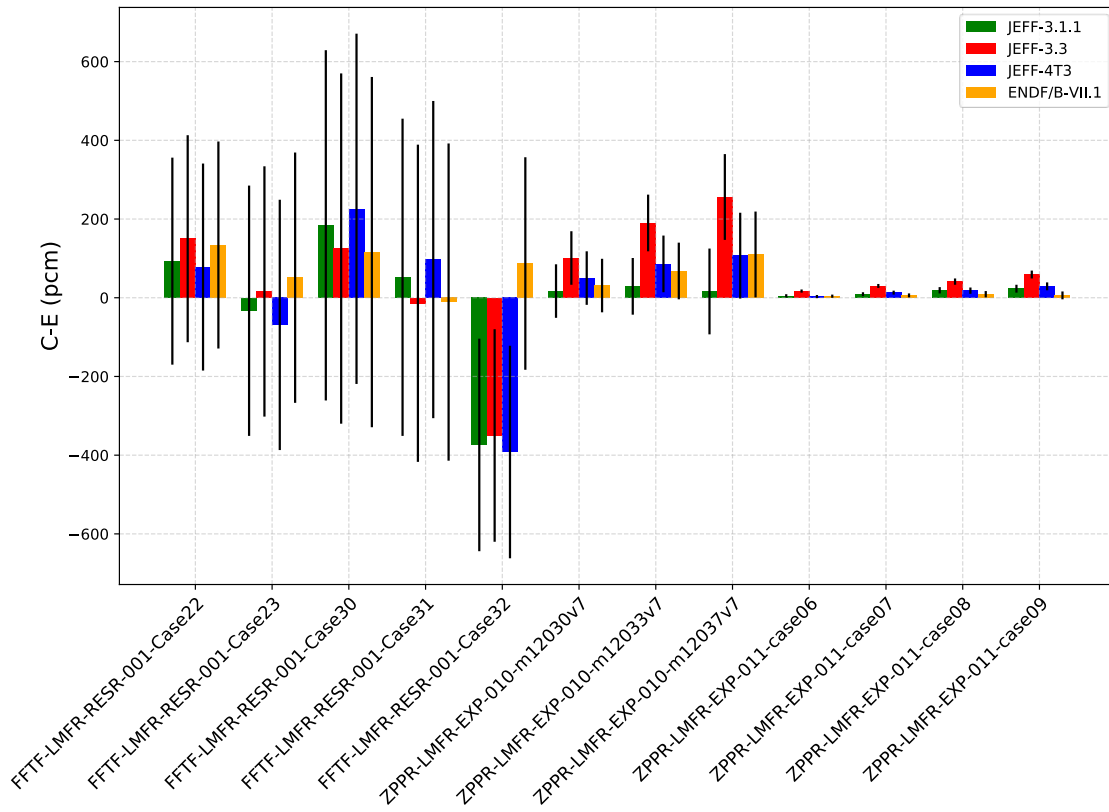


Figure 7. Computational biases in reactivity effects for the selected IRPhEP reactor physics benchmarks (uncertainties account for both evaluated benchmark uncertainties and Monte Carlo statistical errors).

C-E deviations for multiplication factors and reactivity effects with JEFF-4T3 were compared to nuclear data induced-uncertainties due to JEFF-3.3 covariance data in Figure 8 and Figure 9 respectively. It can be seen that the biases are covered by the nuclear data uncertainties for almost all cases as there is a huge impact of nuclear data uncertainties in fast spectrum region.

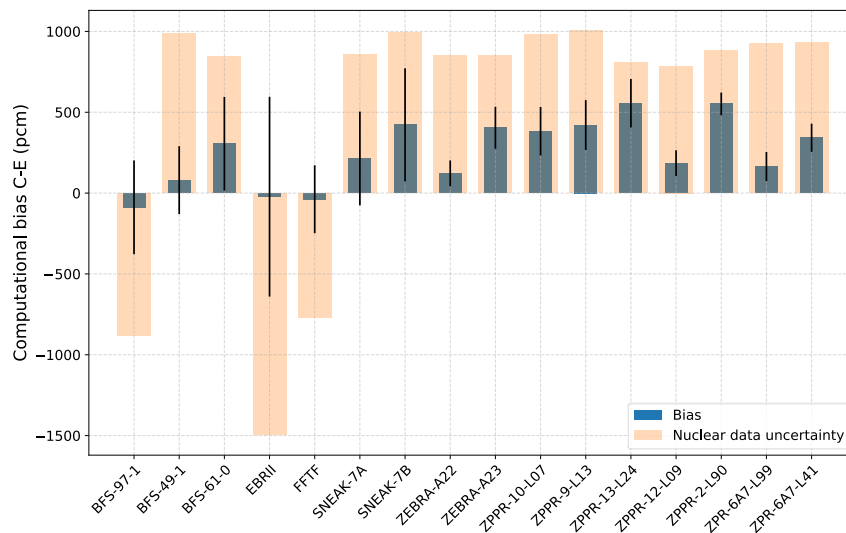


Figure 8. Comparison of C-E biases in the multiplication factor for JEFF-4T3 to nuclear data induced-uncertainties due to JEFF-3.3 covariance data.

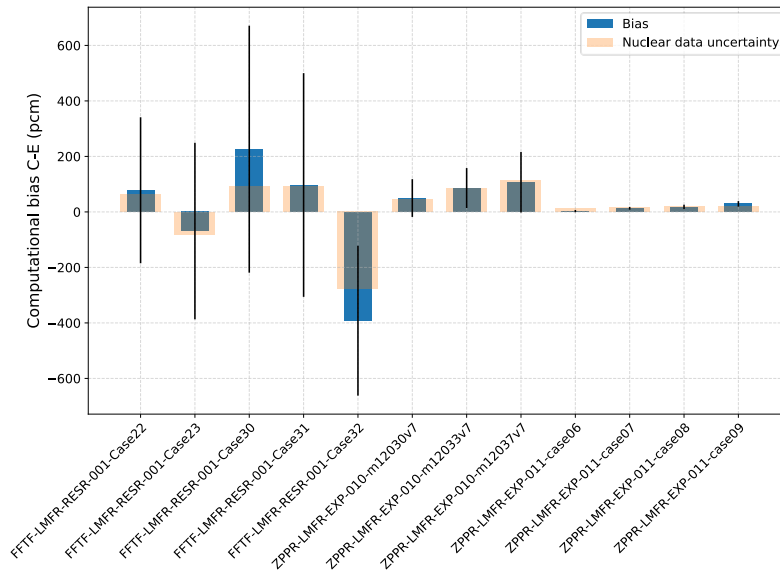


Figure 9. Comparison of C-E biases in reactivity effects for JEFF-4T3 to nuclear data induced-uncertainties due to JEFF-3.3 covariance data.

A comparison of different metrics is given in Table 4 and Table 5 for the multiplication factor for ICSBEP and IRPhEP benchmark dataset respectively for a quantitative measure of the overall deviations.

Table 4. Metrics for nuclear data library performance for the ICSBEP benchmark dataset

Metric	JEFF-3.1.1	JEFF-3.3	JEFF-4T3	ENDF/B-VII.1
MSD (%)	0.18	0.28	0.20	0.16
MAD (%)	0.33	0.43	0.31	0.37
MSD _σ	0.80	0.90	0.71	0.42
MAD _σ	1.42	1.77	1.32	1.45

Table 5. Metrics for nuclear data library performance for the IRPhEP benchmark dataset

Metric	JEFF-3.1.1	JEFF-3.3	JEFF-4T3	ENDF/B-VII.1
MSD (%)	0.23	0.45	0.25	-0.10
MAD (%)	0.40	0.45	0.27	0.19
MSD _σ	2.16	3.37	2.03	-0.56
MAD _σ	2.83	3.37	2.09	1.18

It can be seen that JEFF-3.3 systematically overestimates the benchmark results for both ICSBEP and IRPhEP benchmarks. This is also evident from the comparable values of MSD and MAD. The use of JEFF-4T3 notably reduces the deviations, although MSD_σ and MAD_σ metrics indicate that calculations do not align with benchmarks within one experimental benchmark standard deviation, which is nearly achieved with ENDF/B-VII.1. That is, the overall best agreement with the benchmark values corresponds to ENDF/B-VII.1 library.

Regarding the multiplication factor, significant improvements using JEFF-4T3 with respect to JEFF-3.3 are observed for some IRPhEP cases, like EBR-II and FTF. The different sign of the bias with respect to ENDF/B-VII.1 for SNEAK-7B is worth it to be investigated. For ZPPR experiments no improvement or slight improvement can be seen.

Regarding control worth cases, a large uncertainty is associated to the experimental measurements so that the C/E discrepancies are covered by the 1_σ experimental uncertainties. For ZPPR sodium void cases, JEFF-4T3 exhibits a better agreement to benchmark values than JEFF-3.3. Moreover, with JEFF-4T3 the trend exhibited by JEFF-3.3 (further analysed), where biases progressively increase as more sodium is voided, no longer occurs.

3.2.2. Perturbation analysis

A perturbation analysis was performed to provide insight into the C-E deviations. Sensitivities were used in NDaST tool from OECD/NEA.

Concerning ICSBEP, a reduced set of benchmarks were selected to identify biases, in particular, MIX-COMP-FAST series since they are the most similar benchmarks with selected SFR applications and exhibit biases of around 500 pcm. Cross section perturbations for ^{23}Na , ^{52}Cr , ^{56}Fe , ^{235}U , ^{238}U , ^{239}Pu and ^{240}Pu between JEFF-3.3 and JEFF-3.1.1 were applied leading to a multiplication factor increase of around 400 pcm when using JEFF-3.3 instead of JEFF-3.1.1. Main contributors to deviations are given in Table 6.

Table 6. Main contributors to deviations of multiplication factors between JEFF-3.3 and JEFF-3.1.1 for MIX-COMP-FAST experiments series. Energy-integrated isotope-reaction contribution to $\Delta k/k$ (in pcm).

Benchmark	Quantity	Contribution
MIX-COMP-FAST-001	^{238}U ν	-735
	^{238}U (n, γ)	722
	^{239}Pu (n,f)	292
	^{239}Pu χ	-228
	^{240}Pu (n,f)	88
MIX-COMP-FAST-002	^{239}Pu ν	-716
	^{238}U (n, γ)	712
	^{239}Pu (n,f)	290
	^{239}Pu χ	-228
	^{240}Pu (n,f)	122
MIX-COMP-FAST-005	^{238}U (n, γ)	718
	^{239}Pu ν	-673
	^{239}Pu (n,f)	329
	^{239}Pu χ	-249
	^{249}Pu (n, γ)	124
MIX-COMP-FAST-006	^{239}Pu ν	-722
	^{238}U (n, γ)	640
	^{239}Pu (n,f)	274
	^{239}Pu χ	-194
	^{249}Pu (n, γ)	117

It can be observed that:

- Compensating effects between ^{239}Pu and ^{238}U major cross sections play a key role to the bias.
- Concerning ^{238}U , the major perturbation is introduced by capture cross sections (a detailed analysis highlighted the energy interval between 20 keV and 820 keV).
- Perturbations in ^{239}Pu led to a decrease of k-eff driven by nubar and PFNS, and an increase driven by (n,f) and (n,capture).
- Other relevant contributions arise from ^{23}Na and ^{56}Fe mainly due to inelastic scattering cross sections above 1 MeV.

Concerning IRPhEP cases, an analysis with NDaST for ZPPR cases shows that the main contributors to deviations of multiplication factors between JEFF-3.3 and JEFF-3.1.1 are the ones in Table 7 for two representative ZPPR and ZPR cases.

Major contributors to deviations correspond to ^{239}Pu and ^{238}U cross sections, with a significant contribution of ^{23}Na (n,n') and lots of opposite contributions. A higher value of k-eff is predicted with JEFF-3.3 due to the capture of ^{238}U and due to ^{239}Pu fission, while a lower value of k-eff is predicted due to ^{239}Pu nubar and PFNS.

Contributors to deviations of sodium void effect between JEFF-3.3 and JEFF-3.1.1 are given in Table 8. It can be seen that ^{23}Na cross sections play an essential role as well as ^{239}Pu (n,γ) and ^{239}Pu (n,f). An analysis with NDaST of the ZPPR-2 void (see section 3.2.4), revealed that differences in ^{239}Pu (n,γ) around 1 keV were the main responsible of the different sodium void prediction with JEFF-3.3 and JEFF-3.1.1 libraries. However, JEFF-3.1.1 and JEFF-4T3 predicts similar sodium void effects, indicative of an improvement of ^{239}Pu cross-sections around ~ 1 keV in the new evaluation [García-Herranz, 2024].

Table 7. Main contributors to deviations of multiplication factors between JEFF-3.3 and JEFF-3.1.1 for selected LMFR arrangements. Energy-integrated isotope-reaction contribution to $\Delta k/k$ (in pcm).

Benchmark	Quantity	Contribution
ZPPR-2 L90 (ZPPR-LMFR-EXP-011)	^{239}Pu v	-640
	^{238}U (n,γ)	632
	^{239}Pu (n,f)	625
	^{239}Pu χ	-226
	^{23}Na (n,n')	-144
ZPR-6A7 L99 (ZPPR-LMFR-EXP-001)	^{238}U (n,γ)	720
	^{239}Pu v	-632
	^{239}Pu (n,f)	631
	^{239}Pu χ	-234
	^{23}Na (n,n')	-165

Table 8. Main contributors to deviations of sodium void effect between JEFF-3.3 and JEFF-3.1.1 for selected LMFR arrangements. Energy-integrated isotope-reaction contribution to $\Delta\rho/\rho$ (in%).

Benchmark	Quantity	Contribution
ZPPR-LMFR-EXP-010- m23037v7	^{23}Na (n,n)	6.39
	^{23}Na (n,n')	2.91
	^{239}Pu (n,γ)	1.89
	^{239}Pu (n,f)	-1.72
	^{23}Na (n,γ)	1.59
ZPPR-LMFR-EXP-011- case09	^{23}Na (n,n')	11.75
	^{239}Pu (n,γ)	5.78
	^{23}Na (n,γ)	2.54
	^{238}U (n,n)	-1.62
	^{23}Na (n,n)	-1.37

A perturbation analysis with JEFF-4T3 for SNEAK reactors (see section 3.2.3) indicated that U-238 and Pu-239 impacts strongly k-eff values, with opposite contributions. But it revealed an additional issue: a high influence of U-238 elastic scattering between 0.1 a 1 MeV, both the cross section and the angular distribution.

3.2.3. Perturbation analysis for multiplication factor of SNEAK reactors

The differences in biases between JEFF-4T3 and ENDF/B-VII.1 for SNEAK reactors was examined in detail [García-Herranz, 2024]. Results are shown in Table 9 and Figure 10.

- First, perturbation analysis using NDaST was performed, computing the impact of JEFF-4T3 cross sections, nubar and PNFS with respect to ENDF/B-VII.1. The predicted impact (859 pcm for SNEAK-7B) was much higher than the observed deviation with direct MCNP calculations (575 pcm for SNEAK-7B).
- Then, MCNP perturbation of ^{238}U nuclear data and of only of MT2/MF4 ^{238}U was carried out. Comparison of obtained values indicated a compensation of the ^{238}U elastic angular distribution and the rest of ^{238}U data.

- NDaST predictions with the elastic angular distribution provided comparable differences to the deviations with direct MCNP calculations between J4T3 and E71, allowing a rough estimation of the different contributions.

It was then concluded that:

- ^{238}U is the main responsible of differences (also significant changes in ^{239}Pu cross sections but with opposite contributions).
- ^{238}U (n,γ) and (n,fis) have a high influence.
- ^{238}U elastic scattering between 0.1 and 1 MeV has a strong impact, that appears to be compensated by the differences in the elastic angular distribution.

Table 9. Analysis of differences between JEFF-4T3 and ENDF/B-VII.1 for SNEAK configurations.

	SNEAK-7A	SNEAK-7B
C-E (pcm) J4T3	214	422
C-E (pcm) E71	87	-153
Differences (pcm) J4T3 vs. E71	127	575
Perturbation with NDaST: impact of (J4T3-E71)/E71	483	859
Perturbation replacing data in MCNP: E71 with J4T3 Pu^{239} vs. E71	-58	57
Perturbation replacing data in MCNP: E71 with J4T3 U^{238} vs. E71	488	825
Perturbation replacing data in MCNP: E71 with J4T3 U^{238} elastic angular dbn vs. E71	-431	-350
Estimation of the impact of J4T3 U^{238} other	919	1175
Global NDaST effect + elastic angular dbn	52	509

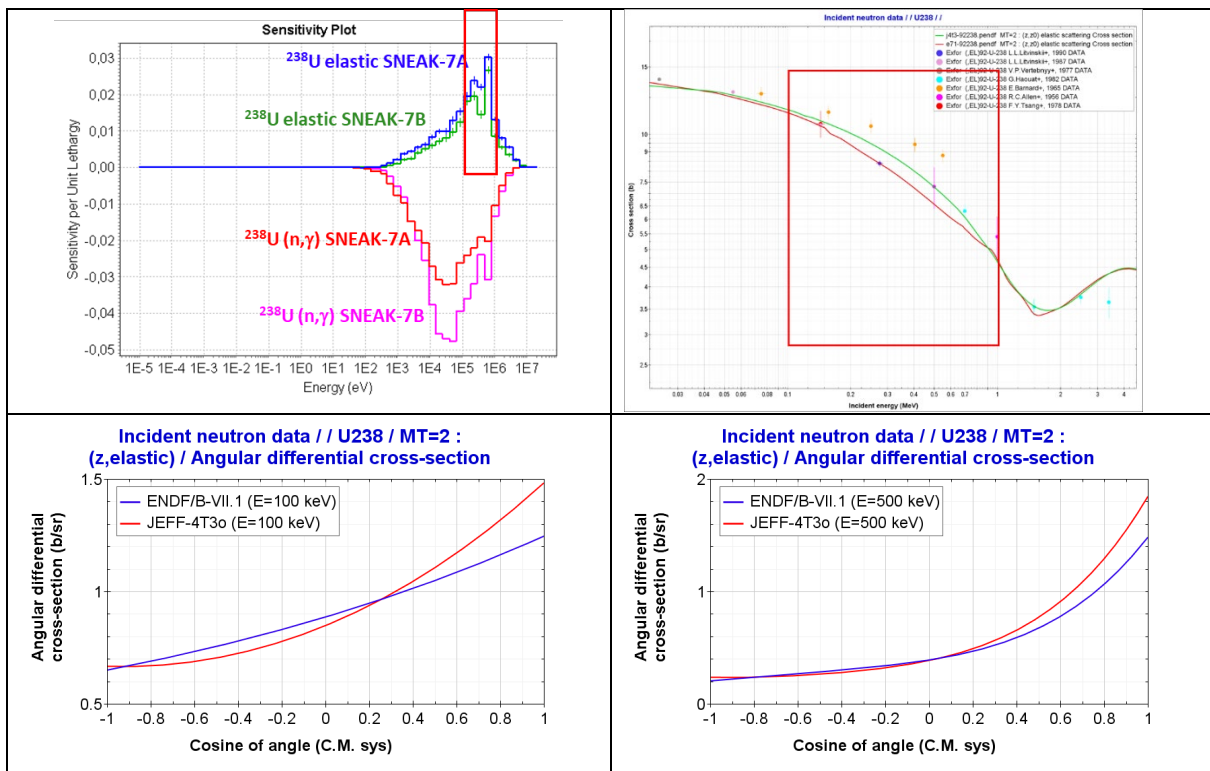


Figure 10. Sensitivity profiles for SNEAK configurations. Differences in the ^{238}U elastic cross section and angular distributions in JEFF-4T3 and ENDF/B-VII.1

3.2.4. Trend analysis for sodium void worth (SVR)

The C-E biases in sodium void worth when voiding different quantities of sodium in the ZPPR Assembly 2 experiments (ZPPR-LMFR-EXP-011) were examined. Results are presented in Figure 11, where the trend exhibited by JEFF-3.3 as more sodium is voided can be identified, while JEFF4T3 no longer presents that behaviour.

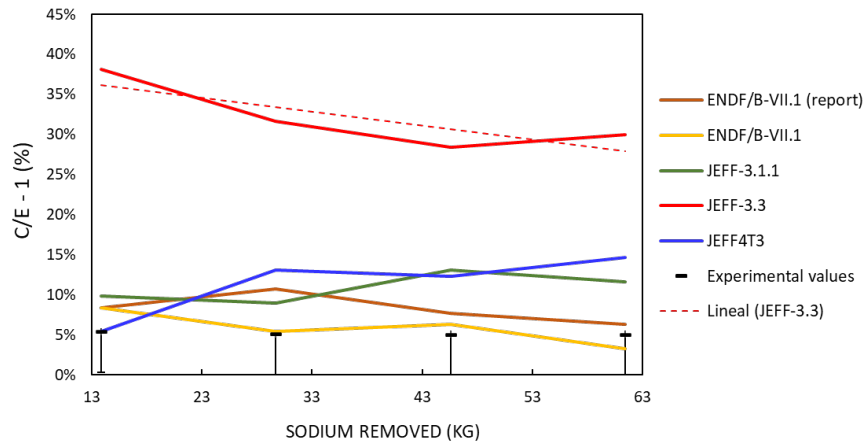


Figure 11. Biases in ZPPR-2 experiments with different quantities of sodium removed.

Sensitivities for sodium voiding are compared to sensitivities for the multiplication factor in Figure 12. It can be seen that: while SVR is very sensitive to Pu-239 capture at ~ 1 keV, k-eff is not very sensitive to that reaction; while SVR is very sensitive to Pu-239 (n,f) at ~ 1 keV, k-eff is very sensitive to that reaction at much higher energies, ~ 100 keV. Then, sodium void benchmarks revealed as appropriate to check performance of ²³⁹Pu at different energy ranges than the relevant in k-eff.

An analysis with NDaST perturbing JEFF-3.3 nuclear data with respect JEFF-3.1.1., allowed to conclude that ²³⁹Pu capture around 1 keV was the main responsible for the differences in the sodium void prediction with JEFF-3.3 and JEFF-3.1.1 The improved biases with JEFF-4T3 indicates an improvement of ²³⁹Pu cross-sections around ~1 keV.

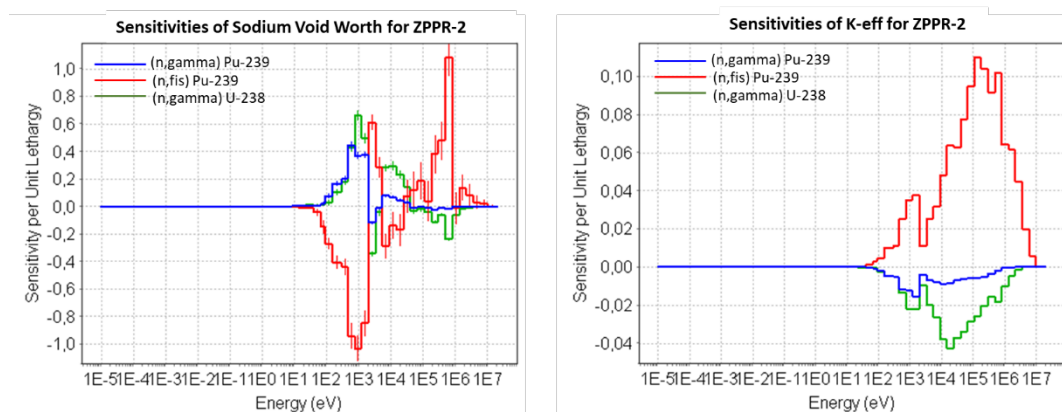


Figure 12. Main sensitivity profiles for sodium void (left) and multiplication factor (right) for ZPPR-2.

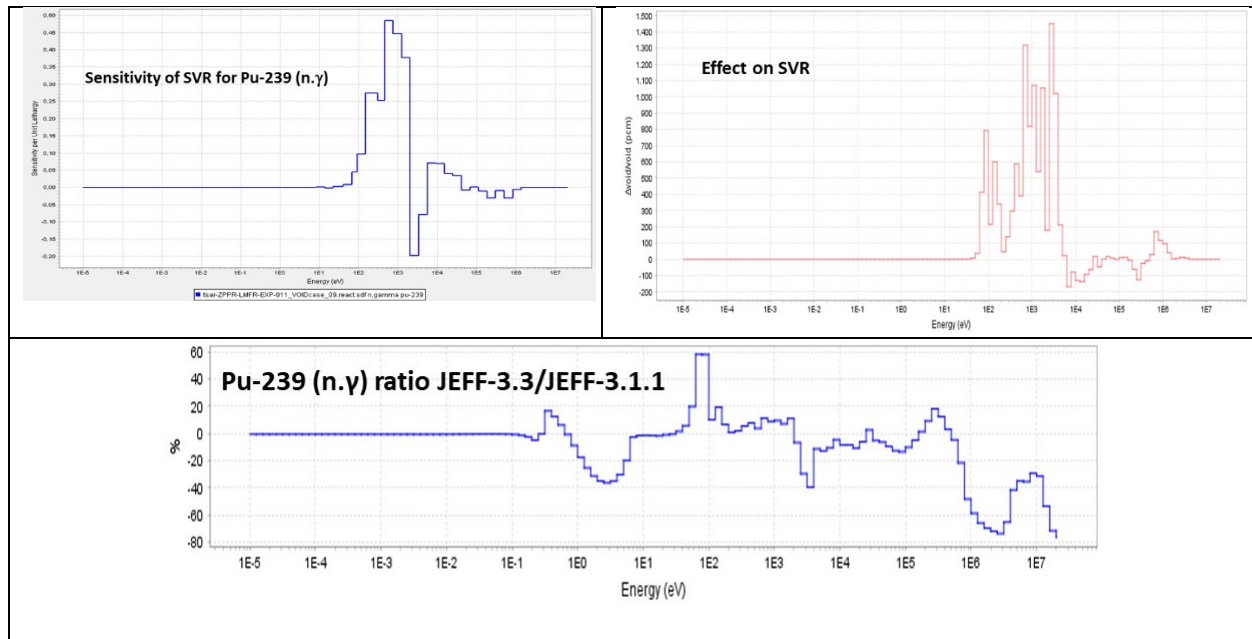


Figure 13. Sensitivity profile for ZPPR-2 sodium void to Pu-239 capture, ratio of the Pu-239 capture between JEFF-3.3 and JEFF-3.1.1 and impact of the perturbation on the sodium void worth.

3.3. Analysis of SEFOR experiments

The Southwest Experimental Fast Oxide Reactor (SEFOR) was a 20 MWth sodium-cooled experimental facility that operated between 1969 and 1972 [Meyer, 1970]. Its extensive experimental program included, among others, isothermal tests so that Doppler reflector worth measurements are available and can be used for nuclear data validation. Some key characteristics:

- Reactor fueled with mixed PuO₂-UO₂. Reflector composition: Ni (95.5%), Fe(2.5%)
- There are no control rods, but reactivity was controlled by adjusting the position of the reflector surrounding the active core. The reflector was segmented in 10 movable parts; each part being axially moved to compensate reactivity
- Doppler measurements are available for configurations Core I-E and Core II-E
- Reflector reactivity worth measurements are available for configuration Core I-E

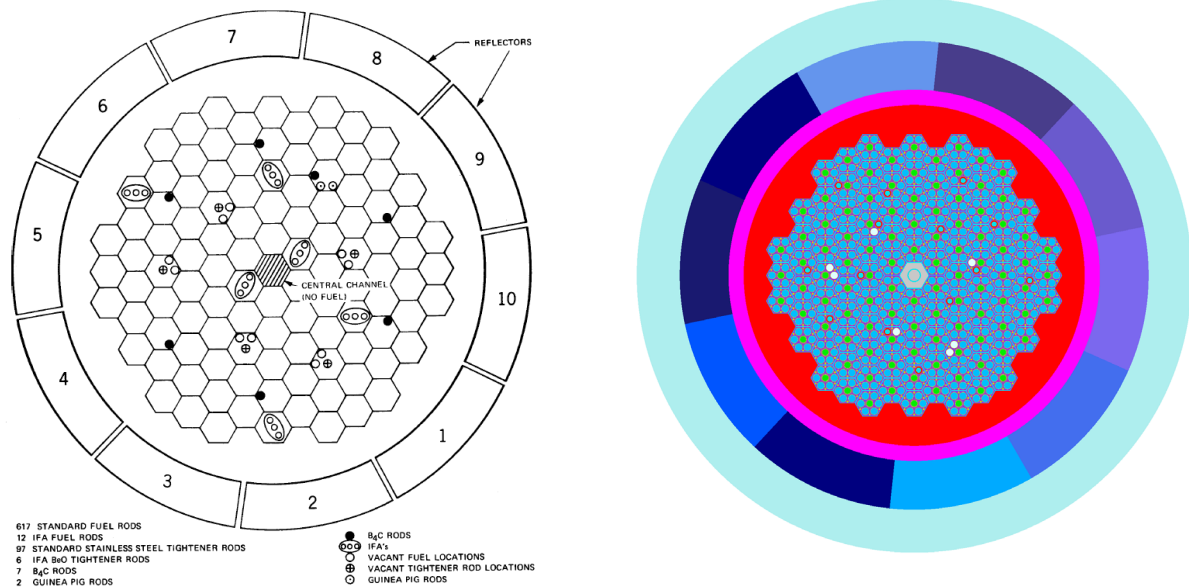


Figure 14. Schematic top view of SEFOR Core I-E (left) and KENO-VI model (right).

A detailed model for Core I-E configuration and a R-Z model for Core II-E configuration were developed for the Monte Carlo code KENO-VI/SCALE6.2.3. A schematic view of the reactor, as well as a top view of the developed model for Core I-E are displayed in Figure 14. Criticality calculations were performed with statistical uncertainties in k -eff of about 5 pcm. Sensitivities were computed with TSUNAMI-3D CE /SCALE6.2.3 in 33 energy groups. The following nuclear data libraries were processed with AMPX: JEFF-3.1.1, JEFF-3.3, JEFF-4T2.2, JEFF-4T3 and the ENDF/B-VII.1-based library provided with SCALE was also used.

It is worth it to mention that Core I-E configuration contains 108 fuel subassemblies with a central BeO pellet. When processing JEFF libraries with AMPX, there was an issue with Be-9, since the description of (n,2n) reaction in the ^9Be ENDF-6 files for JEFF-x is carried out by means of its partial reactions (i.e., MT875+ reaction channels) without including the total (n,2n) reaction. Although AMPX can deal with those channels, it does not reconstruct the total (n,2n) reaction, so that AMPX-processed JEFF data is not suitable for ^9Be . Therefore, data for ^9Be from ENDF/B-VII.1 was taken.

For the R-Z Core II-E configuration, Doppler results are shown in Table 10. They are the result of comparing reactivities for "cold" state (677K) and "hot" state (1365K for fuel sub-assemblies, the rest at 677K). A degradation of C/E could be observed for JEFF-3.3. A detailed analysis showed compensation effects involving mostly ^{238}U , ^{239}Pu , ^{16}O and ^{23}Na . A perturbation analysis of JEFF-3.3 with respect to JEFF-3.1.1 using NDaST led to spot a significant impact of the ^{238}U capture cross section around 1 keV, as illustrated in Figure 15, Figure 16, and Figure 17. This allowed to identify a typo for the 808 eV p-wave G_g parameter displayed in Figure and Figure 18 [Jiménez-Carrascosa, 2021]. Calculations with JEFF-4T3 exhibit a very good agreement with benchmark values.

Table 10. Results for SEFOR Doppler benchmark for Core II-E (R-Z model). Doppler effect from 677 K to 1365 K.

Core II-E	JEFF-3.1.1	JEFF-3.3	JEFF-3.3+U238update	JEFF-4T3
$\Delta\rho$ (pcm)	-474.4	-497.1	-483.0	-469.2
Doppler constant	-676.6	-708.9	-688.7	-669.2
C/E	1.010	1.058	1.028	0.999

For the detailed Core I-E configuration, Doppler results are shown in Table 10 when comparing reactivities when fuel temperature goes from 449 K to 667K. Results provided by JEFF-4T3 are very similar to those predicted by JEFF-3.1.1.

Table 11. Results for SEFOR Doppler benchmark for Core I-E (Detailed model). Doppler effect from 449K to 677K.

Core I-E	JEFF-3.1.1	JEFF-3.3	JEFF-4T2	JEFF-4T3
$\Delta\rho$ (pcm)	-369	-388	-357	-367
Doppler constant	-266	-279	-258	-264
C/E	0.97	1.02	0.94	0.96

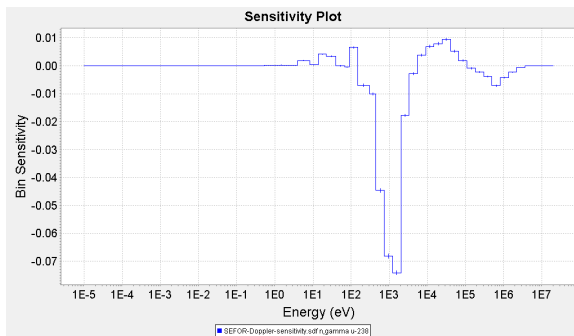


Figure 15. Schematic top view of Sensitivity of Doppler effect to $^{238}\text{U}(n,\gamma)$.

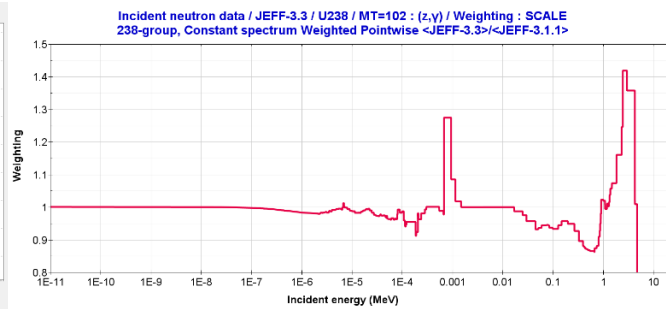


Figure 16. Perturbation of $^{238}\text{U}(n,\gamma)$ cross sections between JEFF-3.3 and JEFF-3.1.1.

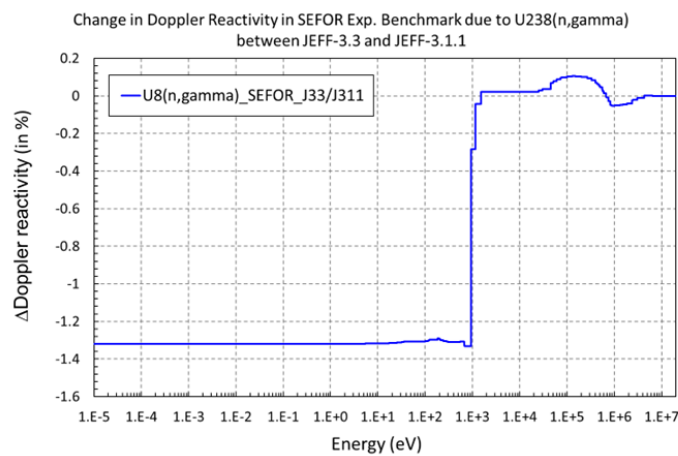


Figure 17. Change in Doppler reactivity due to the $^{238}\text{U}(n,\gamma)$ perturbation.

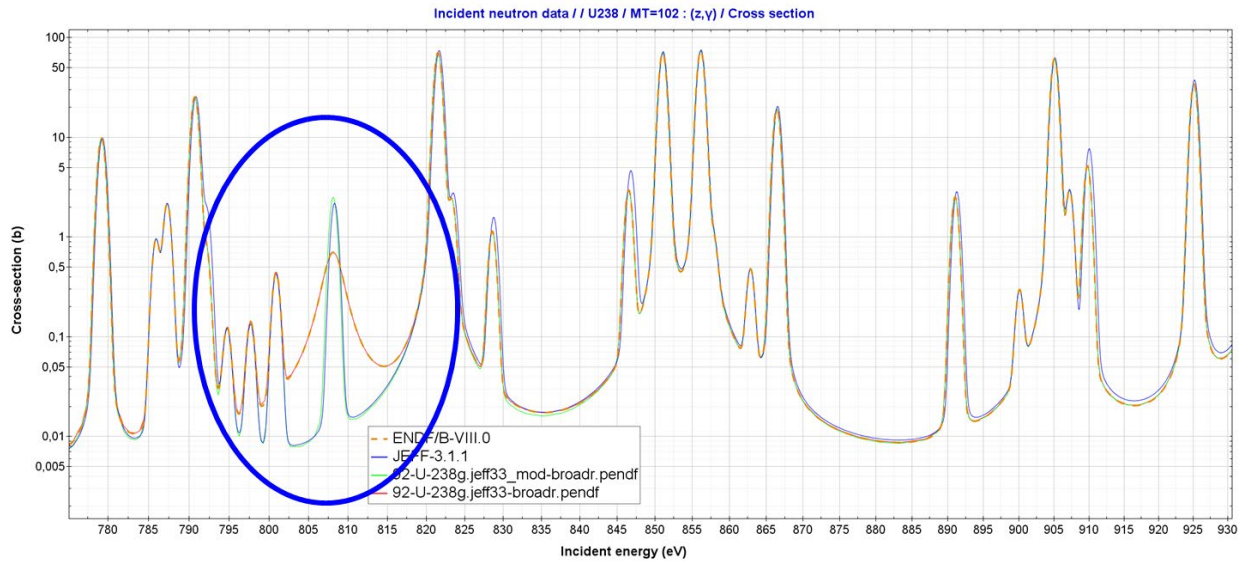


Figure 18. ^{238}U (n,γ) cross sections in the range around 800 eV.

Finally, a comparison of C/E values for reflector reactivity worth for configuration Core I-E is shown in Figure 19. Results predicted by all JEFF libraries are very similar, corresponding the highest biases to ENDF/B-VII.1 library. A sensitivity analysis showed a high impact of ^{239}Pu (n,fis) and nubar as well as elastic cross sections of ^{56}Fe and ^{58}Ni [García-Herranz, 2023].

Regarding the calibration curve of fine reflector R3, a comparison to the experimental curve was performed. Two different initial positions of the movable reflectors were documented: at 0 cm above the core and at 8.73 cm above the core, so both configurations were modelled. Neutron spectrum softens as reflector segment is moving upward, as illustrated in Table 12, so these experiments could be useful to identify trends with spectrum for Pu, Fe and Ni validation. Results are in Figure 20, where predictions with different libraries differ when spectrum softens. However, more investigations are required to determine the real reflector configuration and obtaining the most of these experiments.

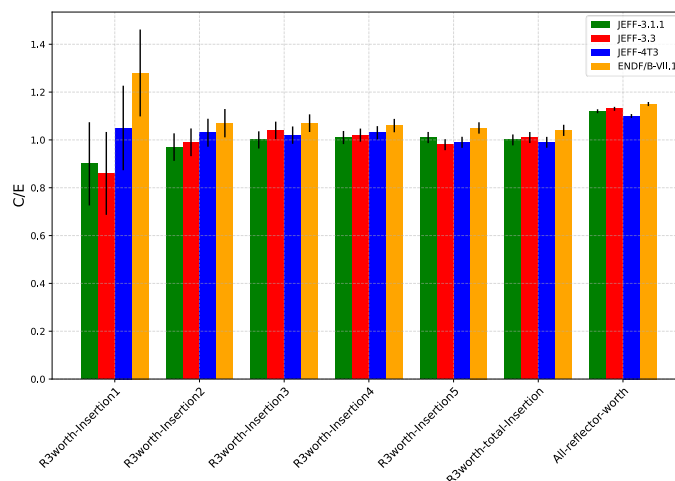


Figure 19. C/E for reflector worth in SEFOR Core I-E configuration.

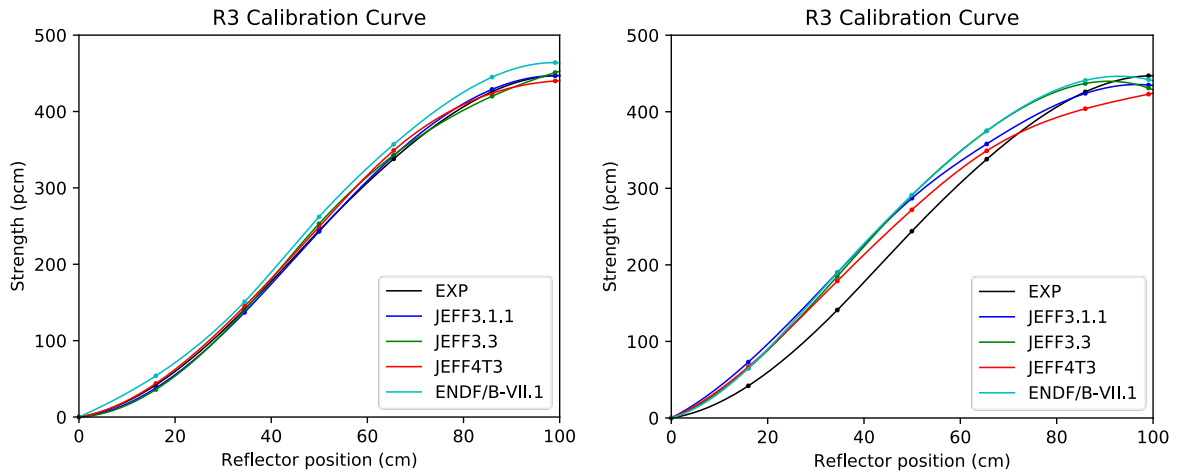


Figure 20. Calibration curves for movable fine reflector R3 in SEFOR Core I-E configuration. Initial position of reflector corresponds to 0 cm (left) and 8.73 cm (right).

Table 12. EALF values (keV) as reflector segment is moving upward.

R3 position (from bottom)	EALF (keV)
0 cm	93.83
16 cm	93.52
34 cm	92.98
50 cm	92.42
65 cm	91.86
86 cm	91.34
99 cm	91.18
All Reflectors down	110.45
All Reflectors up	87.33

4. Thermal reactors *C/E* validation and nuclear data trends (UPM, NRG)

4.1. Analysis performed at UPM: KRITZ benchmarks

IRPhEP Handbook provides a comprehensive set of thermal reactor benchmarks that can be used for nuclear data validation. In particular, the light water moderated lattice experiments at room and elevated temperatures carried out at KRITZ reactor have been assessed. The KRITZ reactor operated at Studsvik, Sweden, during the first half of the nineteen-seventies to support the Swedish nuclear power reactor program.

KRITZ experiments have been chosen with the goal of extending validation with benchmarks sensitive to ^{238}U and ^{239}Pu capture reactions in the thermal range and adequate to identify trends with temperature. The analysed experiments include:

- KRITZ-LWR-RESR-001, 002 and 003
- KRITZ-LWR-RESR-004 (extensive series of measurements provided by KRITZ-1-Mk experiment)

4.1.1. KRITZ-LWR-RESR-001, -002 and -003

These experiments, performed in the period from September 1972 through February 1973, included a series of criticality experiments on light water moderated lattices with uranium rods, mixed-oxide rods or both, at room temperature and at temperatures up to $\sim 250\text{ }^\circ\text{C}$.

Several series of experiments were performed: KRITZ-2:1 (with UO_2 pins in a square lattice with 14.85 mm pin spacing), KRITZ-2:13 (with UO_2 pins in a wider lattice with 16.35 mm pin spacing) and KRITZ -2:19 with (UO_2 , PuO_2)-rods in further widened lattice with 18.00 mm pitch. More details are given in Table 13 and a schematic view is in Figure 21.

Table 13. Summary of analyzed KRITZ-LWR-RESR- benchmarks.

Core	Fuel type	Array size	Cold pitch (cm)	Temp ($^\circ\text{C}$)	Boron (ppm)
KRITZ-2:19	MOX fuel pins	25x24	1.800	21.1	4.8
KRITZ-LWR-RESR-001	1.50wt% PuO_2 in fuel 91.41 at% $\text{Pu}239$ Clad Zircaloy			235.9	5.2
KRITZ-2:1	UO_2 fuel pins	44x44	1.485	19.7	217.9
KRITZ-LWR-RESR-002	1.86wt% $\text{U}235$ Clad Zircaloy			248.5	26.2
KRITZ-2:13	UO_2 fuel pins	44x40	1.635	22.1	451.9
KRITZ-LWR-RESR-003	1.86wt% Clad Zircaloy			243.0	280.1

- KRITZ-LWR-RESR-001

It corresponds to the experiment labelled KRITZ-2:19, with mixed-oxide rods at 18.00 mm pitch.

- KRITZ-LWR-RESR-002

The objective of the KRITZ 2:1 experiment was to attain criticality of a rectangular array of mixed-oxide zircaloy-2 clad fuel rods in light water by regulating the concentration of boron in water and by adjusting the water level. Criticality was achieved at isothermal conditions at room temperature ($19.7\text{ }^\circ\text{C}$) and at elevated temperature ($248.5\text{ }^\circ\text{C}$).

- KRITZ-LWR-RESR-003

The objective of the KRITZ 2:13 experiment was to attain criticality of a rectangular array of mixed-oxide zircaloy-2 clad fuel rods in light water. Criticality was achieved at isothermal conditions at room temperature (22.1 °C) and at elevated temperature (243.0 °C).

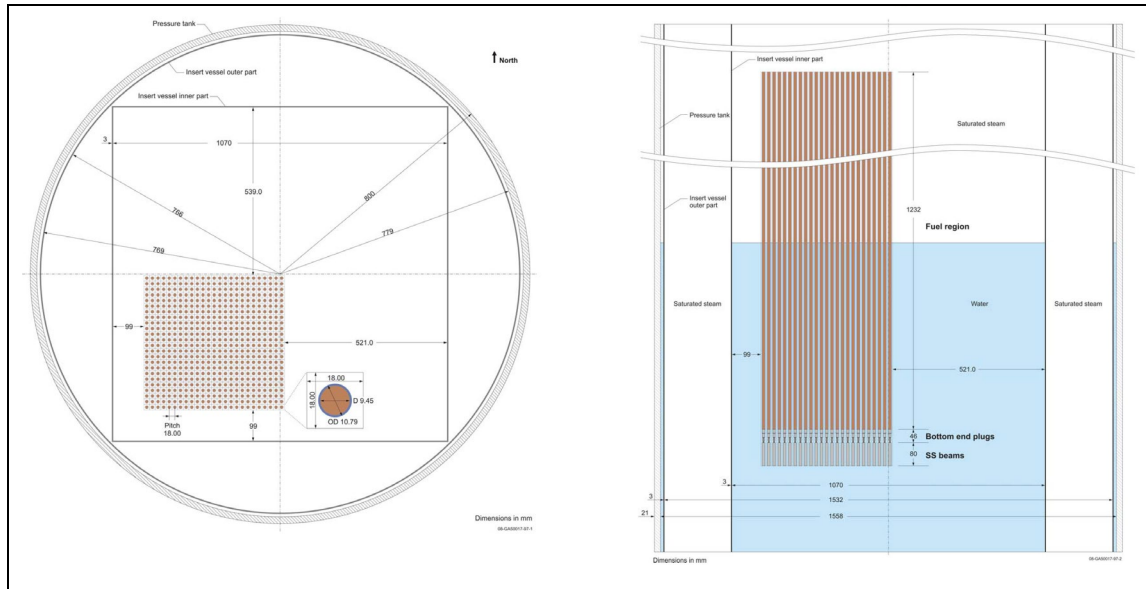


Figure 21. Schematic top and side views of the KRITZ core [Kodeli, 2009]

Calculations were performed with MCNP-6.1 code with three different evaluations: JEFF-3.3, JEFF-3.1.1 and ENDF/B-VIII.0. Results for KRITZ-001, -002 and -003 are shown in Table 14, Table 15 and Table 16 respectively. For KRITZ-001 large biases were found, especially for JEFF-3.3 at high temperature; these results are similar to the ones reported with MONK calculations in [Ware, 2020]. When using ^{239}Pu from ENDF/B-VIII.0 in [JEFDOC-2250], biases reduced and the trend with temperature was no longer observed, suggesting the need of reviewing ^{239}Pu in JEFF-3.3. For KRITZ-002 and KRITZ-003 biases with JEFF-3.3 were lower, differing at cold and hot temperatures for KRITZ-002 and being similar at cold and hot for KRITZ-003.

Bias C-E analysis with uncertainty quantification

Table 14. Summary of results for KRITZ-2:19 (KRITZ-LWR-RESR-001) and C/E biases.

	KRITZ2:19 at 21.1°C (cold)		KRITZ2:19 at 235.9 °C (hot)		KRITZ2:19 at 21.1°C	KRITZ2:19 at 235.9 °C	$\Delta C/E(C-H)$
	keff	$\Delta keff$	keff	$\Delta keff$	(C/E-1) in pcm	(C/E-1) in pcm	
Benchmark model	1.00770	0.00300	1.00550	0.00270	-	-	
MCNP6.1-JEFF-3.3	0.99993	0.00008	0.99553	0.00008	-771	-992	-220
MCNP6.1-JEFF-3.1.1	1.00029	0.00007	1.00022	0.00008	-735	-525	210
MCNP6.1-ENDFB80	0.99945	0.00007	0.99888	0.00008	-819	-658	160
MONK10B-JEFF-3.1.2 (JEFDOC-1998) [Ware, 2020]	1.00090	0.00020	1.00060	0.00020	-675	-487	187
MONK10B-JEFF-3.3 (JEFDOC-1998) [Ware, 2020]	1.00030	0.00020	0.99540	0.00020	-734	-1004	-270
MONK10B-JEFF-3.3+Pu9E80 (JEFDOC-2250, T. Ware)	1.00290	0.00020	1.00170	0.00020	-476	-378	98

Table 15. Summary of results for KRITZ-2:1 (KRITZ-LWR-RESR-002) and C/E biases.

	KRITZ2:1 at 19.7°C		KRITZ2:1 at 248.5 °C		KRITZ2:1 at 19.7°C	KRITZ2:1 at 248.5 °C	$\Delta C/E(C-H)$
	keff	$\Delta keff$	Keff	$\Delta keff$	(C/E-1) in pcm	(C/E-1) in pcm	
Benchmark model	1.00250	0.00200	1.00240	0.00280	-	-	
MCNP6.1-JEFF-3.3	1.00076	0.00008	1.00294	0.00008	-174	54	227
MCNP6.1-JEFF-3.1.1	0.99834	0.00008	0.99910	0.00008	-415	-329	86
MCNP6.1-ENDF/B-VIII.0	0.99812	0.00008	0.99958	0.00008	-437	-281	156

Table 16. Summary of results for KRITZ-2:13 (KRITZ-LWR-RESR-003) and C/E biases.

	KRITZ2:13 at 22.1°C		KRITZ2:13 at 243.0 °C		KRITZ2:13 at 22.1°C	KRITZ2:13 at 243.0 °C	$\Delta C/E(C-H)$
	keff	$\Delta keff$	Keff	$\Delta keff$	(C/E-1) in pcm	(C/E-1) in pcm	
Benchmark model	1.00130	0.00100	1.00190	0.00200	-	-	
MCNP6.1-JEFF-3.3	1.00201	0.00008	1.00261	0.00008	71	71	0
MCNP6.1-JEFF-3.1.1	1.00056	0.00008	0.99875	0.00007	-74	-314	-240
MCNP6.1-ENDF/B-VIII.0	1.00062	0.00008	0.99952	0.00008	-68	-238	-170

The uncertainty quantification due to nuclear data uncertainties was also performed using NDaST tool. Results are shown in Table 17. The KRITZ-2:19 (MOX fuel) shows large uncertainty in ENDF/B-VIII.0, mainly due to $^{239}\text{Pu}(n,\gamma)$ uncertainties. Sensitivity profiles for KRITZ-1 are illustrated in Figure 22 while Figure 23 shows the relative standard deviation for the $^{239}\text{Pu}(n,\gamma)$. It seems that the ~4% uncertainty for the ENDF/B-VIII.0 greater than 2.5% in JEFF-3.3% may explain these differences.

Table 17. Uncertainties in keff (in pcm) due to ND uncertainties in ^{235}U , ^{238}U and ^{239}Pu (except for nubar and PFNS) for JEFF-3.3 (J33) and ENDF/B-VIII.0 (E80).

Core	Case	All		^{238}U		$^{238}\text{U}(n,\gamma)$		^{239}Pu		$^{239}\text{Pu}(n,\gamma)$	
		J33	E80	J33	E80	J33	E80	J33	E80	J33	E80
KRITZ-2:19	Cold	496	971	203	166	139	138	452	956	472	828
KRITZ-LWR-RESR-001	Hot	583	1142	233	172	136	135	534	1129	552	980
KRITZ-2:1	Cold	456	312	328	267	234	232	0	0	0	0
KRITZ-LWR-RESR-002	Hot	486	347	370	302	264	262	0	0	0	0
KRITZ-2:13	Cold	449	307	303	241	206	205	0	0	0	0
KRITZ-LWR-RESR-003	Hot	460	327	325	265	232	231	0	0	0	0

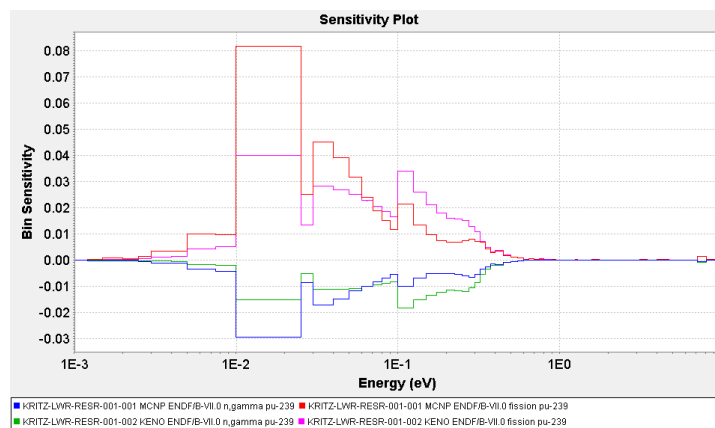


Figure 22. KRITZ-2:19 sensitivity coefficients (left).

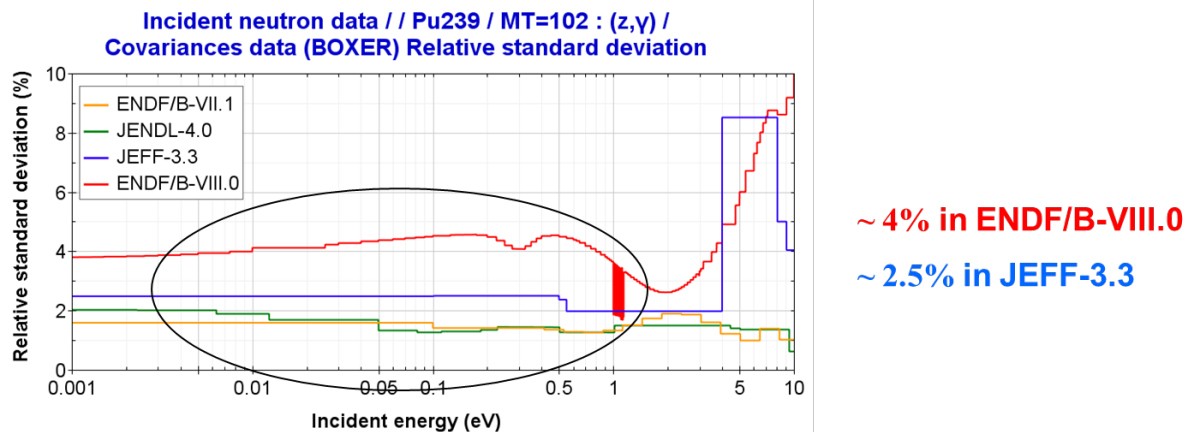


Figure 23. Relative standard deviation for ^{239}Pu (n,γ).

4.1.2. KRITZ-4

KRITZ-4 consisted of a pressure tank that allowed full size reactor fuel rods and assemblies. Criticality at stable conditions was obtained by adjusting the measured water level, leading to four series of configuration varying between 20 °C and 250 °C. These four series were based on three fuelled core configurations, one of which had two different boron mass fractions. Then, temperature was the only variable to be varied for 37 critical measurements:

- Series 1: 9 cases with array 39x39 fuel rods at 41° C - 226° C. Boron=0.8 ppm
- Series 2: 4 cases with array 46x46 fuel rods at 90° C - 246° C. Boron=46.3 ppm
- Series 3: 11 cases with array 46x46 fuel rods at 22° C - 205° C. Boron=175 ppm
- Series 4: 13 cases with array 39x39 fuel rods at 20° C - 244° C. Boron=0.2 ppm

The description of this benchmarks is included in the IRPHEP “KRITZ-LWR-RESR-004 Evaluation Report. 2019 Rev.0”. As mentioned, it contains 37 criticality measurements at room and elevated temperatures (critical water heights of active fuel covered by water), with UO_2 fuels 1.35wt% in ^{235}U .

An extensive work of these benchmarks has been performed within the nuclear criticality safety community [Mennerdahl, 2020] concluding that:

- correlations between measurements were very strong, $c_k > 0.95$
- a priori uncertainty due to nuclear data uncertainties ~600 pcm
- the totally dominating nuclear data adjustment is ^{238}U (n,γ)

Calculations at UPM [Cabellos, 2021b] were performed with KRITZ4 simple models for KENO-VI/SCALE6.2.3, using JEFF-3.3 and JEFF-3.1.1 nuclear data libraries processed with AMPX/SCALE6.3b11 [Jiménez-Carrascosa, 2021b] and employing on-the-fly doppler broadening (DBX=2 option). A summary of results is shown in Figures 12 to 14. Comparisons with MORET calculations reported in IRPHEP are also included (KRITZ4 simple models, MORET5.D.1 Monte Carlo code, processed libraries JEFF-3.3 and ENDF/B-VIII.0 with GAIA1.1.1 tool, TSLs available in ENDF files).

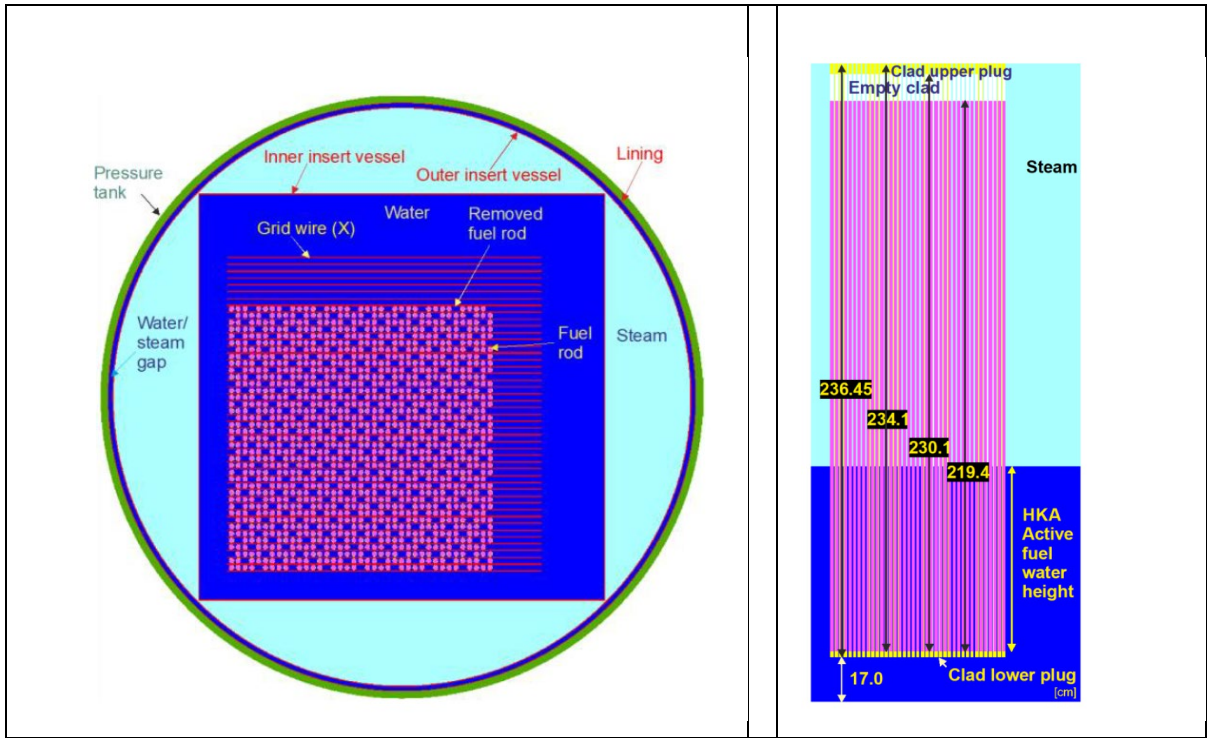


Figure 24. Relative Schematic top and side views of the core are presented [Mennerdahl, 2020]

Bias C-E analysis and trend analysis

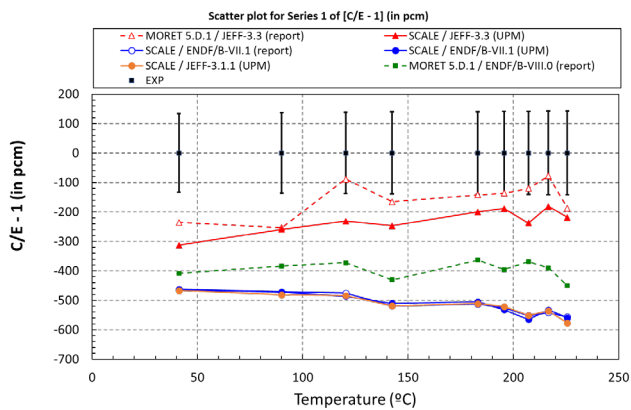


Figure 25. C/E for KRITZ4/Series1.

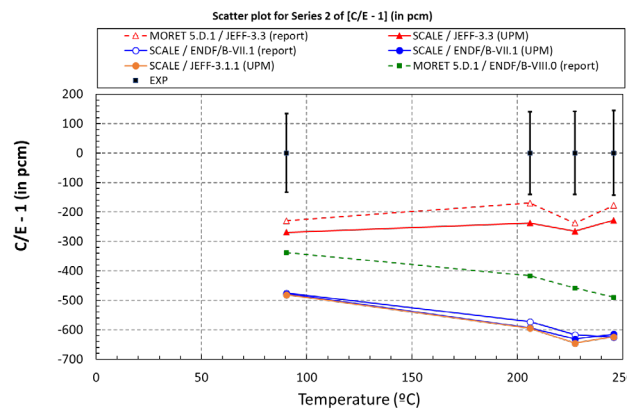


Figure 26. C/E for KRITZ4/Series2

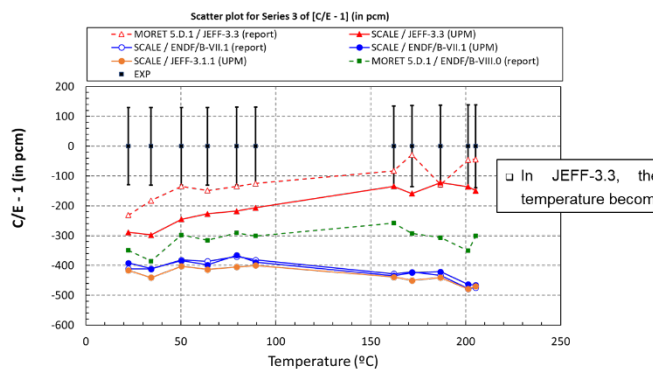


Figure 27. C/E for KRITZ4/Series3

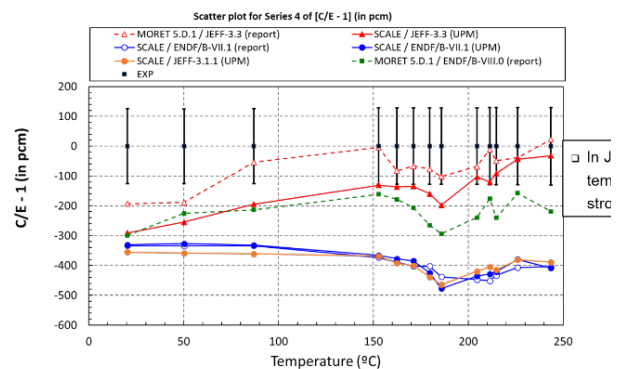


Figure 28. C/E for KRITZ4/Series4

KRITZ calculations with different codes (by different organizations) showed consistent trends in the results. Results for detailed and simple models appear to be consistent (see IRPhEP KRITZ-LWR-RESR-004 Evaluation Report. 2019 Rev.0).

An analysis of JEFF-3.1.1- and ENDF/B-VII.1-based results shows:

- Biases for JEFF-3.1.1 are very similar to those observed for ENDF/B-VII.1 library, for which systematic deviations from 400 to 600 pcm are obtained when comparing to experimental values. The agreement between JEFF-3.1.1 and ENDF/B-VII.1 is consistent with previous comparisons for thermal spectrum low-enriched uranium benchmarks.
- Smaller biases are observed for the most thermalized series of measurements (lower temperatures), although no strong trend with temperature is observed.

An analysis of JEFF-3.3- and ENDF/B-VIII.0-based results shows:

- JEFF-3.3 deviations from experimental values strongly reduce with temperature, exhibiting remarkable trends with temperature. This strong trend may indicate remaining nuclear data biases in JEFF-3.3. A detailed perturbation analysis allowed to conclude that this effect can be mainly due to the reversed effect, dominated by the fission cross section.
- It is worth it to compare results using JEFF-3.3 library provided by MORET 5.D.1 and SCALE. For Series 1, unstable deviations between 10 and 140 pcm are observed between both codes, with no trends that may be associated to temperature variation. This is also found for the other Series, for which deviations are always below 140 pcm. Those differences can be attributed to code effect or modelling inconsistencies since similar trends have been reported between MORET and MCNP codes, both using ENDF/B-VIII.0 library.

Perturbation analysis

Additionally, a perturbation analysis using NDaST is performed to identify the main nuclear data contributors to the strong positive trend with temperature observed for Series 4. Perturbations of ^1H , ^{16}O , ^{238}U and ^{235}U cross-sections were carried out and the impact on k-eff was examined. For Case25 (20 $^{\circ}$) and Case27 (243.6 $^{\circ}$), the effect of perturbations in JEFF3.3 and ENDF/B-VIII.0 with respect to ENDF/B-VII.1 are shown in Table 18 and Table 19 respectively, while the impact of perturbations in JEFF3.3 with respect to JEFF-3.1.1 are in Table 20.

In Table 18, for Case 25 (20.4 $^{\circ}$ C), a perturbation in ^{238}U increases reactivity in +176 pcm while a perturbation in ^{235}U decreases reactivity in -128 pcm. For Case37 (243.6 $^{\circ}$ C), the impact of ^{238}U perturbation is +218 pcm, and the impact of ^{235}U perturbation is +162 pcm. Thus, the reversed ^{235}U effect dominates the temperature trend, which is in agreement with [Mennerdahl, 2021].

Table 18. Δk_{eff} due to perturbations in nuclear data (J33/E71) data for KRITZ4/Case25 and Case27.

JEFF-3.3/ ENDF/B-VII.1														Total
H1 (n,n)	H1 (n,g)	O16 (n,n)	O16 (n, α)	U5 (n,fission)	U5 (n,g)	U5 nubar	U5 PFNS	U8 (n,n)	U8 (n,n')	U8 (n,fission)	U8 (n,g)	U8 nubar		
Case25 20.5 $^{\circ}$ C	0	0	0	0	404	-139	-432	40	5	3	-3	157	13	48
Case37 243.6 $^{\circ}$ C	0	0	0	0	738	-203	-428	55	6	-1	-5	200	15	380
Diff.	0	0	0	0	334	-65	4	15	1	-4	-1	43	1	332

Table 19. Δk_{eff} due to perturbations in nuclear data (E80/E71) data for KRITZ4/Case25 and Case27.

ENDF/B-VIII.0 / ENDF/B-VII.1														
	H1 (n,n)	H1 (n,g)	O16 (n,n)	O16 (n, α)	U5 (n,fission)	U5 (n,g)	U5 nubar	U5 PFNS	U8 (n,n)	U8 (n,n')	U8 (n,fission)	U8 (n,g)	U8 nubar	Total
Case25 20.5°C	-10	-30	-27	-101	458	-184	-272	105	-2	12	44	112	-30	79
Case37 243.6°C	-11	-24	-28	-104	713	-303	-270	124	-2	13	48	147	-33	276
Diff.	-2	5	-1	-3	256	-119	3	19	1	1	4	35	-4	197

Table 20. Δk_{eff} due to perturbations in nuclear data (J33/J311) data for KRITZ4/Case25 and Case27

JEFF-3.3 / JEFF-3.1.1.														
	H1 (n,n)	H1 (n,g)	O16 (n,n)	O16 (n, α)	U5 (n,fission)	U5 (n,g)	U5 nubar	U5 PFNS	U8 (n,n)	U8 (n,n')	U8 (n,fission)	U8 (n,g)	U8 nubar	Total
Case25 20.5°C	-19	-2	4	24	404	-138	-410	48	-10	-9	22	146	-42	21
Case37 243.6°C	-22	-2	4	25	738	-203	-405	48	-8	-7	24	188	-46	337
Diff.	-3	0	0	1	334	-65	5	0	1	2	2	41	-5	316

Figure 29 shows a sensitivity study for Case25 and Case37. The differences in ENDF/B-VIII.0 and JEFF-3.3 with respect to ENDF/B-VII.1 for $^{235}\text{U}(n,fission)$ between 0.01 eV – 1eV are causing such differences. Figure 30 shows the cumulative change in k_{eff} as a function of the incident neutron energy; the main change appears between 0.05eV and 0.1eV [Cabellos, 2021b].

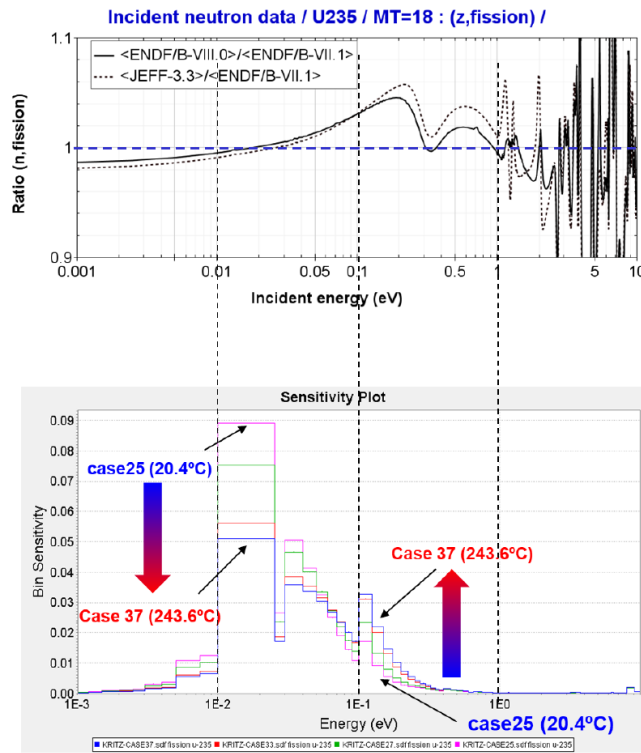


Figure 29. Sensitivity analysis in KRITZ4/Series4 – Case 25 and Case 37. Ratios of $^{235}\text{U}(n,f)$ cross sections in JEFF-3.3 and ENDF/B-VIII.0 with respect to ENDF/B-VII.1 (top) and sensitivity profiles of the multiplication factor to $^{235}\text{U}(n,f)$ for Cases 25 and 37.

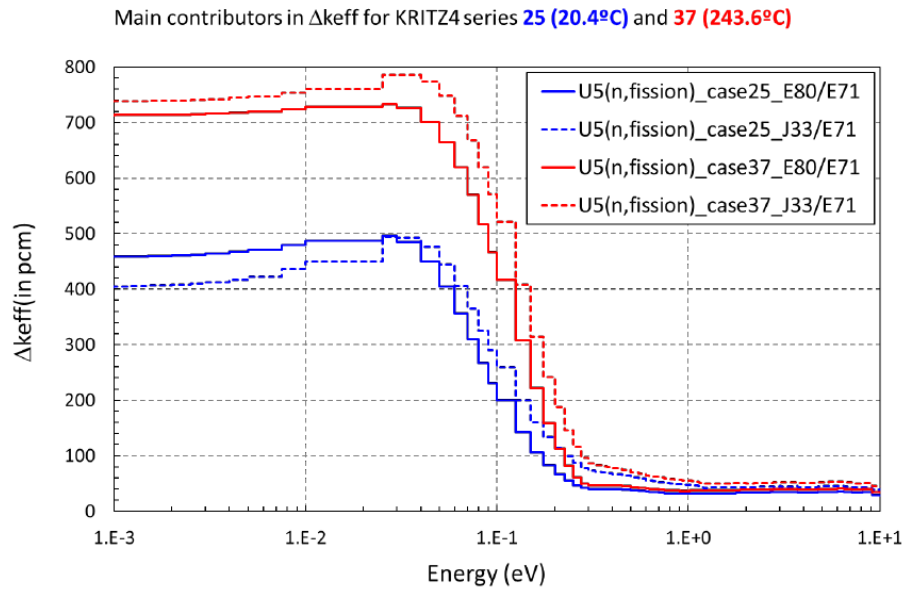


Figure 30. Cumulative Δk_{eff} plot for KRITZ4/Series4 – Case 25 and Case 37.

4.2. Analysis performed at NRG: CREOLE and KRITZ benchmarks

The NRG contribution was calculated using MCNP6.2, only based on neutron data files (i.e. not based on models such as CGM). The ACE files used in the MCNP calculations reported here were all created by processing with NJOY-2016 [MacFarlane 2010]. The 2016 version used here was documented by Muir et al. [2018]. Subversion 2016.20 was used for libraries ENDF/B-VIII.0, JEFF-3.3. For JEFF-4T3, the newer subversion 2016.73 was used. In all cases, NJOY was run for all benchmark temperatures for very nuclide in the benchmark. The thermal scattering data were processed using NJOY at every temperature available in the ENDF file, and subsequently interpolated to the exact benchmark temperatures using MAKXSF, a utility program that is part of the MCNP-6.2 distribution.

The data for CREOLE and KRITZ were analysed in a slightly different way, using reactivity ρ as basic parameter rather than k_{eff} . The rationale for this is to be able to draw conclusions related to the effect that temperature has on reactivity (reactivity feedback). The benchmark experimental value (E) for reactivity was subtracted from the calculated (C) value for every temperature at which benchmark values are available. The results $\Delta\rho = \rho_C - \rho_B$ were plotted as a function of temperature, and fitted to a straight line. The slope of the fitted straight line can be interpreted as a bias in the calculated temperature feedback.

4.2.1. CREOLE-PWR-EXP-001

Results were generated for the CREOLE-PWR-EXP-001 benchmark, based on detailed MCNP-6.2 models of the benchmark, see Table 21. The table shows the trends of C-E with temperature, resulting from a linear fit to the data. In all cases the trend is small, less than or equal to 0.24 pcm/°C in absolute value in all cases. For JEFF-4T3 the results are also shown in Figure 32.

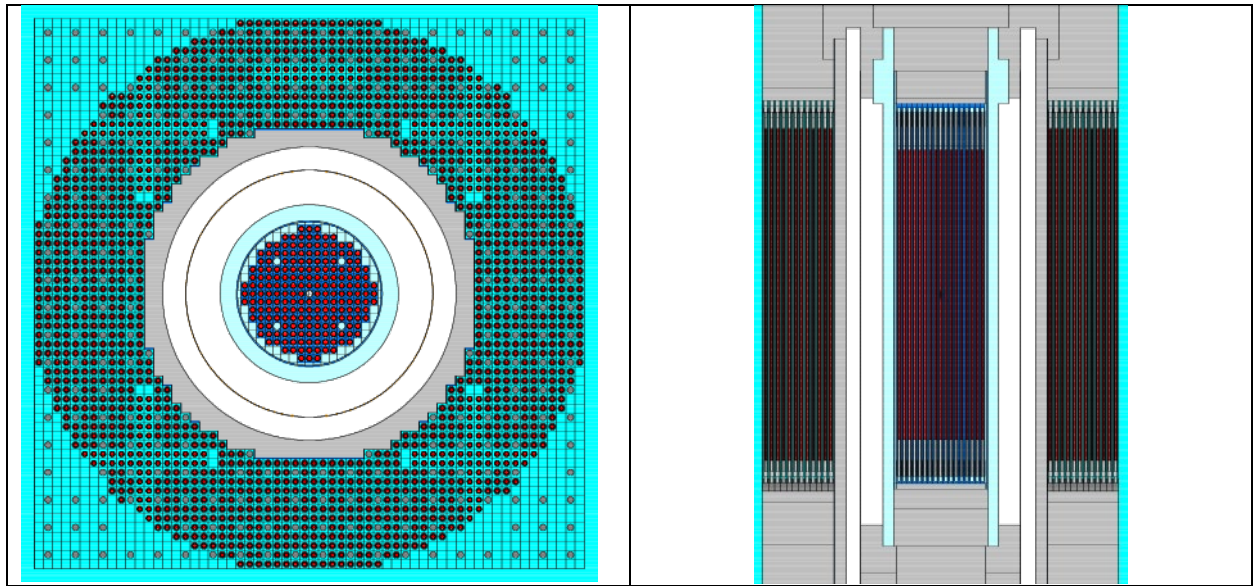


Figure 31. Input model for CREOLE.

Table 21. Results for the fitted trend of C-E reactivity values for CREOLE-PWR-EXP-001.

Results for the trend in $\Delta\rho = \rho_c - \rho_m$	JEFF-4T3 (pcm/°C)	JEFF-3.3 (pcm/°C)	ENDF/B-VIII.0 (pcm/°C)
Core 1: UO ₂ (3.1%) with clean water	0.08 ± 0.02	0.07 ± 0.02	0.13 ± 0.02
Core 2: same but with borated water	0.11 ± 0.03	0.24 ± 0.02	0.15 ± 0.02
Core 3: UO ₂ -PuO ₂	0.17 ± 0.02	0.08 ± 0.03	0.13 ± 0.02
Core 4: same with empty lattice positions	0.13 ± 0.03	0.00 ± 0.03	0.11 ± 0.03

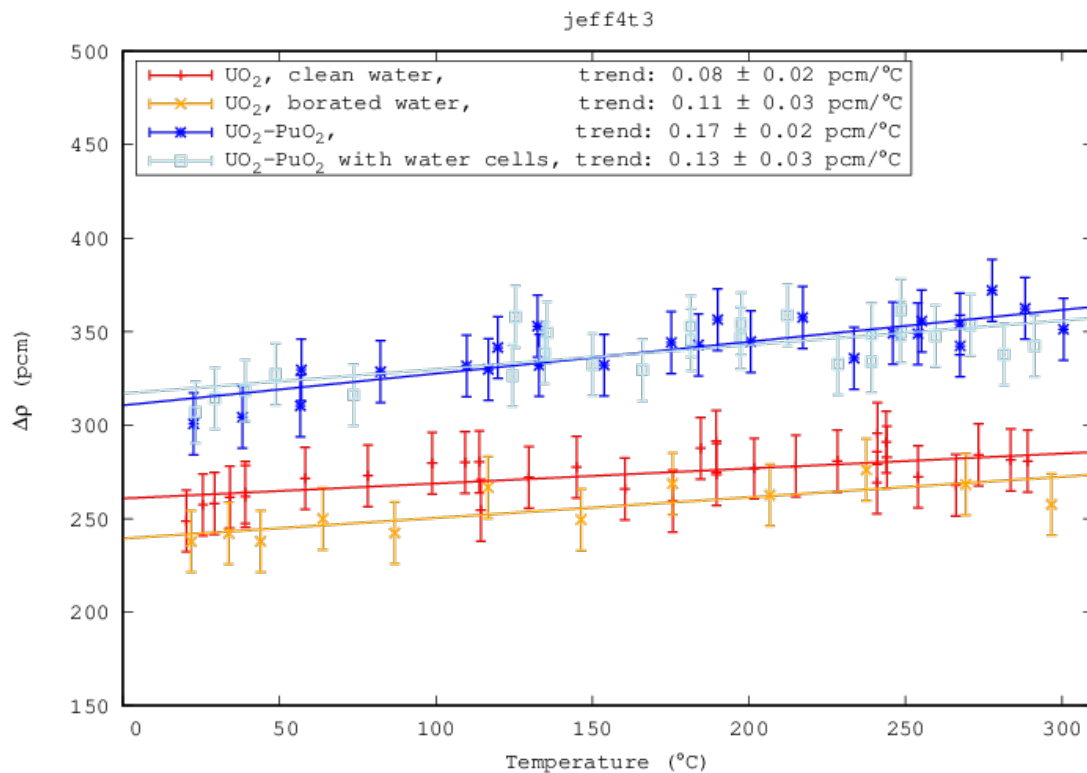


Figure 32. Results with JEFF-4T3 for CREOLE benchmark.

4.2.2. KRITZ-LWR-RESR-001, -002, -003, -004

The benchmarks KRITZ-LWR-RESR-001, 002, 003, and 004 were also analysed with MCNP-6.2, using detailed models for the benchmark cases (see Table 22 and Figure 33). For the KRITZ1 – KRITZ3 benchmarks it is difficult to draw conclusions because there are only two temperature data points in each of these benchmarks, and for KRITZ2 and KRITZ3 moreover the boron concentration is different for the low and high temperature case.

Table 22. Results for the fitted trend of C-E reactivity values for kritz-lwr-resr-001 through -004.

Results for the trend in $\Delta\rho = \rho_c - \rho_m$	JEFF-4t3 (pcm/°C)	JEFF-3.3 (pcm/°C)	ENDF/B-VIII.0 (pcm/°C)
Kritz-1, PuO ₂ -UO ₂ , 25x24, 5 μgB/g	0.52	-1.29	0.42
Kritz-2, UO ₂ (1.86%), 44x44, 218 & 26 μgB/g	-0.64	-0.22	-0.51
Kritz-3, UO ₂ (1.86%), 44x40, 452 & 280 μgB/g	-0.76	-0.06	-0.75
Kritz-4, UO ₂ (1.35%), 39x39, 0.8 μgB/g	-0.15 ± 0.07	0.42 ± 0.08	0.07 ± 0.08
Kritz-4, UO ₂ (1.35%), 46x46, 46.3 μgB/g	-0.73 ± 0.28	0.00 ± 0.19	-0.54 ± 0.24
Kritz-4, UO ₂ (1.35%), 46x46, 175. μgB/g	-0.12 ± 0.11	0.74 ± 0.13	0.29 ± 0.15
Kritz-4, UO ₂ (1.35%), 39x39, 0.2 μgB/g	-0.08 ± 0.13	0.99 ± 0.10	0.35 ± 0.10

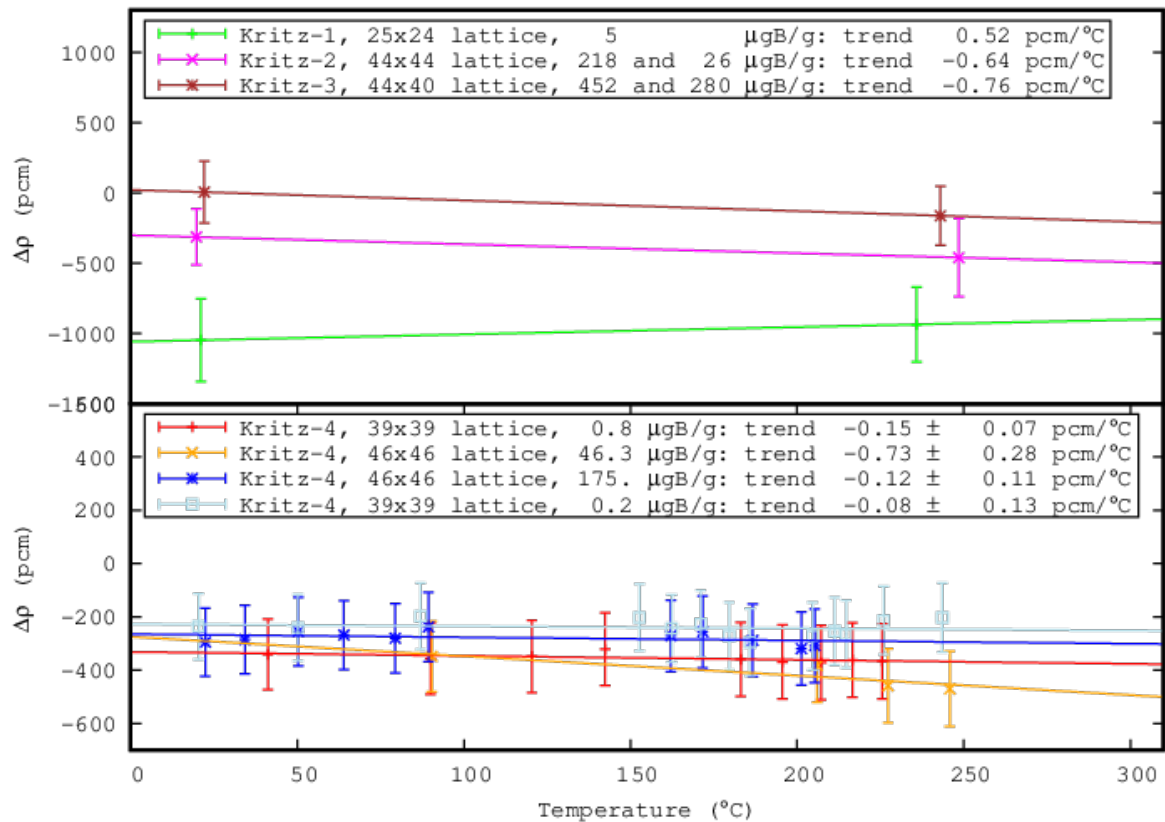


Figure 33. Results for KRITZ benchmark.

5. Commercial Light Water Reactors *C/E* validation and data trends (CEA, UPM)

5.1. Analysis of the critical boron letdown curve (UPM)

At UPM, validation calculations of JEFF libraries for LWRs have been extensively carried out in the past years using the critical boron letdown curve for a typical 3-loop 1000 MWe Westinghouse-type PWR [Plompen, 2020] [Cabellos, 2018], [Cabellos, 2019].

Details of the applied methodology to compute the boron curve follow:

- Calculations performed with SEANAP system [Ahnert, 1998] for LWR core analysis
- 3D/2-group diffusion full core nodal calculations
- Lattice calculations with WIMSD5 code
- Nuclear Data processing with NJOY2016.26 following the WLUP's procedures <https://www-nds.iaea.org/wimsd/>)

To illustrate the evolution of the examined parameter, Figure 34 shows the critical boron letdown curve for a cycle of the mentioned PWR (cycle 5), with three different nuclear data evaluations: JEFF-3.3, JEFF-3.1 and JEF-2.2 (data for neutron induced reactions, neutron thermal scattering library for H in H₂O, decay and fission yield data).

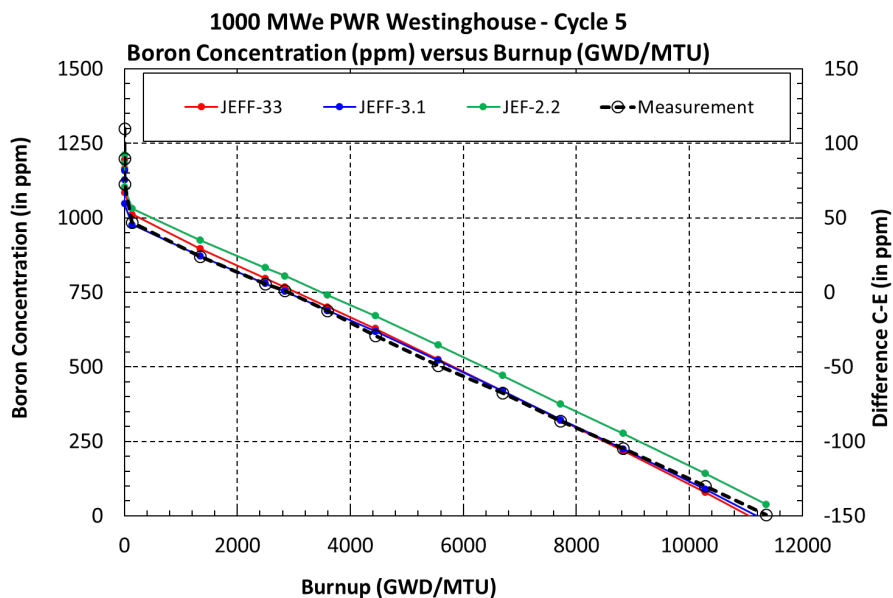


Figure 34. Boron letdown in a typical 1000MWe Westinghouse-type PWR, cycle 5.

Differences between Calculations (C) and Measurements (E) in ppm along the cycle burnup are shown in Figure 35, including also ENDF/B-VIII.0 data library. For JEFF-3.3, the bias is within ± 50 ppm, which is the acceptance criteria for PWR reactors.

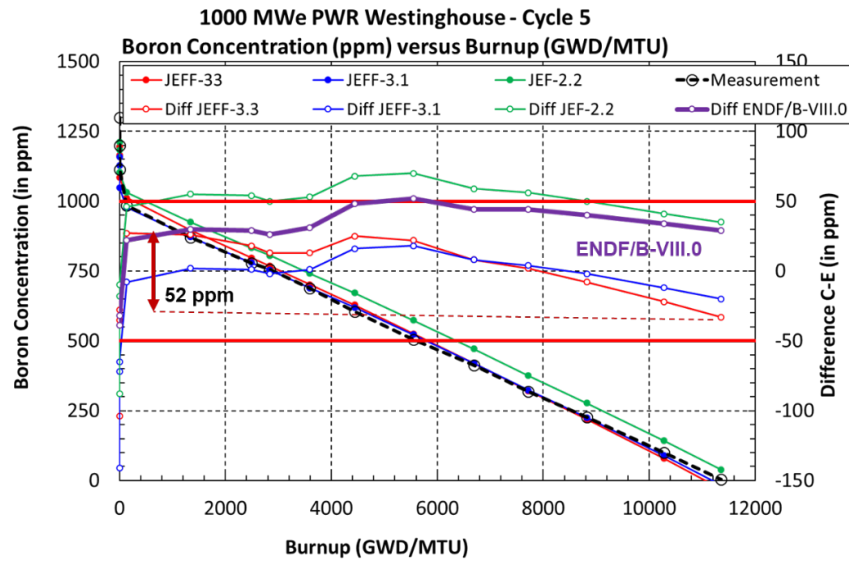


Figure 35. Difference (Calculated – Measurement) in critical Boron let-down in a typical 1000MWe Westinghouse-type PWR, cycle 5, for different libraries (ENDF/B-VIII.0 is highlighted)

An analysis for different consecutive cycles was carried out to assess in-depth the performance of JEFF-3.3 in depletion calculations [Cabellos, 2021]. Figure 36 shows the modification in the boron letdown prediction between JEFF-3.3 and ENDF/B-VII.1 for the first 5 cycles of the PWR under study, taking ENDF/B-VII.1 evaluation as reference. It can be seen that JEFF-3.3 predicts a higher loss-of-reactivity along burnup. Using ENDF/B-VII.1 with some nuclear data from JEFF-3.3 allowed to conclude that deviations are mainly due to the differences in the evaluation of ^{239}Pu , being the impact of ^{238}U and ^{235}U evaluations also significant.

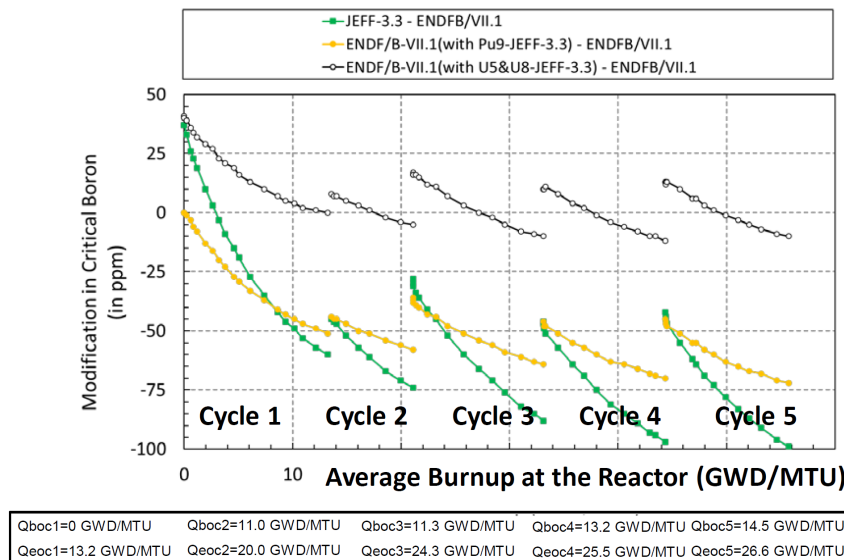


Figure 36. Critical boron modifications (in ppm) at reactor level. Calculations performed with SEANAP system (COBAYA/2D code) for a typical 1000MWe- PWR Westinghouse.

Similar SEANAP-based calculations have been performed to assess JEFF-4 beta evaluations [Astigarraga, 2022] for the first cycle of Almaraz II Spanish Nuclear Power Plant [(IAEA-TECDOC-815, 1995)].

Figure 37 displays a good performance of ENDF/B-VII.1, with differences within the design acceptance of ± 50 ppm. However, JEFF-3.3 clearly exhibits a loss of reactivity along burnup, being ^{239}Pu the most

important contributor to the reactivity loss. The figure also shows a higher deterioration with JEFF-4T2.2, which indicates that more effort for JEFF-4.x is needed to avoid this burnup issue in LWRs.

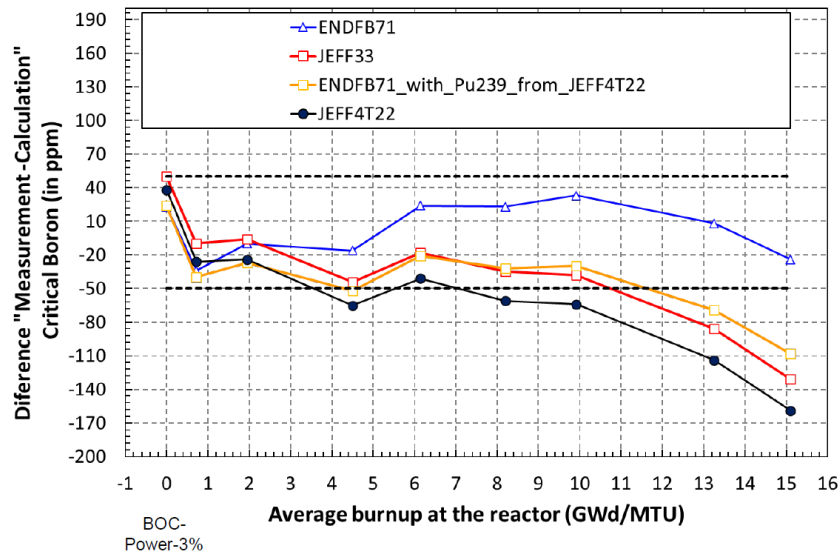


Figure 37. Critical boron differences "Experimental – Calculation" (in ppm) for the Almaraz II, Cycle 1. Calculation performed with SEANAP system.

In Figure 38, the change in the critical boron (in ppm) when using JEFF-3.3 and JEFF-4T2.2 with respect to ENDF/B-VII.1 is shown, clearly showing a larger reactivity loss predicted by JEFF libraries in regards of ENDF/B-VII.1.

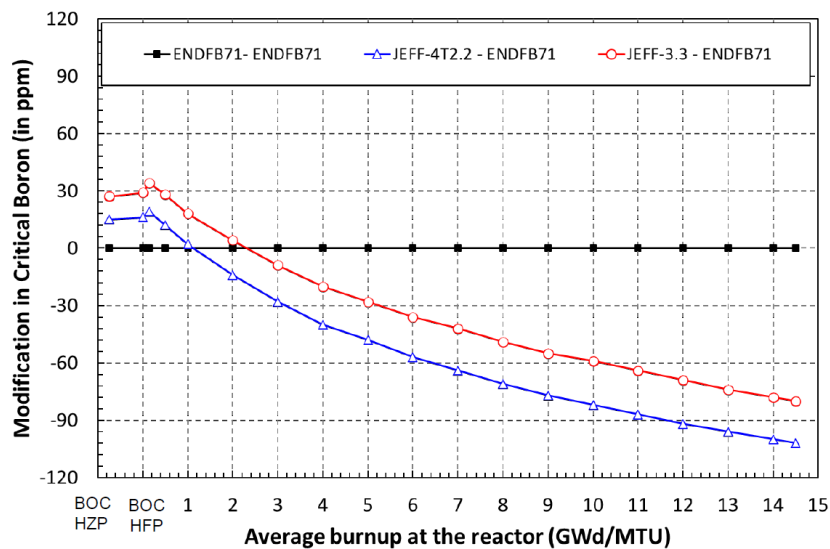


Figure 38. Critical boron modifications (in ppm) in NPP Almaraz II, cycle 1. Calculations performed with COBAYA/2D code.

As it can be seen in Figure 39, the loss-of-reactivity in JEFF-4T2.2 can be attributed mainly to ^{239}Pu and ^{235}U , while the impact of ^{238}U seems to be quite small. At high burnup, contribution of fission products can be also at the origin of discrepancies.

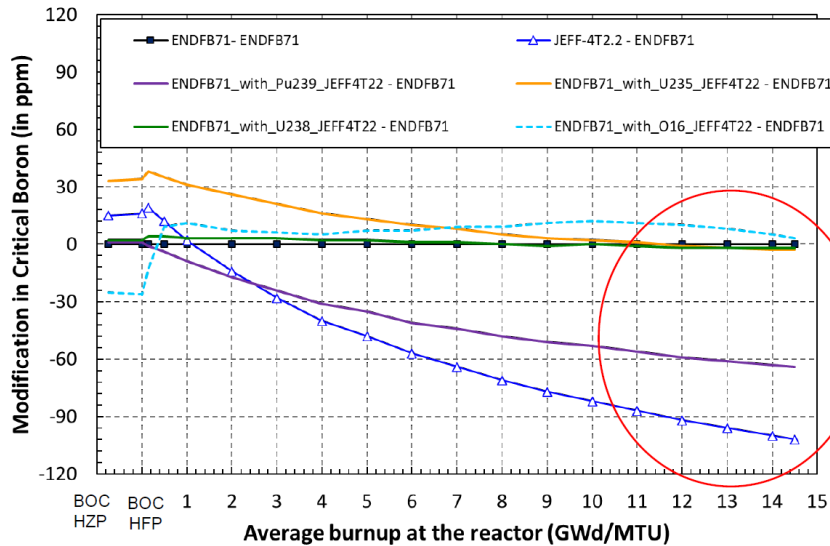


Figure 39. Critical boron modifications (in ppm) in NPP Almaraz II, cycle 1. Calculations performed with COBAYA/2D code.

Updated calculations have been performed with JEFF4-T3 and results are shown in Figure 40 with two different sets of ^{239}Pu , ^{240}Pu and ^{241}Pu (PUs), referring “un” as the new general purpose evaluation and “ad” as the adjusted evaluations using some ICSBEP and burnup calculations. Here, ENDF/B-VII.1 is taken as the reference evaluation. Figure 40 also shows the performance of the new ENDF/B-VIII.1b2 evaluation which is very close to the ENDF/B-VIII.0.

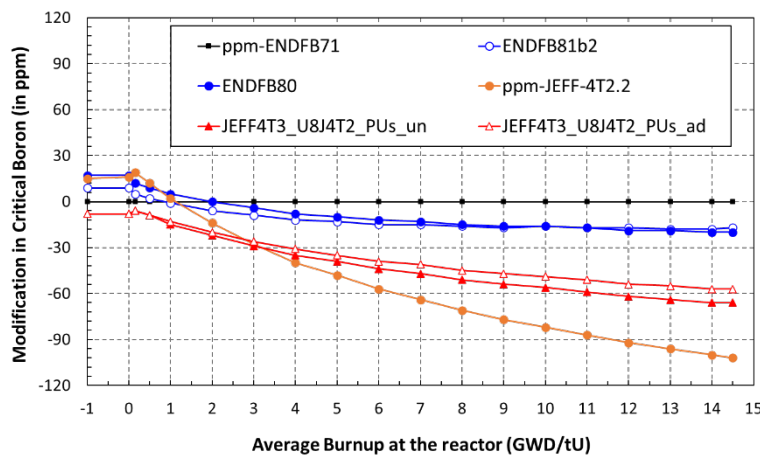


Figure 40. Critical boron modifications (in ppm) in NPP Almaraz II, cycle 1. Calculations performed with COBAYA/2D code.

It is worth to mention that the modification of reactivity along burnup can also be assessed at fuel-assembly level with less computational expensive calculations. Figure 41 and Figure 42 show the Δk_{eff} (in pcm) in a typical PWR Westinghouse 17x17 fuel assembly at 4.8 w/o as a function of burnup. ENDF/B-VII.1 is again taken as reference. As it can be seen in Figure 41, the performance of ENDF/B-VIII.1b2 is very close to ENDF/B-VIII.0, with an increase of reactivity of around 200 pcm at 60 GWD/tU. Figure 42 shows the change in reactivity isotope-by-isotope for ENDF/B-VIII.1b2. It can be seen the large increase of reactivity with the new ^{241}Pu evaluation (this isotope was not important in the loss-of-reactivity for ENDF/B-VIII.0).

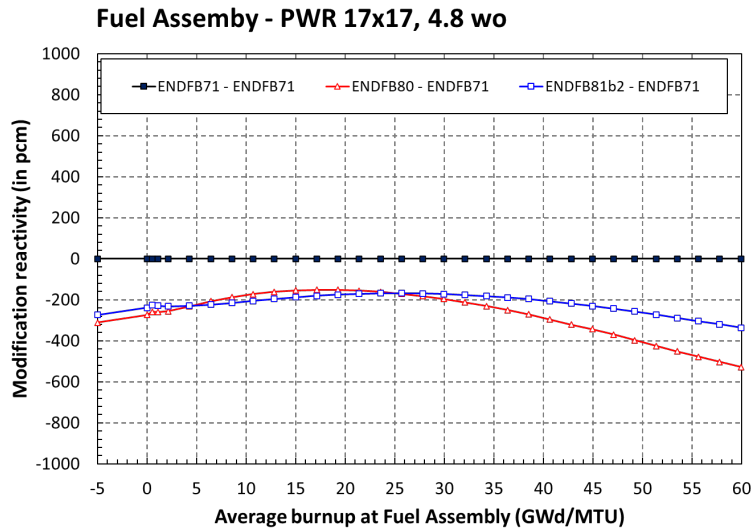


Figure 41. Modification reactivity (in pcm) in a typical PWR Fuel Assembly 17x17 at 4.8w/o. Calculations performed with WIMSD5b lattice code.

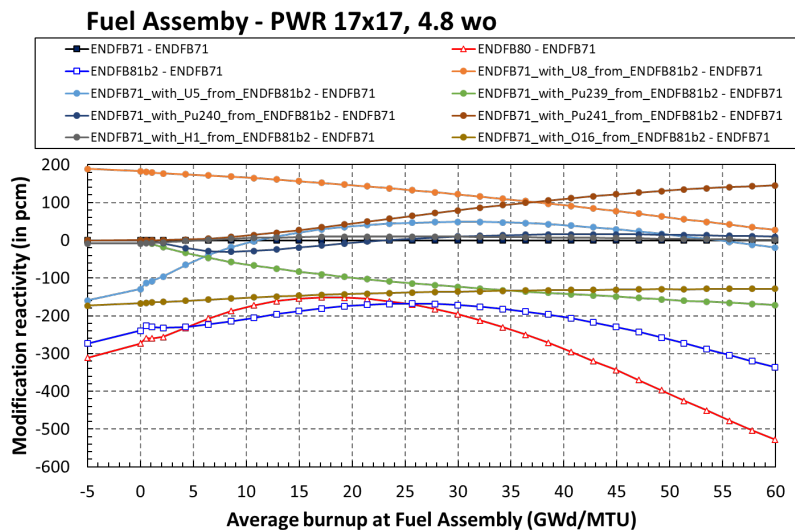


Figure 42. Modification reactivity (in pcm) in typical PWR Fuel Assembly 17x17 at 4.8w/o. Calculations performed with WIMSD5b lattice code.

5.2. Analysis of post-irradiation experiments (CEA/DES)

At CEA/DES, the overall performance of JEFF libraries has been assessed through the interpretation of Post-Irradiation Experiments (PIE) of reprocessed uranium pellets. Fuel pellets were irradiated in a 900 MWe PWR and chemically analysed for major and minor actinides. The specific experiment studied covers from 1 to 3 cycles of irradiation of PWR-UO₂ pins (4.5wt.% ²³⁵U enriched but using reprocessed uranium, *i.e.* with a given amount of ²³⁶U) as a function of burnup in the CRUAS reactor. A sketch of the radial and axial position of the examined rod cuts is illustrated in Figure 43 and Figure 44 respectively.

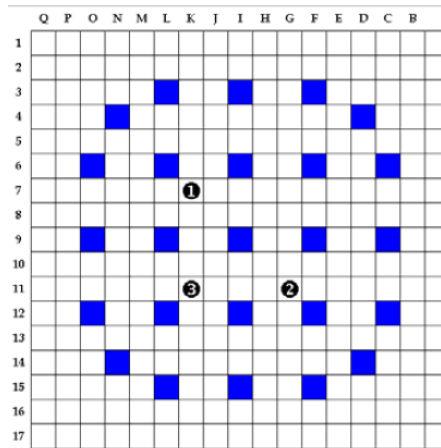


Figure 43. Sketch of the radial position of the analyzed fuel rods.

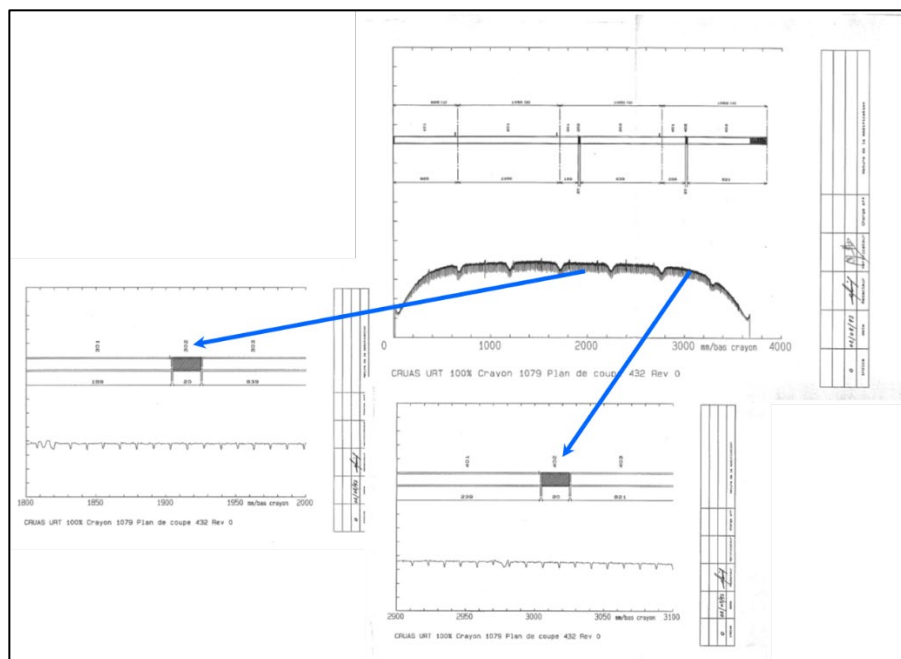


Figure 44. Sketch of the axial position of the analyzed rod cuts.

Calculation details are given as follows:

- SHEM-MOC calculation route:, 281 neutron kinetic energy-groups, P1-scattering, Method of Characteristics, B1-critical leakage,
- Cycle follow up (power + temperatures), 2 rod cuts (1900 & 3000mm heights) for each of the 3 cycles,
- $^{235,236,238}\text{U}$ and $^{239,240}\text{Pu}$ mutual shielding calculation during depletion,
- The fluence is scaled by using the “virtual neodymium indicator”, *i.e.*, by fixing the specific power [W/g_{HM}] in order to reach exactly (more than 0.1% accuracy) the experimental buildup estimated through this combination of neodymium amounts during the precise duration of the irradiation:

$$\left(\frac{[^{145}\text{Nd}] + [^{146}\text{Nd}]}{2} \right) + [^{148}\text{Nd}] + [^{150}\text{Nd}]$$

The sum in the first parenthesis allows us to be free from $^{145}\text{Nd}(n,\gamma)$ potential biases.

C/E biases in the fuel isotopic concentrations for the 3 consecutive cycles using different libraries were examined. Table 12 shows the 2 fuel pin-averaged deviations per cycle for actinides and neodymium isotopes when using JEFF-x libraries.

Table 23. Biases (C/E) of isotopic concentrations using JEFF-x libraries
(fluences are estimated by using each nuclear data library, i.e. respective to their own neodymium fission yields)

JEFF-3.1.1	Cycle 1	Cycle 2	Cycle 3
SHEM-MOC	(C/E-1) ± ΔE/E [%]	(C/E-1) ± ΔE/E [%]	(C/E-1) ± ΔE/E [%]
²³⁴ U/ ²³⁸ U	1.0 ± 0.3	1.3 ± 0.4	1.4 ± 0.5
²³⁵ U/ ²³⁸ U	0.3 ± 0.4	1.5 ± 0.7	1.9 ± 1.3
²³⁶ U/ ²³⁸ U	0.0 ± 0.2	0.5 ± 0.2	0.2 ± 0.2
²³⁷ Np/ ²³⁸ U	-7.3 ± 2.9	-3.0 ± 2.9	-1.6 ± 2.0
²³⁸ Pu/ ²³⁸ U	-5.5 ± 1.9	-4.0 ± 2.0	-3.3 ± 1.8
²³⁹ Pu/ ²³⁸ U	1.1 ± 0.7	1.1 ± 0.9	2.7 ± 1.2
²⁴⁰ Pu/ ²³⁸ U	-0.7 ± 1.2	0.9 ± 0.9	1.2 ± 0.7
²⁴¹ Pu/ ²³⁸ U	-2.3 ± 2.1	-1.6 ± 1.4	0.1 ± 2.0
²⁴² Pu/ ²³⁸ U	-2.3 ± 3.3	-1.1 ± 2.1	-0.3 ± 1.6
²⁴¹ Am/ ²³⁸ U	•	•	0.1 ± 3.2
^{242m} Am/ ²³⁸ U	•	•	6.8 ± 7.0
²⁴³ Am/ ²³⁸ U	•	•	-0.3 ± 4.1
²⁴³ Cm/ ²³⁸ U	•	•	-5.1 ± 15.0
²⁴⁴ Cm/ ²³⁸ U	•	•	0.4 ± 5.6
²⁴⁵ Cm/ ²³⁸ U	•	•	2.3 ± 7.5
²⁴⁶ Cm/ ²³⁸ U	•	•	-16.2 ± 8.2
²⁴⁷ Cm/ ²³⁸ U	•	•	0.1 ± 29.7
¹⁴³ Nd/ ²³⁸ U	-0.8 ± 0.6	-0.5 ± 0.6	-0.5 ± 0.5
¹⁴⁴ Nd/ ²³⁸ U	-1.3 ± 0.8	-1.5 ± 0.8	-1.7 ± 0.9
¹⁴⁵ Nd/ ²³⁸ U	0.0 ± 0.7	-0.1 ± 0.7	-0.4 ± 0.6
¹⁴⁶ Nd/ ²³⁸ U	-0.4 ± 0.8	-0.3 ± 0.8	-0.2 ± 0.8
¹⁴⁸ Nd/ ²³⁸ U	0.5 ± 0.8	0.6 ± 0.7	0.6 ± 0.8
¹⁵⁰ Nd/ ²³⁸ U	-0.4 ± 0.9	0.0 ± 0.8	0.0 ± 0.8
Σ ¹⁴³ Nd/ ²³⁸ U	0.0 ± 1.0	0.0 ± 1.0	0.0 ± 1.0
BU Cray. [GWj/t]	13.6	22.0	35.3

JEFF-3.2	Cycle 1	Cycle 2	Cycle 3
SHEM-MOC	(C/E-1) ± ΔE/E [%]	(C/E-1) ± ΔE/E [%]	(C/E-1) ± ΔE/E [%]
²³⁴ U/ ²³⁸ U	1.2 ± 0.3	1.6 ± 0.4	2.1 ± 0.5
²³⁵ U/ ²³⁸ U	0.5 ± 0.4	1.7 ± 0.7	2.4 ± 1.3
²³⁶ U/ ²³⁸ U	0.0 ± 0.2	0.4 ± 0.2	0.2 ± 0.2
²³⁷ Np/ ²³⁸ U	-6.8 ± 2.9	-2.5 ± 2.9	-1.1 ± 2.0
²³⁸ Pu/ ²³⁸ U	-5.0 ± 1.9	-3.4 ± 2.0	-2.6 ± 1.8
²³⁹ Pu/ ²³⁸ U	1.4 ± 0.7	1.6 ± 0.9	3.4 ± 1.2
²⁴⁰ Pu/ ²³⁸ U	-0.7 ± 1.2	1.0 ± 0.9	1.5 ± 0.7
²⁴¹ Pu/ ²³⁸ U	-2.3 ± 2.1	-1.6 ± 1.4	0.4 ± 2.0
²⁴² Pu/ ²³⁸ U	-2.5 ± 3.3	-1.4 ± 2.1	-0.5 ± 1.6
²⁴¹ Am/ ²³⁸ U	•	•	-0.7 ± 3.2
^{242m} Am/ ²³⁸ U	•	•	13.9 ± 7.0
²⁴³ Am/ ²³⁸ U	•	•	-0.6 ± 4.1
²⁴³ Cm/ ²³⁸ U	•	•	23.6 ± 15.0
²⁴⁴ Cm/ ²³⁸ U	•	•	-0.6 ± 5.6
²⁴⁵ Cm/ ²³⁸ U	•	•	10.7 ± 7.5
²⁴⁶ Cm/ ²³⁸ U	•	•	-14.7 ± 8.2
²⁴⁷ Cm/ ²³⁸ U	•	•	-4.5 ± 29.7
¹⁴³ Nd/ ²³⁸ U	-0.8 ± 0.6	-0.5 ± 0.6	-0.3 ± 0.5
¹⁴⁴ Nd/ ²³⁸ U	-1.4 ± 0.8	-1.7 ± 0.8	-1.8 ± 0.9
¹⁴⁵ Nd/ ²³⁸ U	0.0 ± 0.7	-0.1 ± 0.7	-0.4 ± 0.6
¹⁴⁶ Nd/ ²³⁸ U	-0.4 ± 0.8	-0.4 ± 0.8	-0.2 ± 0.8
¹⁴⁸ Nd/ ²³⁸ U	0.5 ± 0.8	0.5 ± 0.7	0.5 ± 0.8
¹⁵⁰ Nd/ ²³⁸ U	-0.3 ± 0.9	0.0 ± 0.8	0.1 ± 0.8
Σ ¹⁴³ Nd/ ²³⁸ U	0.0 ± 1.0	0.0 ± 1.0	0.0 ± 1.0
BU Cray. [GWj/t]	13.5	21.9	35.2

JEFF-3.3	Cycle 1	Cycle 2	Cycle 3
SHEM-MOC	(C/E-1) ± ΔE/E [%]	(C/E-1) ± ΔE/E [%]	(C/E-1) ± ΔE/E [%]
²³⁴ U/ ²³⁸ U	1.2 ± 0.3	1.7 ± 0.4	2.1 ± 0.5
²³⁵ U/ ²³⁸ U	0.1 ± 0.4	0.9 ± 0.7	0.4 ± 1.3
²³⁶ U/ ²³⁸ U	0.1 ± 0.2	0.5 ± 0.2	0.3 ± 0.2
²³⁷ Np/ ²³⁸ U	-7.1 ± 2.9	-2.5 ± 2.9	-0.6 ± 2.0
²³⁸ Pu/ ²³⁸ U	-4.9 ± 1.9	-1.3 ± 2.0	2.8 ± 1.8
²³⁹ Pu/ ²³⁸ U	0.1 ± 0.7	0.1 ± 0.9	1.3 ± 1.2
²⁴⁰ Pu/ ²³⁸ U	-1.4 ± 1.2	0.7 ± 0.9	1.5 ± 0.7
²⁴¹ Pu/ ²³⁸ U	-3.3 ± 2.1	-2.2 ± 1.4	0.0 ± 2.0
²⁴² Pu/ ²³⁸ U	-4.6 ± 3.3	-2.7 ± 2.1	-0.8 ± 1.6
²⁴¹ Am/ ²³⁸ U	•	•	-1.1 ± 3.2
^{242m} Am/ ²³⁸ U	•	•	12.5 ± 7.0
²⁴³ Am/ ²³⁸ U	•	•	-4.5 ± 4.1
²⁴³ Cm/ ²³⁸ U	•	•	22.2 ± 15.0
²⁴⁴ Cm/ ²³⁸ U	•	•	8.3 ± 5.6
²⁴⁵ Cm/ ²³⁸ U	•	•	20.3 ± 7.5
²⁴⁶ Cm/ ²³⁸ U	•	•	-6.7 ± 8.2
²⁴⁷ Cm/ ²³⁸ U	•	•	4.3 ± 29.7
¹⁴³ Nd/ ²³⁸ U	-0.7 ± 0.6	-0.4 ± 0.6	-0.1 ± 0.5
¹⁴⁴ Nd/ ²³⁸ U	-1.9 ± 0.8	-2.4 ± 0.8	-2.7 ± 0.9
¹⁴⁵ Nd/ ²³⁸ U	-0.3 ± 0.7	-0.5 ± 0.7	-1.1 ± 0.6
¹⁴⁶ Nd/ ²³⁸ U	-0.1 ± 0.8	0.0 ± 0.8	0.4 ± 0.8
¹⁴⁸ Nd/ ²³⁸ U	0.8 ± 0.8	0.8 ± 0.7	1.0 ± 0.8
¹⁵⁰ Nd/ ²³⁸ U	-0.8 ± 0.9	-0.6 ± 0.8	-0.6 ± 0.8
Σ ¹⁴³ Nd/ ²³⁸ U	0.0 ± 1.0	0.0 ± 1.0	0.0 ± 1.0
BU Cray. [GWj/t]	13.5	21.8	35.0

JEFF-4.0i0	Cycle 1	Cycle 2	Cycle 3
SHEM-MOC	(C/E-1) ± ΔE/E [%]	(C/E-1) ± ΔE/E [%]	(C/E-1) ± ΔE/E [%]
²³⁴ U/ ²³⁸ U	1.2 ± 0.3	1.6 ± 0.4	1.9 ± 0.5
²³⁵ U/ ²³⁸ U	0.1 ± 0.4	0.8 ± 0.7	0.2 ± 1.3
²³⁶ U/ ²³⁸ U	0.0 ± 0.2	0.5 ± 0.2	0.2 ± 0.2
²³⁷ Np/ ²³⁸ U	-7.2 ± 2.9	-2.6 ± 2.9	-0.8 ± 2.0
²³⁸ Pu/ ²³⁸ U	-7.2 ± 1.9	-5.0 ± 2.0	-3.8 ± 1.8
²³⁹ Pu/ ²³⁸ U	0.4 ± 0.7	0.6 ± 0.9	2.2 ± 1.2
²⁴⁰ Pu/ ²³⁸ U	-2.9 ± 1.2	-1.0 ± 0.9	-0.4 ± 0.7
²⁴¹ Pu/ ²³⁸ U	-3.4 ± 2.1	-2.1 ± 1.4	0.1 ± 2.0
²⁴² Pu/ ²³⁸ U	-5.2 ± 3.3	-3.3 ± 2.1	-1.8 ± 1.6
²⁴¹ Am/ ²³⁸ U	•	•	-0.9 ± 3.2
^{242m} Am/ ²³⁸ U	•	•	13.0 ± 7.0
²⁴³ Am/ ²³⁸ U	•	•	-1.7 ± 4.1
²⁴³ Cm/ ²³⁸ U	•	•	21.8 ± 15.0
²⁴⁴ Cm/ ²³⁸ U	•	•	11.7 ± 5.6
²⁴⁵ Cm/ ²³⁸ U	•	•	24.3 ± 7.5
²⁴⁶ Cm/ ²³⁸ U	•	•	-3.6 ± 8.2
²⁴⁷ Cm/ ²³⁸ U	•	•	8.0 ± 29.7
¹⁴³ Nd/ ²³⁸ U	-0.6 ± 0.6	-0.1 ± 0.6	0.1 ± 0.5
¹⁴⁴ Nd/ ²³⁸ U	-1.7 ± 0.8	-2.0 ± 0.8	-2.4 ± 0.9
¹⁴⁵ Nd/ ²³⁸ U	0.1 ± 0.7	0.0 ± 0.7	-0.3 ± 0.6
¹⁴⁶ Nd/ ²³⁸ U	-0.3 ± 0.8	-0.3 ± 0.8	-0.2 ± 0.8
¹⁴⁸ Nd/ ²³⁸ U	0.5 ± 0.8	0.5 ± 0.7	0.5 ± 0.8
¹⁵⁰ Nd/ ²³⁸ U	-0.6 ± 0.9	-0.3 ± 0.8	-0.2 ± 0.8
Σ ¹⁴³ Nd/ ²³⁸ U	0.0 ± 1.0	0.0 ± 1.0	0.0 ± 1.0
BU Cray. [GWj/t]	13.5	21.9	35.1

JEFF-4.0t1	Cycle 1	Cycle 2	Cycle 3
SHEM-MOC	(C/E-1) ± ΔE/E [%]	(C/E-1) ± ΔE/E [%]	(C/E-1) ± ΔE/E [%]
²³⁴ U/ ²³⁸ U	1.2 ± 0.3	1.6 ± 0.4	1.8 ± 0.5
²³⁵ U/ ²³⁸ U	-0.1 ± 0.4	0.5 ± 0.7	-0.4 ± 1.3
²³⁶ U/ ²³⁸ U	-0.1 ± 0.2	0.3 ± 0.2	-0.1 ± 0.2
²³⁷ Np/ ²³⁸ U	-3.6 ± 2.9	1.0 ± 2.9	2.7 ± 2.0
²³⁸ Pu/ ²³⁸ U	-2.4 ± 1.9	-0.5 ± 2.0	0.8 ± 1.8
²³⁹ Pu/ ²³⁸ U	0.9 ± 0.7	1.3 ± 0.9	3.1 ± 1.2
²⁴⁰ Pu/ ²³⁸ U	-4.8 ± 1.2	-2.6 ± 0.9	-1.6 ± 0.7
²⁴¹ Pu/ ²³⁸ U	-3.7 ± 2.1	-2.5 ± 1.4	-0.2 ± 2.0
²⁴² Pu/ ²³⁸ U	-6.0 ± 3.3	-4.1 ± 2.1	-2.3 ± 1.6
²⁴¹ Am/ ²³⁸ U	•	•	-1.1 ± 3.2
^{242m} Am/ ²³⁸ U	•	•	12.2 ± 7.0
²⁴³ Am/ ²³⁸ U	•	•	-1.3 ± 4.1
²⁴³ Cm/ ²³⁸ U	•	•	21.4 ± 15.0
²⁴⁴ Cm/ ²³⁸ U	•	•	3.8 ± 5.6
²⁴⁵ Cm/ ²³⁸ U	•	•	15.0 ± 7.5
²⁴⁶ Cm/ ²³⁸ U	•	•	-9.8 ± 8.2
²⁴⁷ Cm/ ²³⁸ U	•	•	1.3 ± 29.7
¹⁴³ Nd/ ²³⁸ U	-0.6 ± 0.6	-0.2 ± 0.6	0.0 ± 0.5
¹⁴⁴ Nd/ ²³⁸ U	-1.6 ± 0.8	-2.0 ± 0.8	-2.3 ± 0.9
¹⁴⁵ Nd/ ²³⁸ U	0.1 ± 0.7	0.0 ± 0.7	-0.3 ± 0.6
¹⁴⁶ Nd/ ²³⁸ U	-0.3 ± 0.8	-0.3 ± 0.8	-0.1 ± 0.8
¹⁴⁸ Nd/ ²³⁸ U	0.5 ± 0.8	0.5 ± 0.7	0.5 ± 0.8
¹⁵⁰ Nd/ ²³⁸ U	-0.7 ± 0.9	-0.4 ± 0.8	-0.3 ± 0.8
Σ ¹⁴³ Nd/ ²³⁸ U	0.0 ± 1.0	0.0 ± 1.0	0.0 ± 1.0
BU Cray. [GWj/t]	13.5	21.9	35.1

JEFF-4.0T3	Cycle 1	Cycle 2	Cycle 3
SHEM-MOC	(C/E-1) ± ΔE/E [%]	(C/E-1) ± ΔE/E [%]	(C/E-1) ± ΔE/E [%]
²³⁴ U/ ²³⁸ U	1.2 ± 0.3	1.8 ± 0.4	2.4 ± 0.5
²³⁵ U/ ²³⁸ U	0.5 ± 0.4	1.9 ± 0.7	2.8 ± 1.3
²³⁶ U/ ²³⁸ U	0.0 ± 0.2	0.4 ± 0.2	0.2 ± 0.2
²³⁷ Np/ ²³⁸ U	-4.1 ± 2.9	0.2 ± 2.9	1.7 ± 2.0
²³⁸ Pu/ ²³⁸ U	-3.2 ± 1.9	-2.0 ± 2.0	-1.4 ± 1.8
²³⁹ Pu/ ²³⁸ U	1.4 ± 0.7	1.6 ± 0.9	3.7 ± 1.2
²⁴⁰ Pu/ ²³⁸ U	-4.8 ± 1.2	-2.9 ± 0.9	-2.1 ± 0.7
²⁴¹ Pu/ ²³⁸ U	-4.1 ± 2.1	-4.2 ± 1.4	-2.5 ± 2.0
²⁴² Pu/ ²³⁸ U	-5.8 ± 3.3	-5.3 ± 2.1	-4.9 ± 1.6
²⁴¹ Am/ ²³⁸ U	•	•	-3.2 ± 3.2
^{242m} Am/ ²³⁸ U	•	•	9.3 ± 7.0
²⁴³ Am/ ²³⁸ U	•	•	-4.5 ± 4.1
²⁴³ Cm/ ²³⁸ U	•	•	17.2 ± 15.0
²⁴⁴ Cm/ ²³⁸ U	•	•	-0.4 ± 5.6
²⁴⁵ Cm/ ²³⁸ U	•	•	9.8 ± 7.5
²⁴⁶ Cm/ ²³⁸ U	•	•	-15.5 ± 8.2
²⁴⁷ Cm/ ²³⁸ U	•	•	-6.0 ± 29.7
¹⁴³ Nd/ ²³⁸ U	-1.4 ± 0.6	-1.1 ± 0.6	-0.6 ± 0.5
¹⁴⁴ Nd/ ²³⁸ U	-1.6 ± 0.8	-2.3 ± 0.8	-2.9 ± 0.9
¹⁴⁵ Nd/ ²³⁸ U	1.2 ± 0.7	1.1 ± 0.7	0.8 ± 0.6
¹⁴⁶ Nd/ ²³⁸ U	-0.6 ± 0.8	-0.7 ± 0.8	-0.5 ± 0.8
¹⁴⁸ Nd/ ²³⁸ U	-0.7 ± 0.8	-0.6 ± 0.7	-0.3 ± 0.8
¹⁵⁰ Nd/ ²³⁸ U	0.0 ± 0.9	0.2 ± 0.8	0.2 ± 0.8
Σ ¹⁴³ Nd/ ²³⁸ U	0.0 ± 1.0	0.0 ± 1.0	0.0 ± 1.0
BU rod [GWd/t _{HM}]	13.4	21.7	34.8

While C/E results are consistent with experimental uncertainties, different trends with burnup can be observed. A perturbation analysis aimed at offering insights into the performance of libraries for the isotopic prediction in LWR applications was then carried out.

APOLLO2 perturbation analysis of post-irradiated examination results obtained for PWR-UO₂ pins at different burnup (22 and 35 GWD/MTU) were performed. **JEFF-4T3 analysis results suggest that some cross sections should still be revised:**

- ***JEFF-4T3/²³⁹Pu($n_{[0.10-0.53]eV}, \gamma$) should be increased by (+5.3±1.4)% (prior uncertainty was ±3%).***
- ***JEFF-4T3/²⁴⁰Pu($n_{[0.53-4.00]eV}, \gamma$) should be increased by (+1.5±2.2)% (prior uncertainty was ±3%).***

6. Shielding benchmarks *C/E* validation and nuclear data trends (JSI/UKAEA, UPM)

Different shielding integral benchmarks from SINBAD [SINBAD, 2021] database have been extensively analysed to provide feedback on nuclear data validation. The use of SINBAD for data validation is nowadays less widespread compared to the use of ICSBEP or IRPhEP [Kodeli, 2021]. However, shielding benchmarks may offer additional insights beyond the neutron energy of criticality benchmarks [Astigarraga, 2022] [Cabellos, 2023].

Shielding and transmission benchmarks exhibit high sensitivity to neutron leakage, which may lead to further shortcomings if deficiencies in angular distributions are compensated in the integral-energy cross-sections. They can be especially useful for focusing on specific nuclear data, such as scattering (elastic, inelastic) and fission observables (fission, nubar and PNFS).

JSI/UKAEA has studied different shielding benchmarks, mainly for validation of iron evaluations, providing valuable indications on iron cross section data.

UPM has contributed to this task with the assessment of different Time-of-Flight (ToF) integral benchmarks (Oktavian and FNS) as well as neutron transmission experiments from ICSBEP.

6.1. Shielding benchmarks for validation of iron evaluations (JSI/UKAEA)

Table 24 summarizes the SINBAD benchmarks analyzed by JSI/UKAEA for validation of iron evaluations.

Table 24. Summary of analyzed SINBAD benchmarks for validation of iron evaluations.

Benchmark / quality	Additional information needed on:
ASPIS Iron-88 ~ ◆◆◆ Analyses by JSI & UKAEA	Review: new MCNP model. Additional information needed on: <ul style="list-style-type: none"> - detectors arrangement (e.g. stacking) - gaps between the slabs - absolute calibration of neutron source & dilution factor - effect of the cave walls
ORNL PCA Pool Critical Assembly - PV Benchmark (1980) Analyses by NRG (S.v.d. Marck)	<ul style="list-style-type: none"> - approximate modelling of neutron source (material test reactor MTR) with a 93% ²³⁵U fuel elements) - SINBAD quality evaluations to be performed
ASPIS PCA REPLICA - Winfrith Water/Steel ◆◆◆ Analyses by JSI & UKAEA	Supplementary information received from David Hanlon (Jacobs) on (available from WPEC SG47 Github [WPEC-SG47-2022]): <ul style="list-style-type: none"> - geometrical arrangement of the fission plate and ASPIS cave; - geometry and material of the detectors; - measurement arrangement and background contribution - availability of ²³⁵U fission chamber measurements
CIAE Iron slab 14 MeV benchmark Analyses by JSI & UKAEA	<ul style="list-style-type: none"> - Ongoing SINBAD evaluation (presented at WPEC SG47 [WPEC-SG47-2022]) - TOA neutron spectra measured from 5, 10 and 15 cm Fe slabs at 600 and 1200 (~2016)
KFK Iron spheres neutron and gamma spectra Analyses by JSI & UKAEA	<ul style="list-style-type: none"> - Ongoing SINBAD evaluation (presented at WPEC SG47) - Neutron and gamma spectra measured from Fe spheres with diameters of 25, 30 and 35 cm (gammas) and 25, 30, 35 and 40 cm (neutrons) (~1977)

The ASPIS Iron-88 benchmark consists of a 67-cm thick iron block irradiated with ²³⁵U fission neutrons. Several reaction rates were calculated using the MCNP5 code and compared to measurements: ²⁷Al(n,a) and ³²S(n,p) using older and the most recent evaluations JEFF-3.3/4T, ENDF/B-VI to VIII.0, JENDL-4/-5 and FENDL-3.2. Figure 45 and Figure 46 show *C/E* ratios. Dashed lines delimit the $\pm 1\sigma$ standard deviations of the measurements. Uncertainties due to nuclear data uncertainties are also

shown for a few detector positions. Worse C/E agreement using JEFF-3.3 and ENDF/B-VIII.0 comparing to older iron evaluations can be observed.

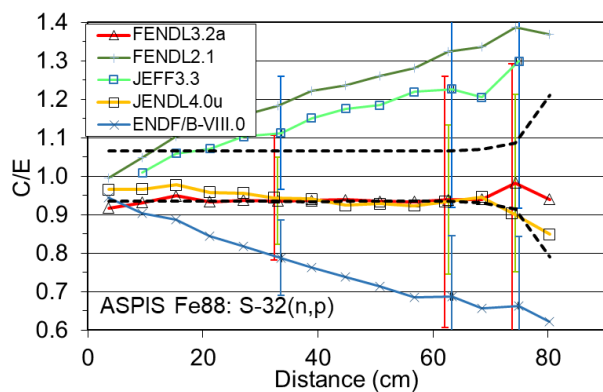


Figure 45. Biases C/E in $S(n,p)$ for ASPIS Fe-88.

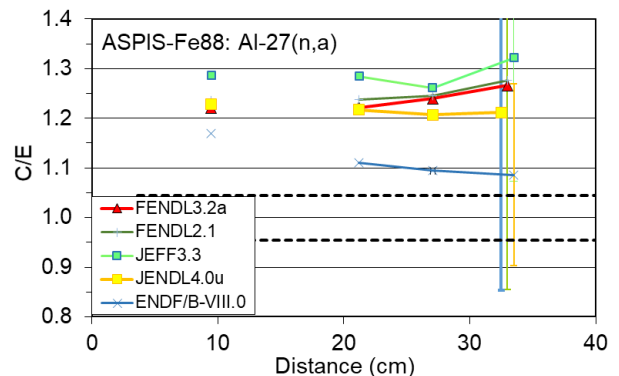


Figure 46. Biases C/E in $Al(n,\alpha)$ for ASPIS Fe-88.

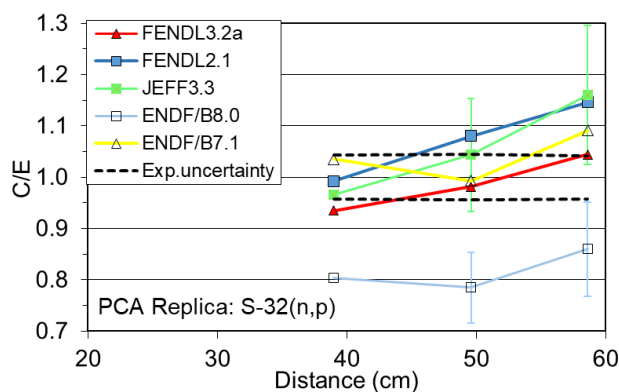


Figure 47. Biases C/E in $S(n,p)$ for PCA Replica.

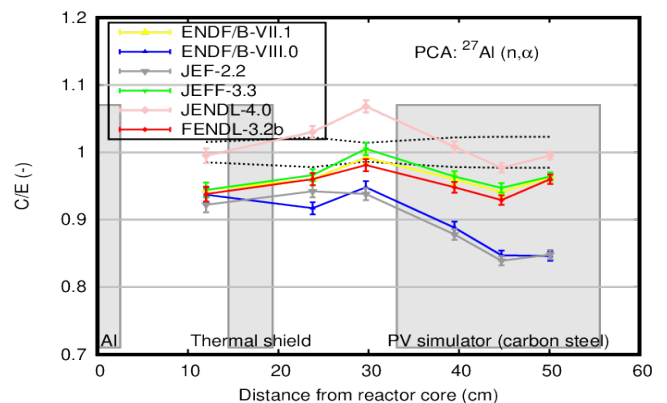


Figure 48. Biases C/E in $Al(n,\alpha)$ for PCA.

PCA and PCA Replica was then added to the Verification & Validation scheme to check ASPIS Iron-88 results [Kodeli, 2023b]. C/E values for the reactions $^{32}\text{S}(n,p)$ and $^{27}\text{Al}(n,\alpha)$ using PCA Replica and PCA respectively are shown in Figure 47 and Figure 48. Consistency between both experiments was verified, that is, predictions provided by both experiments concerning nuclear data quality are consistent, except for the $^{27}\text{Al}(n,\alpha)$ reaction rates. Such reaction rates are severely overestimated using all libraries for ASPIS Iron-88 benchmark but in a good agreement, or even underestimated, for PCA benchmark. This may be due to some systematic uncertainties involved in the ASPIS-Iron88 measurements.

C/E values for the ASPIS-Iron88 benchmark obtained using the recent FENDL-3.2, JENDL-5, INDEN libraries and the ongoing JEFF4T nuclear data evaluations are presented in Figure 49, demonstrating considerable improvements at all energies.

Sensitivity profiles to $^{56}\text{Fe}(n,n')$ in deepest positions for PCA, PCA Replica and ASPIS-Iron88 were computed and are shown in Figure 50 to Figure 52.

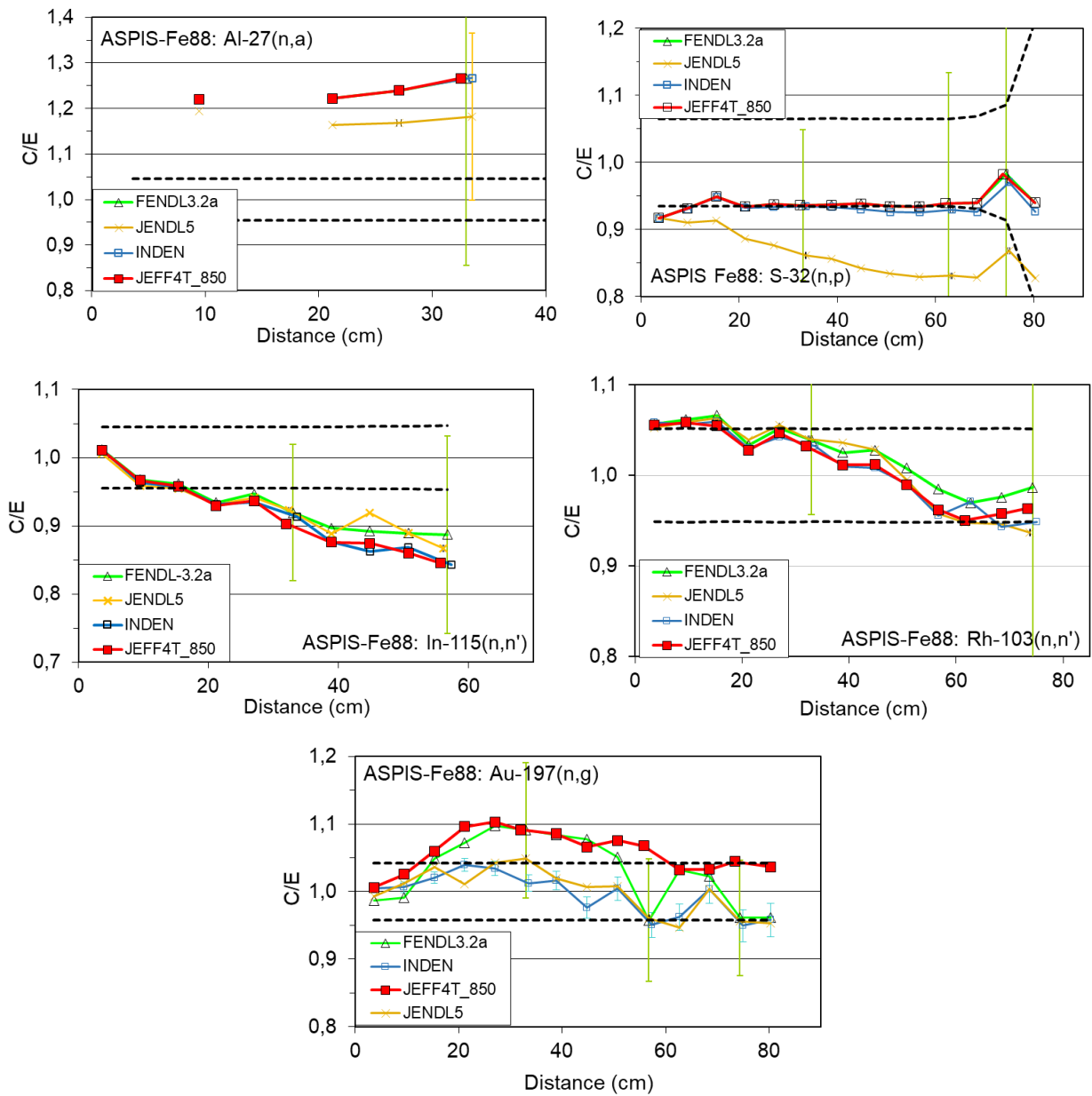


Figure 49. Biases C/E for reaction rates measured in ASPIS Fe-88 benchmark obtained using recent nuclear data.

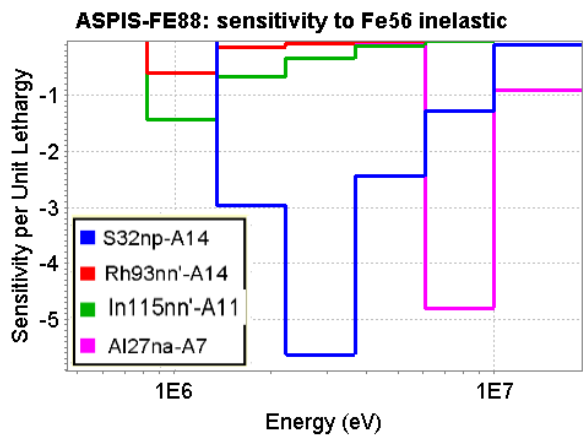


Figure 50. Sensitivities for ASPIS Fe-88.

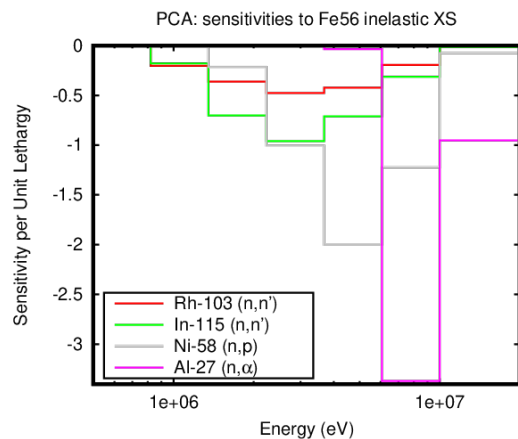


Figure 51. Sensitivities for PCA.

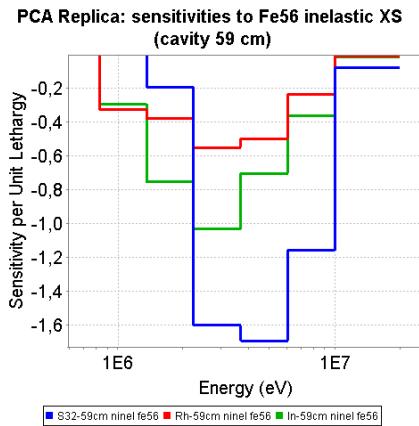


Figure 52. Sensitivities for PCA Replica.

Table 25. Computational nuclear data uncertainties vs. measurement uncertainties for ASPIS-*Iron88*.

ASPIS Fe88	ΔE	Uncertainties (%)		
		ΔC		
		JEFF-3.3	ENDF/B-VII.1	JENDL-4.0
$^{197}\text{Au}(n,g)$: 26cm	4.2	5.1	9.9	9.2
	4.2	4.3	8.8	8.8
	4.2	3.7	8.1	8.5
$^{103}\text{Rh}(n,n')$: 26cm	5.1	6.4	7.8	8.6
	5.1	11.7	18.7	14.9
$^{115}\text{In}(n,n')$: 26cm	4.5	6.6	10.5	14.8
	4.7	10.5	15.0	17.8
$^{32}\text{S}(n,p)$: 26cm	6.5	13.3	11.5	17.2
	6.5	25.0	20.8	35.0
	8.6	29.3	25.1	42.9
$^{27}\text{Al}(n,a)$: 26cm	4.7	18.8	31.5	29.5

Table 26. Computational nuclear data uncertainties vs. measurement uncertainties for PCA Replica.

PCA REPLICA		Uncertainty (%)		
		ΔE	ΔC	
			JEFF-3.3	ENDF/B-VIII.0
$^{103}\text{Rh}(n,n')$	59cm	5.0	8.0	8.0
$^{115}\text{In}(n,n')$:	26cm	4.4	9.7	9.0
$^{32}\text{S}(n,p)$:	49cm	5.7	10.6	9.9
	59cm	5.5	11.6	11.8

6.2. KFK γ -ray leakage benchmark (JSI/UKAEA)

New SINBAD evaluation by Stanislav Simakov: KFK-1977 measured gamma from bare $^{252}\text{Cf}(s.f.)$ source and from $\varnothing 25$, 30 and 35 cm Fe spheres was prepared within WPEC SG47 [WPEC-SG47, 2022], including detailed descriptions of facility, methods and final numerical results with uncertainties. This evaluation complements the existing KFK Iron sphere SINBAD evaluation which is limited to the neutron leakage spectra leaking from the 15, 20, 25, 30, 35, and 40 cm diameter iron spheres.

Neutron and gamma transport and sensitivity/uncertainty calculations were performed using the MCNP5, PARTISN and SUSD-3D computer codes and FENDL-3.2a nuclear data libraries. As shown in Figure 54, an excellent agreement between the MCNP Monte Carlo and PARTISN deterministic solutions was observed, and a reasonable agreement with the measured neutron and gamma spectra.

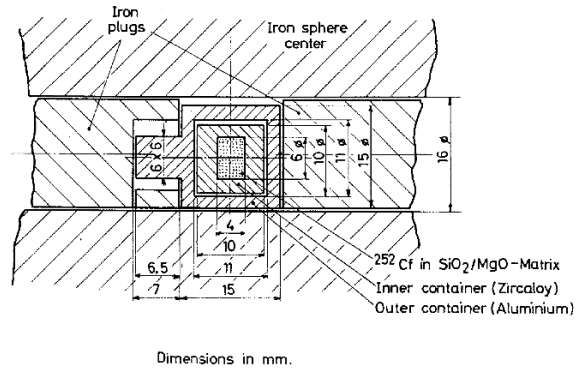
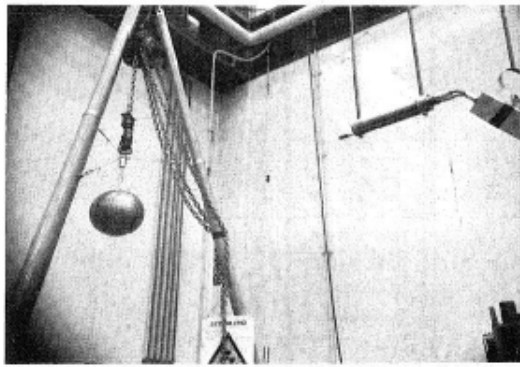


Figure 53. KFK set-up and ^{252}Cf source.

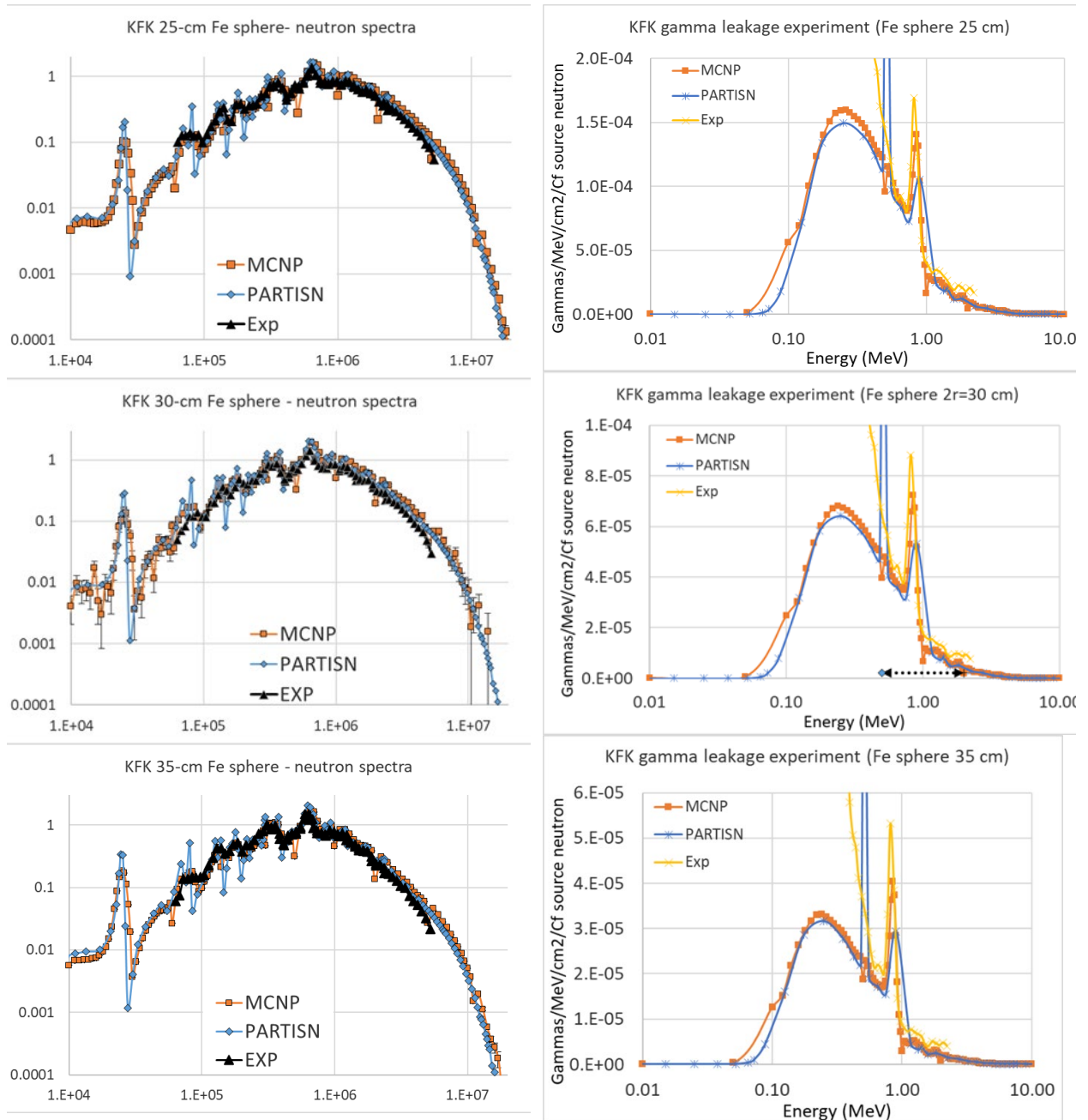


Figure 54. Comparison between the measured neutron and gamma spectra from KFK iron spheres of different diameters and those calculated using the MCNP and PARTISN codes and FENDL-3.2a nuclear data. Note that electrons were not transported in MCNP.

The SUSD3D [Kodeli, 2022] code was recently extended to the gamma ray nuclear data sensitivity/uncertainty calculations. Sensitivities of the total gamma flux to iron elastic and inelastic neutron, and the incoherent gamma scattering data are presented in Figure 55. Due to the lack of the covariance data for the photon nuclear data the full uncertainty calculations could not be performed yet. Only the partial uncertainties due to the uncertainty in the neutron and gamma fission spectra could be estimated in amount to roughly ~10% (see Table 27 and Table 28 for details on the different terms contributing to the uncertainty) [Kodeli, 2023a].

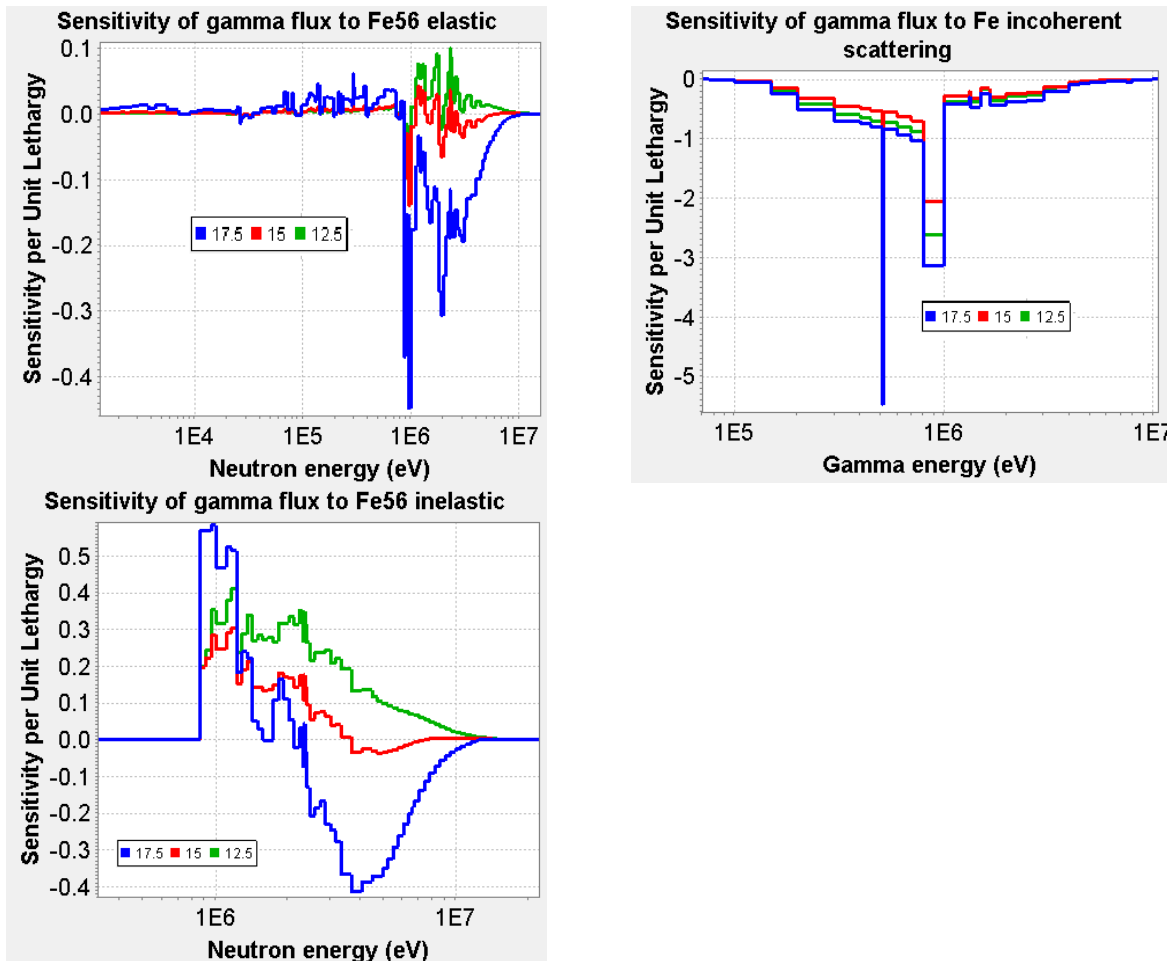


Figure 55. KFK set-up: Sensitivity of the total gamma flux to the ^{56}Fe elastic and inelastic neutron cross sections and to the incoherent gamma scattering data for iron spheres with the radius of 12.5, 15, and 17.5 cm.

Table 27. KFK benchmark: contribution of neutron-induced gammas and ^{252}Cf gamma source terms to the 0.5 - 2 MeV gamma flux in the detector for the spheres of different radii.

γ (0.5 - 2 MeV)	^{252}Cf neutron			^{252}Cf gammas		
	Sphere radius (cm)	Total	Prompt	Delayed	Total	Prompt
12.5	50.94%	50.93%	0.01%	49.06%	23.44%	25.63%
15	63.54%	63.53%	0.01%	36.46%	17.56%	18.12%
17.5	82.72%	82.70%	0.02%	17.28%	10.10%	7.18%

Table 28. Uncertainty in the 0.5 to 2 MeV gamma flux due to the uncertainty in ^{252}Cf PFNS and prompt and delayed gamma source spectra.

γ (0.5 - 2 MeV) Sphere radius (cm)	^{252}Cf neutron	^{252}Cf gammas	
	Prompt	Prompt	Delayed
12.5	6.6%	6.1%	4.5%
15	8.0%	5.0%	3.3%
17.5	9.5%	2.7%	1.4%

6.3. Shielding Time-of-Flight benchmarks in SINBAD: Oktavian and FNS (UPM)

UPM has actively participated in the Working Party on International Nuclear Data Evaluation Cooperation Subgroup 47 (WPEC/SG47) entitled "Use of Shielding Integral Benchmark Archive and Database for Nuclear Data Validation" [WPEC/SG47, 2019]. One of the Tasks where UPM was involved is the compilation of inputs for various transport codes and shielding benchmark data to be shared via the NEA GitLab.

Figure 56 shows a screenshot of the benchmark repository used in the WPEC/SG47 for nuclear data validation. UPM has delivered the so-called "UPM Suite" [Plompen, 2020], with a set of MCNP inputs and MCNP results for the shielding Time-of-Flight (ToF) OKTAVIAN and FNS Benchmarks.

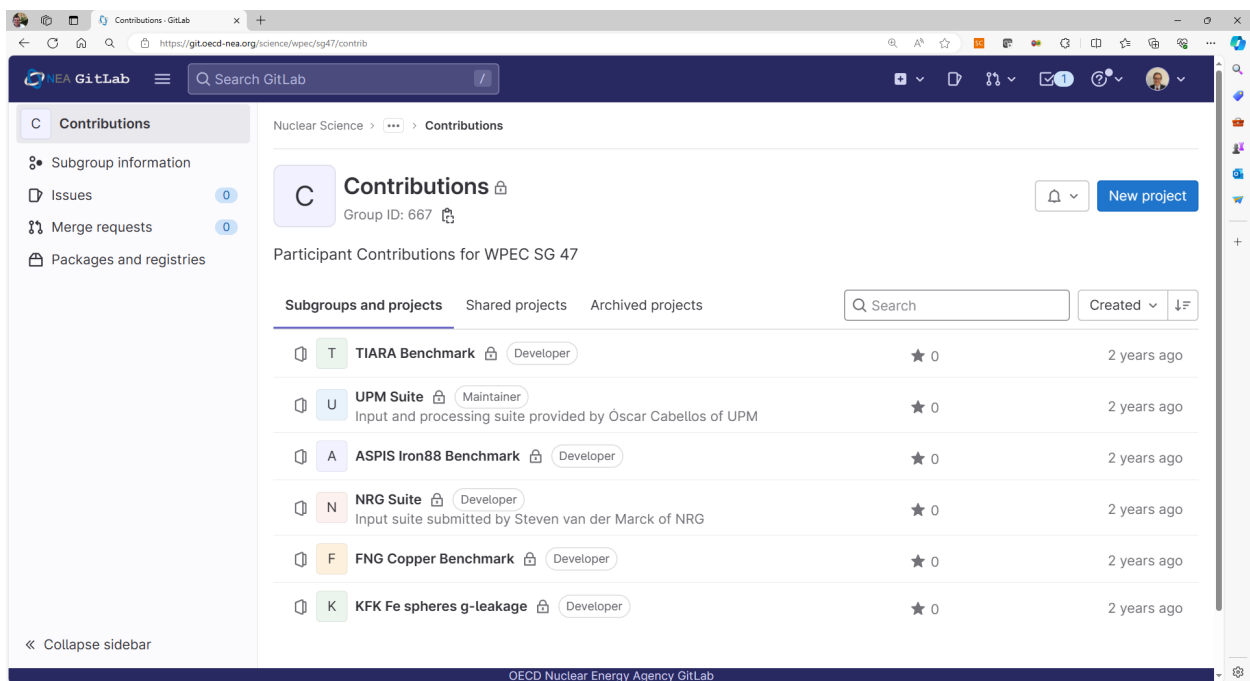


Figure 56. Screen-shot SG47 GitLab³ showing UPM Suite of OKTAVIAN and FNS Benchmarks.

³ <https://git.oecd-nea.org/science/wpec/sg47/contrib>

6.3.1. FNS/TOF

The first time-of-flight (TOF) shielding and transmission experiments selected is the JAEA Fusion Neutron Source (FNS). The FNS/TOF used a 14-MeV dT neutron source [Maekawa, 2000] [Maekawa, 2002].

Figure 57 shows the experimental setup for FNS/TOF. The detector was located to observe leakage neutrons from cylindrical slabs at several angles.

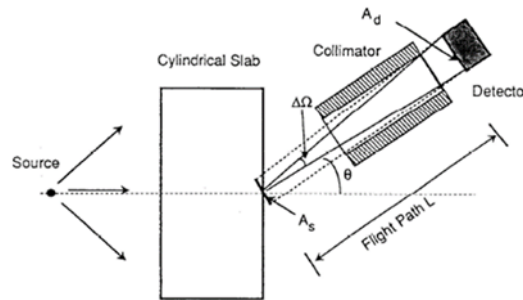


Figure 57. FNS/TOF setup

A list of FNS Benchmarks included in the UPM distribution used to test different nuclear data libraries can be seen in Table 29. These benchmarks are classified by materials, geometry and angle-dependent detector positions.

Table 29. FNS-ToF Benchmarks (17 cases x 5 angles)

NOTE: Ref. F. Maekawa et al., "Collection of Experimental Data for Fusion Neutronics Benchmark", JAERI, 1994.

Geometry, materials		Detector Position
Beryllium	FNS-TOF/31.4 CM(R)*15.24 CM(Z)	Angle= 0.0°
	FNS-TOF/31.4 CM(R)*5.06 CM(Z)	Angle= 12.20 °
Graphite	FNS-TOF/31.4 CM(R)*20.24CM(Z)	Angle= 24.90 °
	FNS-TOF/31.4 CM(R)*40.48CM(Z)	Angle= 41.80 °
	FNS-TOF/31.4 CM(R)*5.06CM(Z)	Angle= 66.80 °
Iron	FNS-TOF/50.0 CM(R)*20.0 CM(Z)-Iron	
	FNS-TOF/50.0 CM(R)*40.0 CM(Z)-Iron	
	FNS-TOF/50.0 CM(R)*5.0 CM(Z)-Iron	
	FNS-TOF/50.0 CM(R)*60.0 CM(Z)-Iron	
Li2O	FNS-TOF/31.4 CM(R)*20.0 CM(Z)-Li2O	
	FNS-TOF/31.4 CM(R)*40.0 CM(Z)-Li2O	
	FNS-TOF/31.4 CM(R)*4.8 CM(Z)-Li2O	
N2	FNS-TOF/ N2 SLAB-TOF	
O2	FNS-TOF/ LO2 SLAB-TOF	
Lead	FNS-TOF/31.4 CM(R)*20.32CM(Z)-Lead	
	FNS-TOF/31.4 CM(R)*40.64CM(Z)-Lead	
	FNS-TOF/31.4 CM(R)*5.06CM(Z)-Lead	

Figure 58 to Figure 91 show results obtained for different ToF-experiment at FNS showing angular neutron leakage spectra for thick slabs at 0° degrees for different nuclear data evaluations. Here the performance of JEFF-3.3, FENDL-3.1b and ENDF/B-VIII.0 is compared, jointly with different beta releases for ENDF/B-VIII.1 and JEFF-4.0, with the experimental data.

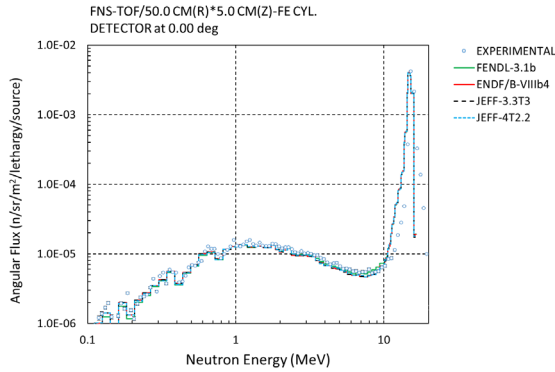


Figure 58. Angular neutron leakage spectra at 0 degrees for the 5CM(Z) FNS-TOF iron FNS-TOF experiment: JEFF-4T2.

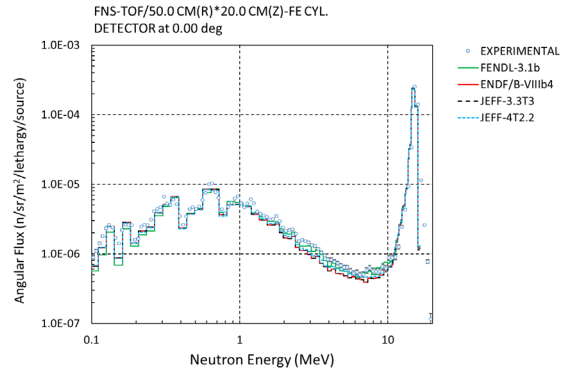


Figure 59. Angular neutron leakage spectra at 0 degrees for the 20CM(Z) FNS-TOF iron FNS-TOF experiment: JEFF-4T2.

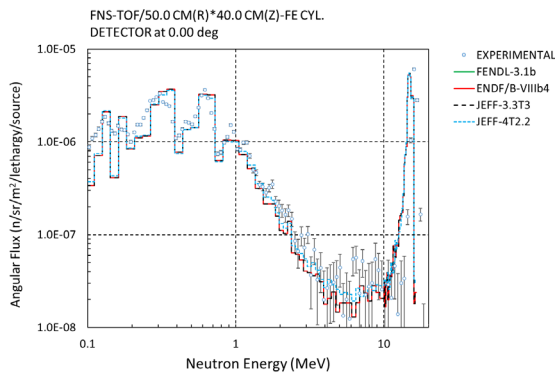


Figure 60. Angular neutron leakage spectra at 0 degrees for the 40CM(Z) FNS-TOF iron FNS-TOF experiment: JEFF-4T2.

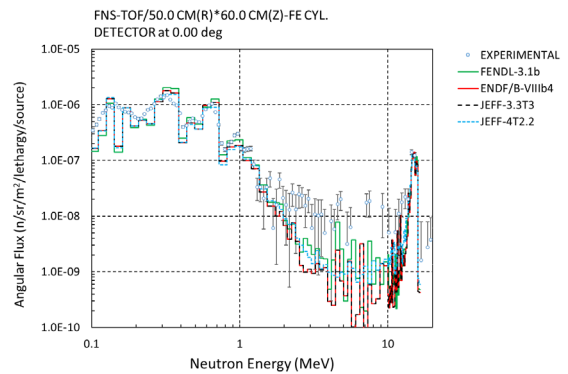


Figure 61. Angular neutron leakage spectra at 0 degrees for the 60CM(Z) FNS-TOF iron FNS-TOF experiment: JEFF-4T2.

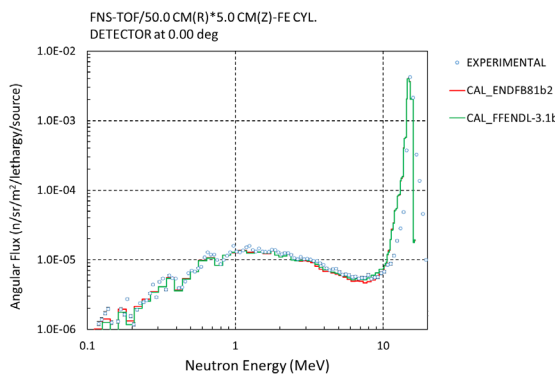


Figure 62. Angular neutron leakage spectra at 0 degrees for the 5CM(Z) FNS-TOF iron FNS-TOF experiment: ENDF/B-VIII.1b2.

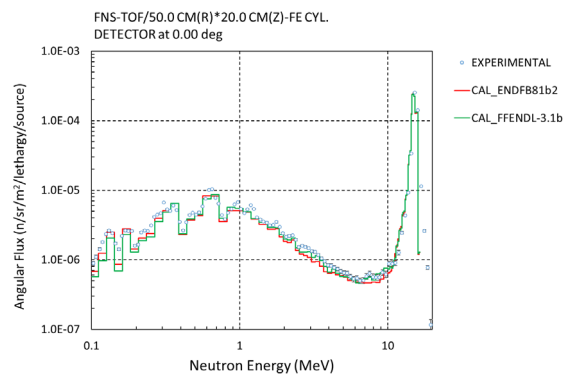


Figure 63. Angular neutron leakage spectra at 0 degrees for the 20CM(Z) FNS-TOF iron FNS-TOF experiment: ENDF/B-VIII.1b2.

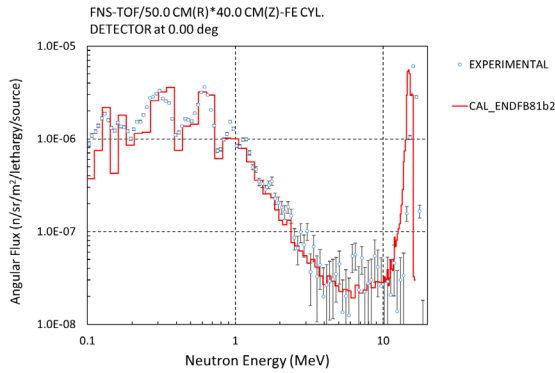


Figure 64. Angular neutron leakage spectra at 0 degrees for the 40CM(Z) FNS-TOF iron FNS-TOF experiment: ENDF/B-VIII.1b2.

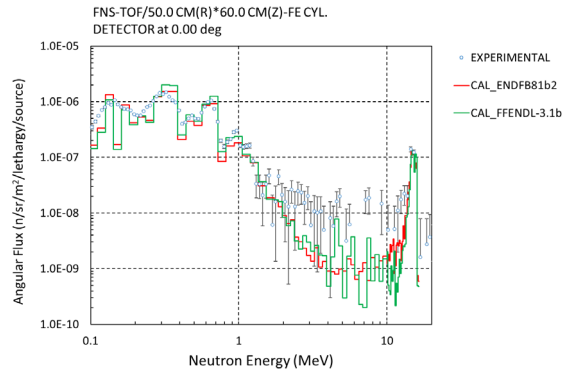


Figure 65. Angular neutron leakage spectra at 0 degrees for the 60CM(Z) FNS-TOF iron FNS-TOF experiment: ENDF/B-VIII.1b2.

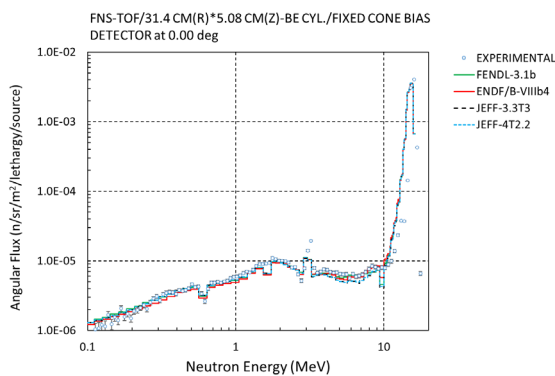


Figure 66. Angular neutron leakage spectra at 0 degrees for the 5.08CM(Z) FNS-TOF beryllium FNS-TOF experiment: : JEFF-4T2.

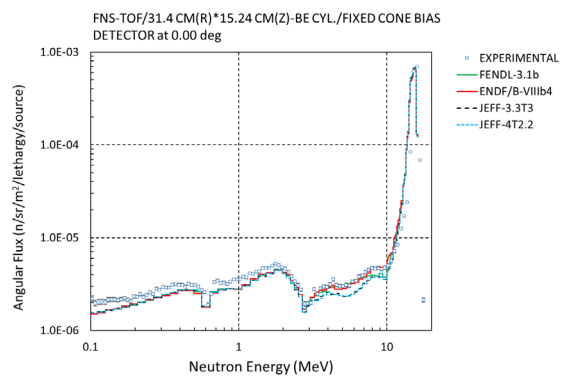


Figure 67. Angular neutron leakage spectra at 0 degrees for the 15.24CM(Z) FNS-TOF beryllium FNS-TOF experiment: : JEFF-4T2.

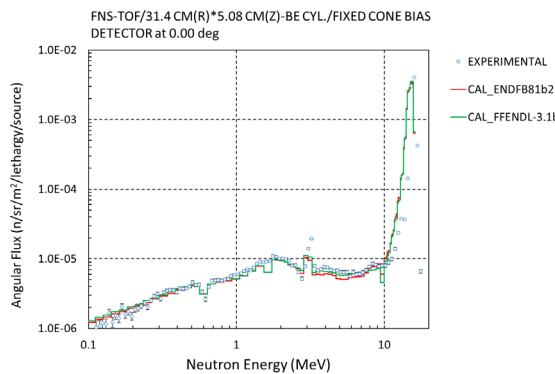


Figure 68. Angular neutron leakage spectra at 0 degrees for the 5.08CM(Z) FNS-TOF beryllium FNS-TOF experiment: ENDF/B-VIII.1b2.

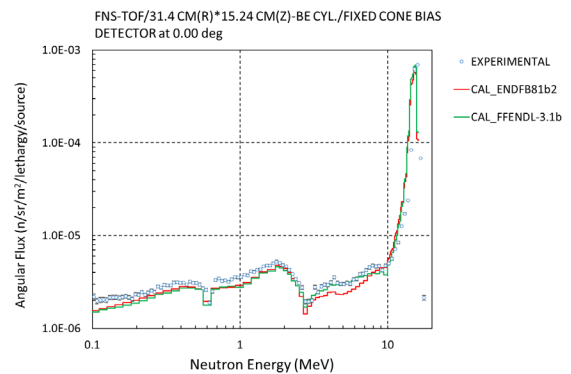


Figure 69. Angular neutron leakage spectra at 0 degrees for the 15.24CM(Z) FNS-TOF beryllium FNS-TOF experiment: ENDF/B-VIII.1b2.

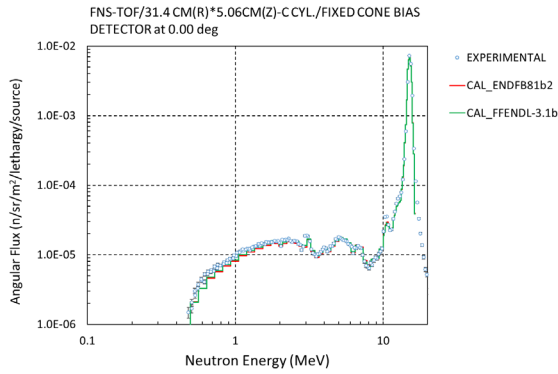


Figure 70. Angular neutron leakage spectra at 0 degrees for the 5.06CM(Z) FNS-TOF carbon FNS-TOF experiment: ENDF/B-VIII.1b2.

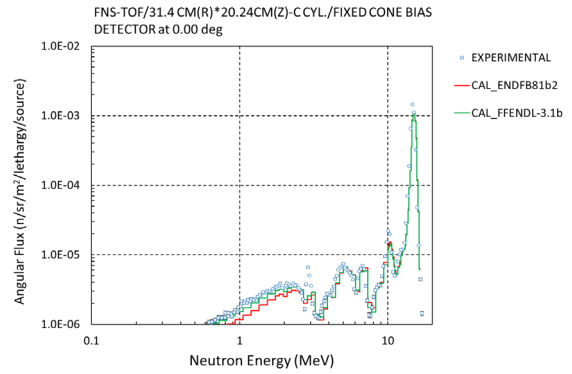


Figure 71. Angular neutron leakage spectra at 0 degrees for the 20.24CM(Z) FNS-TOF carbon FNS-TOF experiment: ENDF/B-VIII.1b2.

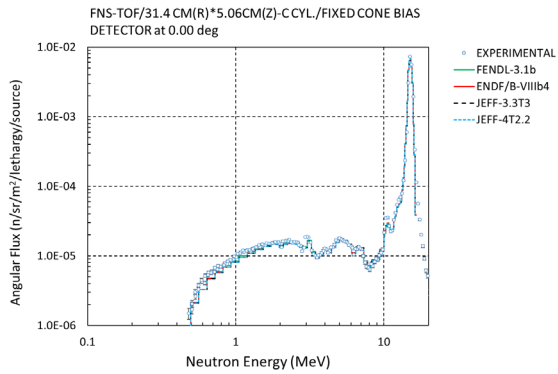


Figure 72. Angular neutron leakage spectra at 0 degrees for the 5.06CM(Z) FNS-TOF carbon FNS-TOF experiment: JEFF-4T.

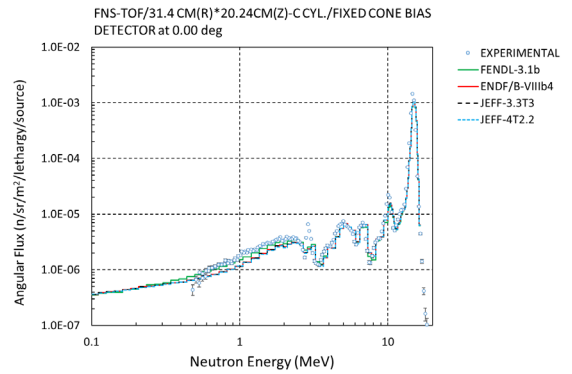


Figure 73. Angular neutron leakage spectra at 0 degrees for the 20.24CM(Z) FNS-TOF carbon FNS-TOF experiment: JEFF-4T.

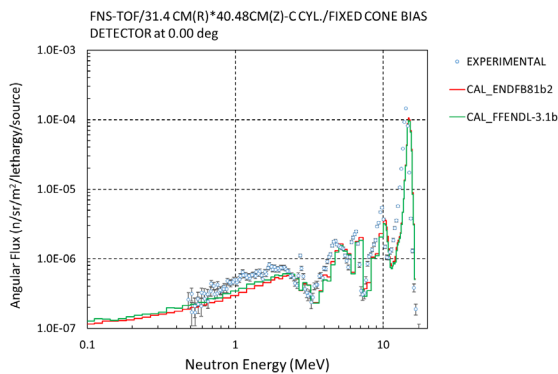


Figure 74. Angular neutron leakage spectra at 0 degrees for the 40.48CM(Z) FNS-TOF carbon FNS-TOF experiment: ENDF/B-VIII.1b2.

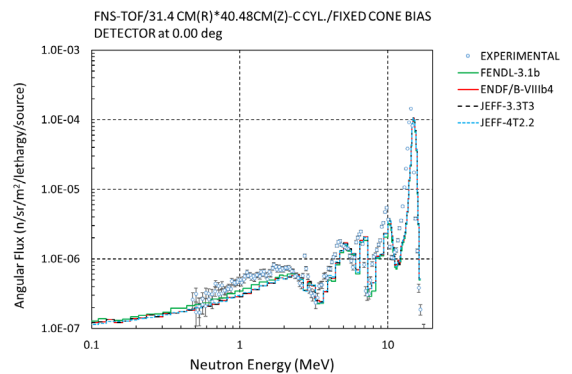


Figure 75. Angular neutron leakage spectra at 0 degrees for the 40.48CM(Z) FNS-TOF carbon FNS-TOF experiment: JEFF-4T.

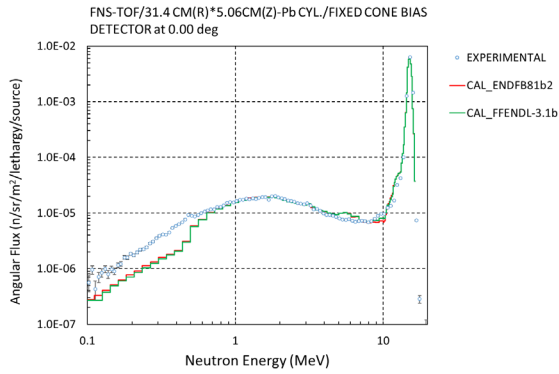


Figure 76. Angular neutron leakage spectra at 0 degrees for the 5.06CM(Z) FNS-TOF lead FNS-TOF experiment: ENDF/B-VIII.1b2.

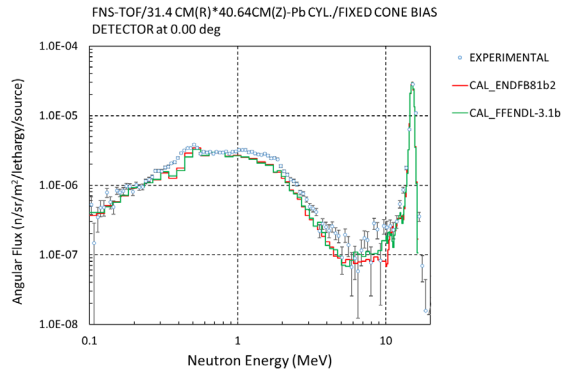


Figure 77. Angular neutron leakage spectra at 0 degrees for the 40.64CM(Z) FNS-TOF lead FNS-TOF experiment: ENDF/B-VIII.1b2.

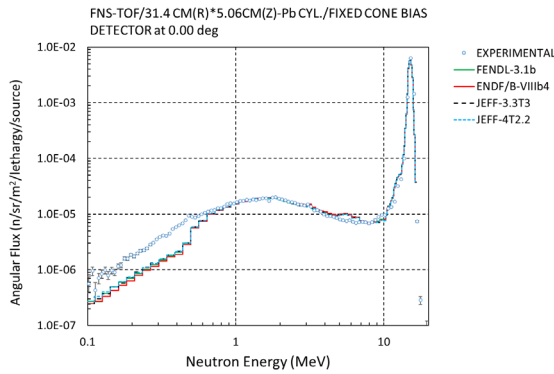


Figure 78. Angular neutron leakage spectra at 0 degrees for the 5.06CM(Z) FNS-TOF lead FNS-TOF experiment: JEFF-4T2.

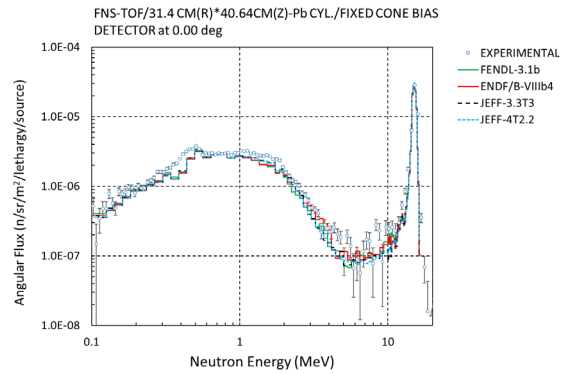


Figure 79. Angular neutron leakage spectra at 0 degrees for the 40.64CM(Z) FNS-TOF lead FNS-TOF experiment: JEFF-4T2.

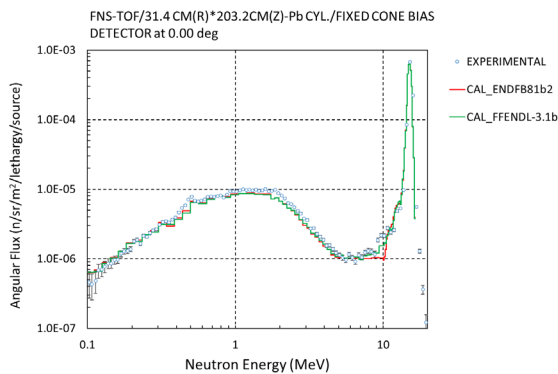


Figure 80. Angular neutron leakage spectra at 0 degrees for the 203.2CM(Z) FNS-TOF lead FNS-TOF experiment: ENDF/B-VIII.1b2.

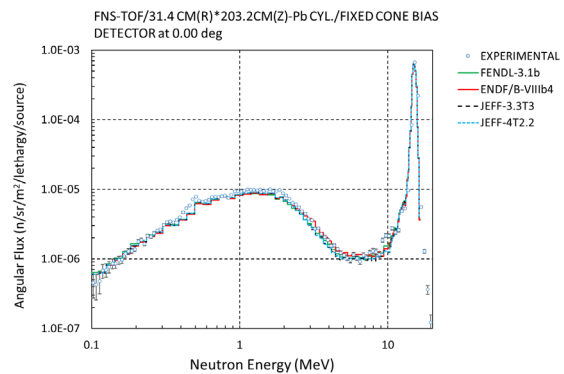


Figure 81. Angular neutron leakage spectra at 0 degrees for the 203.2CM(Z) FNS-TOF lead FNS-TOF experiment: JEFF-4T2.

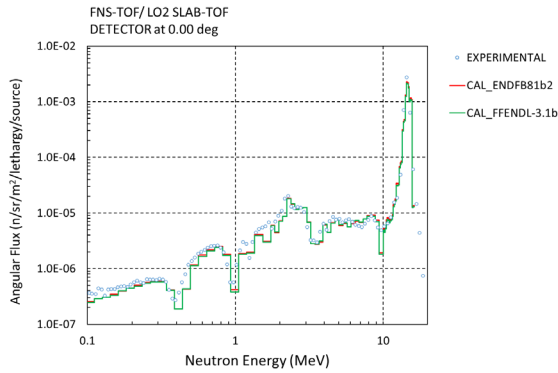


Figure 82. Angular neutron leakage spectra at 0 degrees for the SLAB FNS-TOF oxygen FNS-TOF experiment: ENDF/B-VIII.1b2.

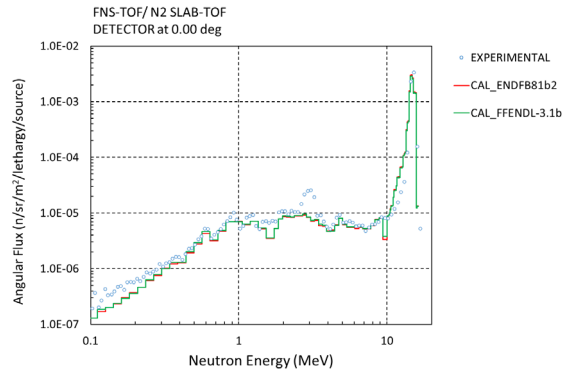


Figure 83. Angular neutron leakage spectra at 0 degrees for the SLAB FNS-TOF nitrogen FNS-TOF experiment: ENDF/B-VIII.1b2.

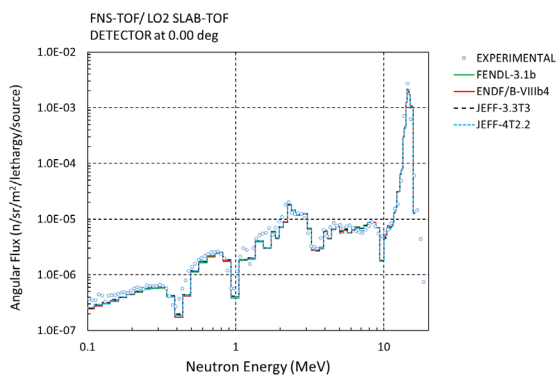


Figure 84. Angular neutron leakage spectra at 0 degrees for the SLAB FNS-TOF oxygen FNS-TOF experiment: JEFF-4T2.

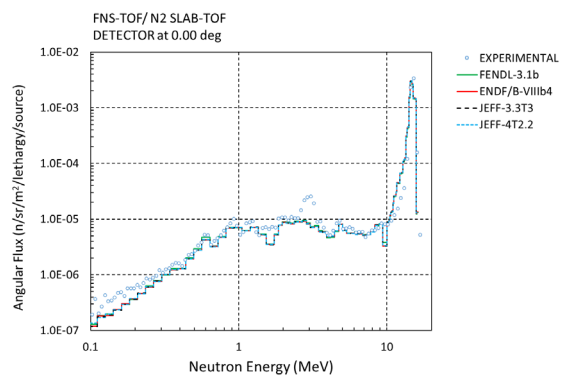


Figure 85. Angular neutron leakage spectra at 0 degrees for the SLAB FNS-TOF nitrogen FNS-TOF experiment: JEFF-4T2.

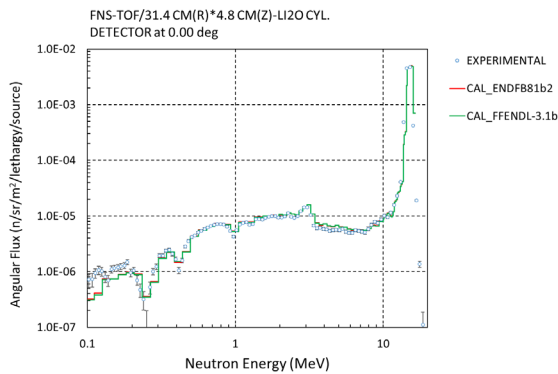


Figure 86. Angular neutron leakage spectra at 0 degrees for the 4.08CM(Z) FNS-TOF Li2O FNS-TOF experiment: ENDF/B-VIII.1b2.

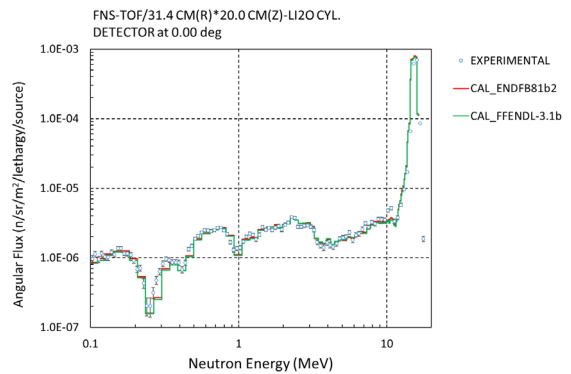


Figure 87. Angular neutron leakage spectra at 0 degrees for the 20.00CM(Z) FNS-TOF Li2O FNS-TOF experiment: ENDF/B-VIII.1b2.

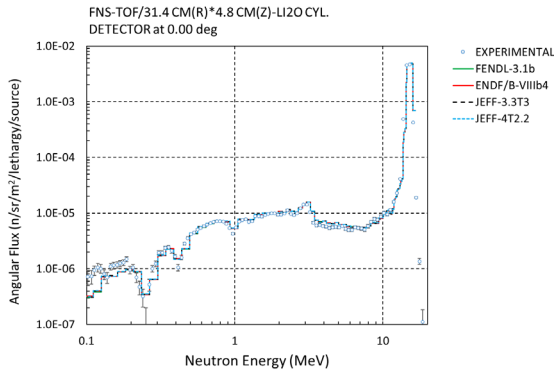


Figure 88. Angular neutron leakage spectra at 0 degrees for the 4.08CM(Z) FNS-TOF Li2O FNS-TOF experiment: JEFF-4T2.

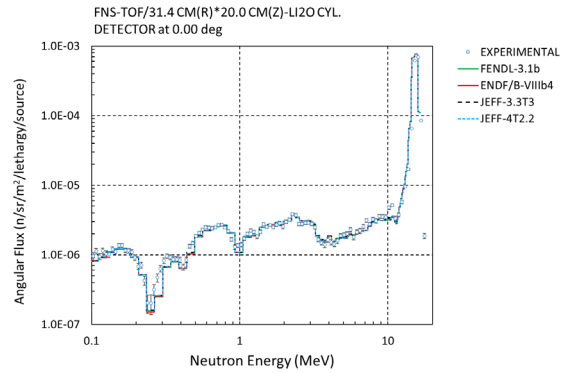


Figure 89. Angular neutron leakage spectra at 0 degrees for the 20.00CM(Z) FNS-TOF Li2O FNS-TOF experiment: JEFF-4T2.

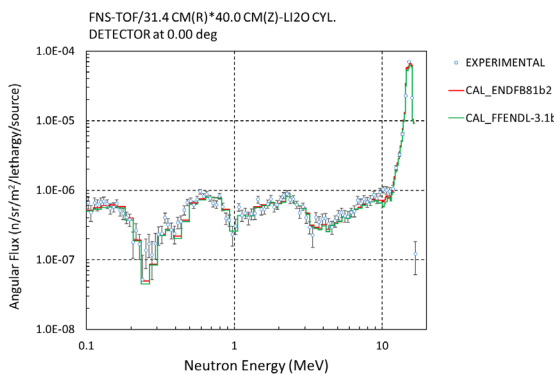


Figure 90. Angular neutron leakage spectra at 0 degrees for the 40.00CM(Z) FNS-TOF Li2O FNS-TOF experiment: ENDF/B-VIII.1b2.

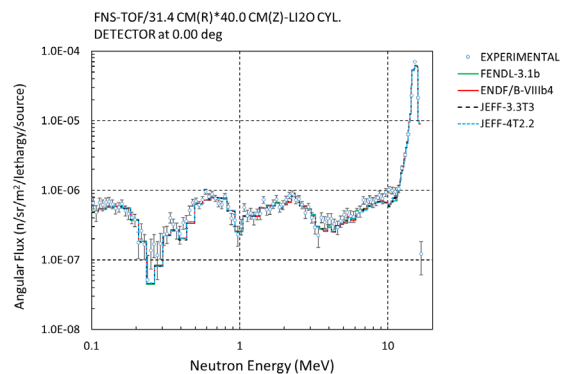


Figure 91. Angular neutron leakage spectra at 0 degrees for the 40.00CM(Z) FNS-TOF Li2O FNS-TOF experiment: JEFF-4T2.

6.3.2. OKTAVIAN

The second time-of-flight (TOF) shielding and transmission experiments selected is the OKTAVIAN/ToF spheres that used a 14-MeV dT neutron source [Takahashi, 1987].

Figure 92 shows a sketch of the OKTAVIAN pulsed sphere Type-I.

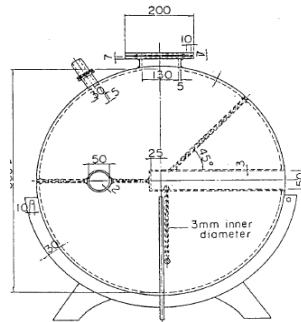


Figure 92. Example of OKTAVIAN pulsed sphere 61 cm: Type I.

For OKTAVIAN, fifteen validation studies were carried out for different materials. Table 30 shows a list of the OKTAVIAN Benchmarks included in the mentioned UPM distribution.

Table 30. OKTAVIAN ToF Benchmarks (15 cases)

Ref.: F. Maekawa et al., Collection of Exper. Data for Fusion Neutronics Benchmark, JAERI, 1994.

Geometry			
Type-I 61 cm diameter vessel	Type-II 40 cm diameter vessel	Type-III 60 cm diameter vessel	Type-IV 28 cm diameter vessel
Cu	Al	Si	Nb
LiF	As		
Mn	Co		
Mo	Cr		
Zr	Se		
	Teflon		
	Ti		
	W		

Figure 93 to Figure 120 show results obtained for different ToF-experiments at OKTAVIAN showing neutron leakage spectra for different nuclear data evaluations. Here the performance of JEFF-3.3, FENDL-3.1b and ENDF/B-VIII.0 is compared, jointly with different beta releases for ENDF/B-VIII.1 and JEFF-4.0, with the experimental data.

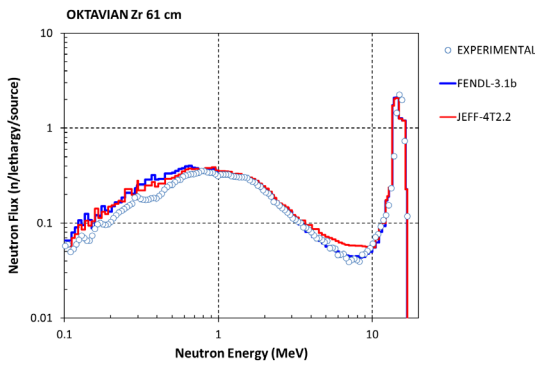


Figure 93. Neutron leakage for the OKTAVIAN Zr-61cm: JEFF-4T2.

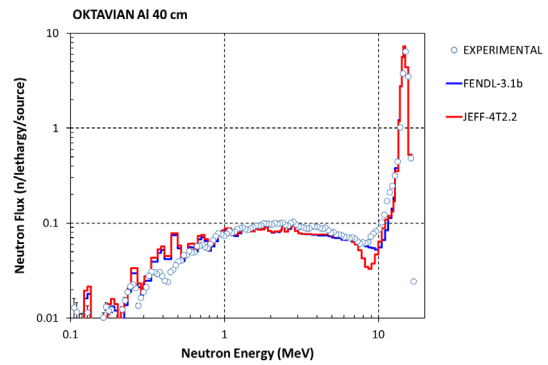


Figure 94. Neutron leakage for the OKTAVIAN Al-40cm: JEFF-4T2.

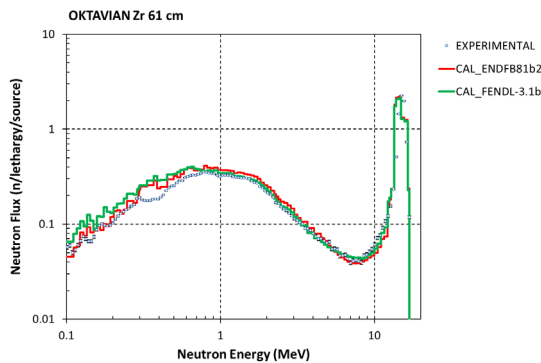


Figure 95. Neutron leakage for the OKTAVIAN Zr-61cm: ENDF/B-VIII.1b2.

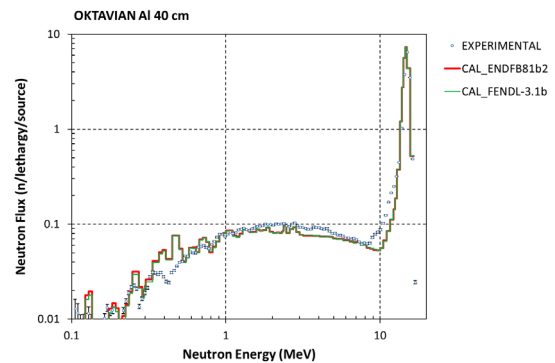


Figure 96. Neutron leakage for the OKTAVIAN Al-40cm: ENDF/B-VIII.1b2.

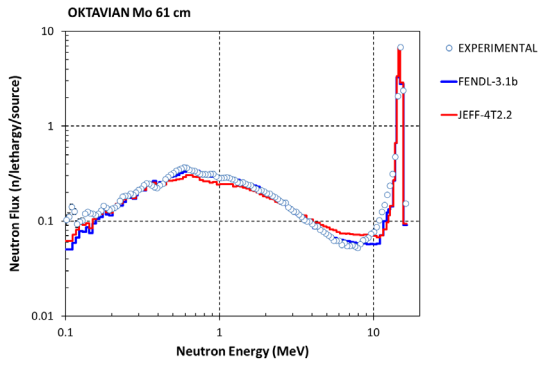


Figure 97. Neutron leakage for the OKTAVIAN Mo-61cm: JEFF-4T2.

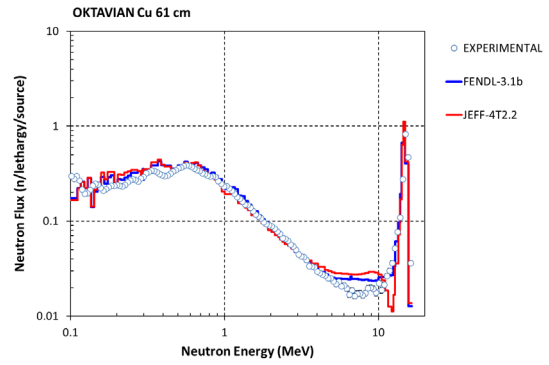


Figure 98. Neutron leakage for the OKTAVIAN Cu-61cm: JEFF-4T2.

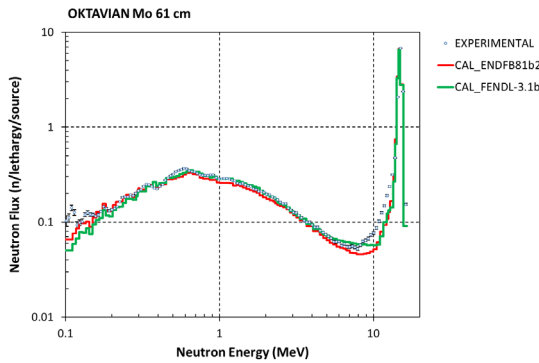


Figure 99. Neutron leakage for the OKTAVIAN Mo-61cm: ENDF/B-VIII.1b2.

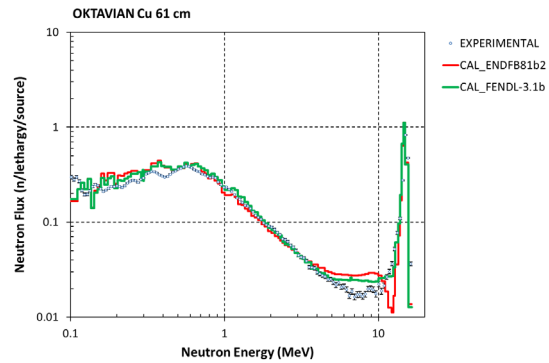


Figure 100. Neutron leakage for the OKTAVIAN Cu-61cm: ENDF/B-VIII.1b2.

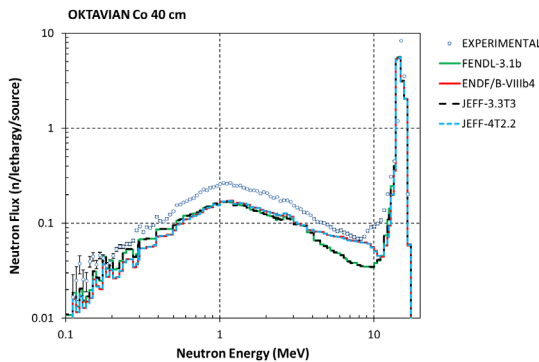


Figure 101. Neutron leakage for the OKTAVIAN Co-40cm: JEFF-4T2.

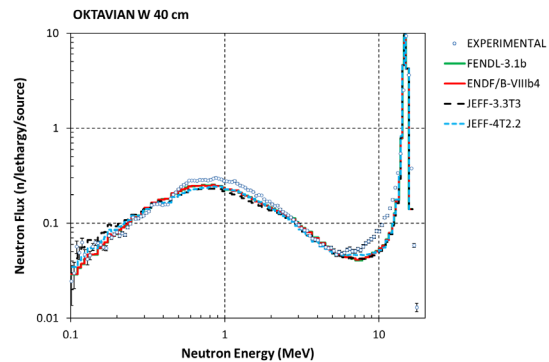


Figure 102. Neutron leakage for the OKTAVIAN W-40cm: JEFF-4T2.

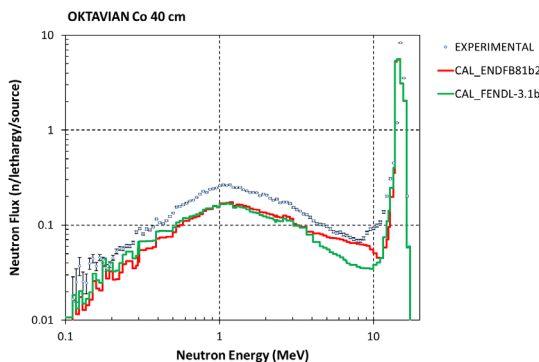


Figure 103. Neutron leakage for the OKTAVIAN Co-40cm: ENDF/B-VIII.1b2.

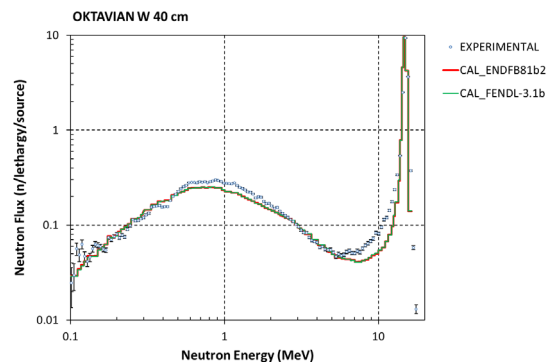


Figure 104. Neutron leakage for the OKTAVIAN W-40cm: ENDF/B-VIII.1b2.

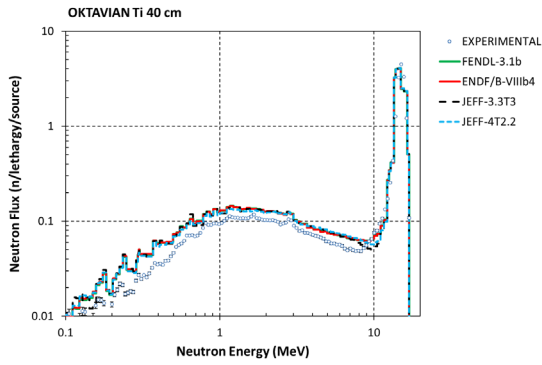


Figure 105. Neutron leakage for the OKTAVIAN Ti-40cm: JEFF-4T2.

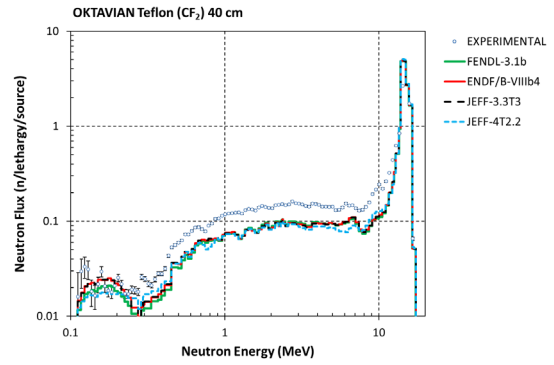


Figure 106. Neutron leakage for the OKTAVIAN Teflon-40cm: JEFF-4T2.

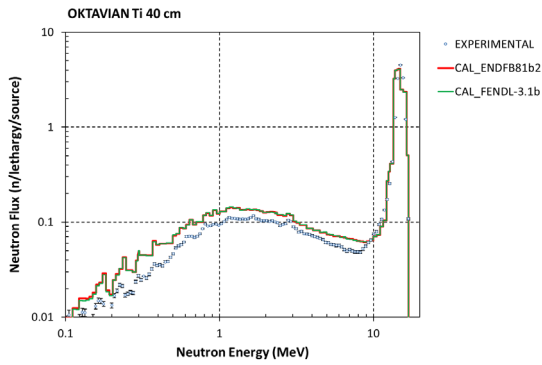


Figure 107. Neutron leakage for the OKTAVIAN Ti-40cm: ENDF/B-VIII.1b2.

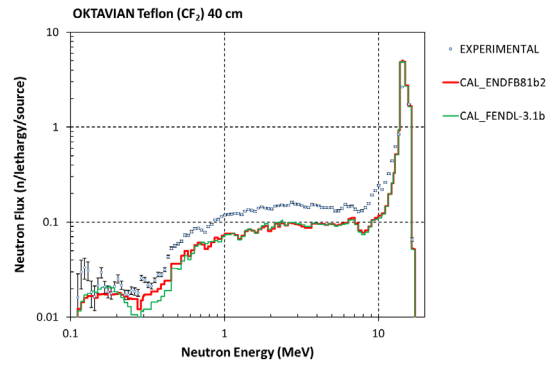


Figure 108. Neutron leakage for the OKTAVIAN Teflon-40cm: ENDF/B-VIII.1b2.

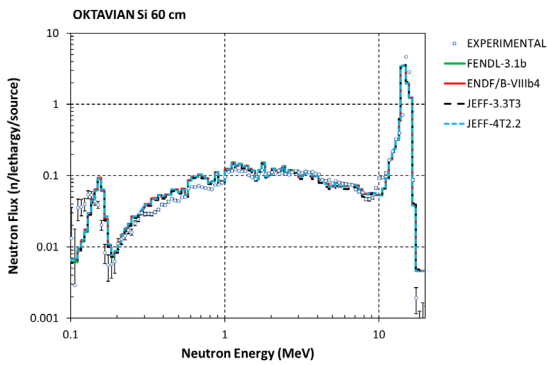


Figure 109. Neutron leakage for the OKTAVIAN Si-60cm: JEFF-4T2.

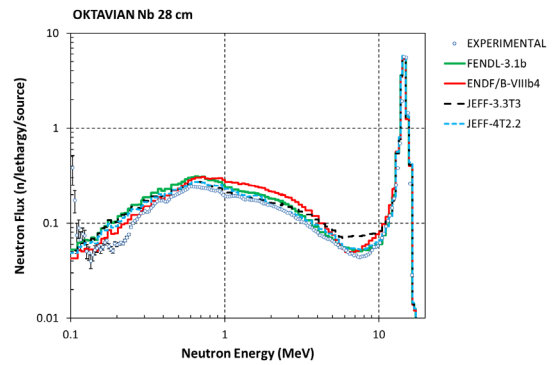


Figure 110. Neutron leakage for the OKTAVIAN Nb-28cm: JEFF-4T2.

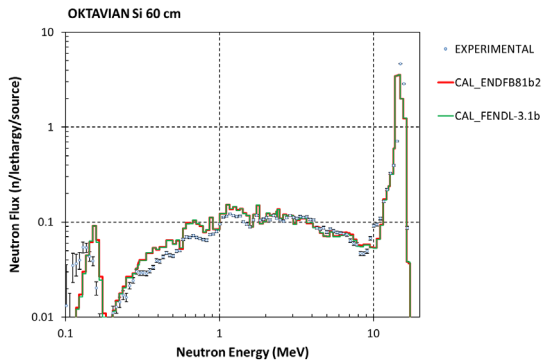


Figure 111. Neutron leakage for the OKTAVIAN Si-60cm: ENDF/B-VIII.1b2.

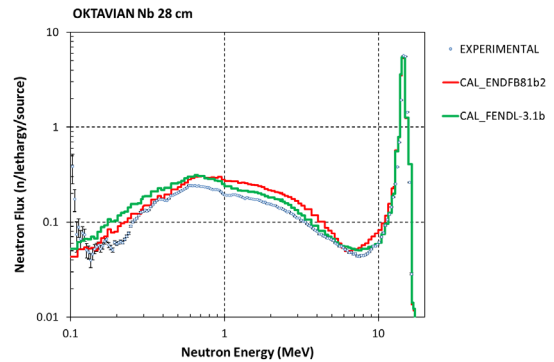


Figure 112. Neutron leakage for the OKTAVIAN Nb-28cm: ENDF/B-VIII.1b2.

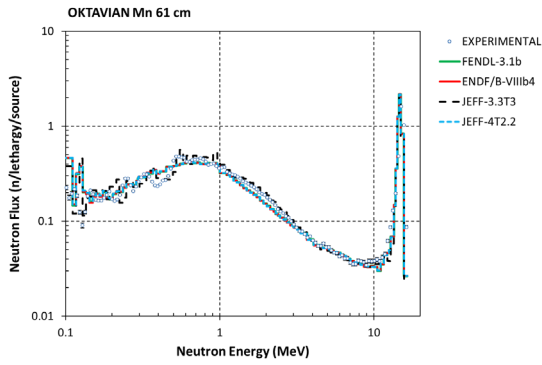


Figure 113. Neutron leakage for the OKTAVIAN Mn-61cm: JEFF-4T2.

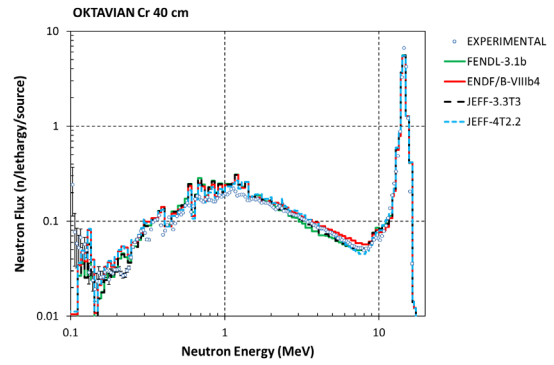


Figure 114. Neutron leakage for the OKTAVIAN Cr-40cm: JEFF-4T2.

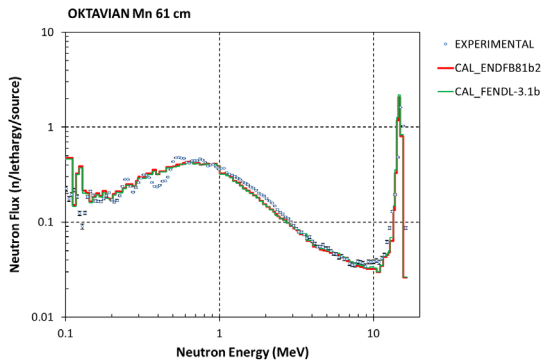


Figure 115. Neutron leakage for the OKTAVIAN Mn-61cm: ENDF/B-VIII.1b2.

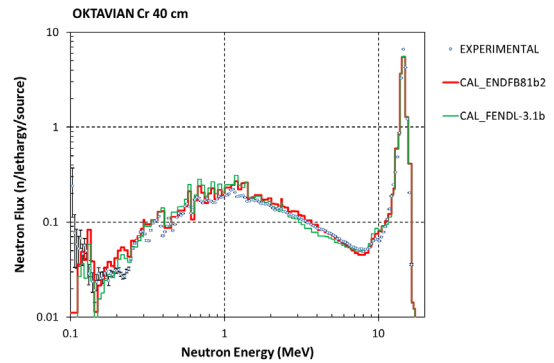


Figure 116. Neutron leakage for the OKTAVIAN Cr-40cm: ENDF/B-VIII.1b2.

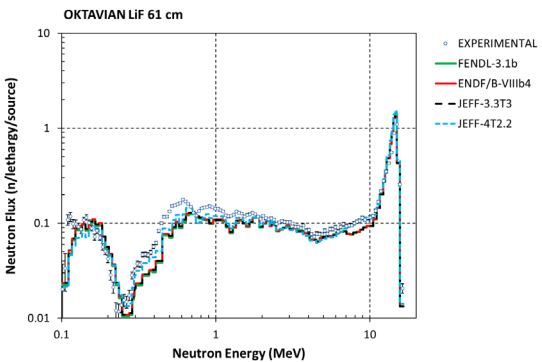


Figure 117. Neutron leakage for the OKTAVIAN LiF-61cm: JEFF-4T2.

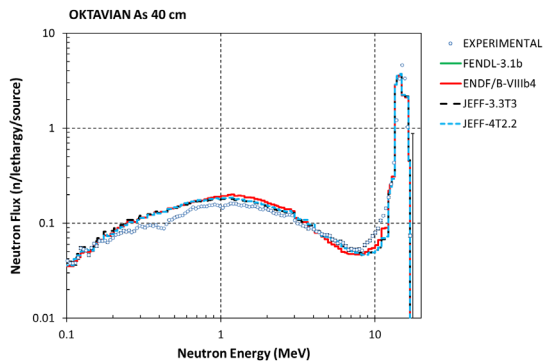


Figure 118. Neutron leakage for the OKTAVIAN As-40cm: JEFF-4T2.

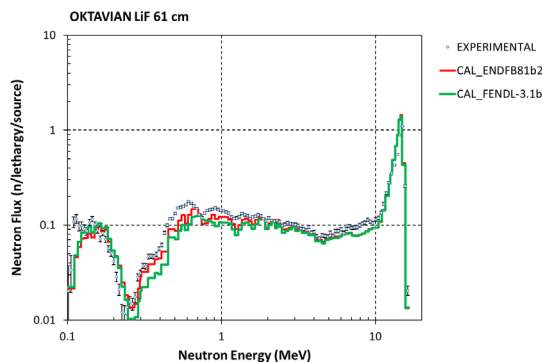


Figure 119. Neutron leakage for the OKTAVIAN LiF-61cm: ENDF/B-VIII.1b2.

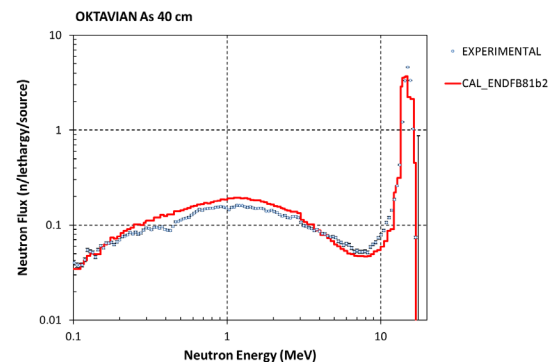


Figure 120. Neutron leakage for the OKTAVIAN As-40cm: ENDF/B-VIII.1b2.

6.4. Neutron transmission experiments in ICSBEP: FUND-JINR-1/E-MULT-TRANS-001 (UPM)

Finally, neutron transmission experiments for ^{235}U included in the ICSBEP Handbook [FUND-JINR-1/E-MULT-TRANS-001, 2019] were also analysed. These benchmarks can give alternative insights into nuclear data.

These ICSBEP/FUND-JINR-1/E-MULT-TRANS-001 experiments can reveal trends in the α -value ($\alpha = \sigma_{\text{capture}} / \sigma_{\text{fission}}$) characterized by different self-shielded and unshielded experiments [Cabellos, 2020b] [IAEA/INDEN-Nov 2020].

Table 31 shows the selected number of ^{235}U samples used in the Benchmark with different thickness.

Table 31. Samples of highly enriched uranium for FUND-JINR-1/E-MULT-TRANS-001: ^{235}U

Table 1.3-2. Samples of Highly Enriched Uranium.

Sample No.	1	2	3	4	5	6	7	8
Composition	2× U(90) t	3× U(90) t	4× U(90) t	8× U(90) t	1× U(90)	2× U(90)	4× U(90)	8× U(90)
Thickness, mm	~0.6	~0.9	~1.2	~2.4	~5	~10	~20	~40
Thickness, atoms/barn (Reference 2)	0.002574	0.003861	0.005148	0.01029	0.02145	0.0429	0.0858	0.1716

Figure 121 to Figure 124 show results obtained for samples 1 and 7. Here the performance of ENDF/B-VII.1, JEFF-3.3 and ENDF/B-VIII.0 is compared, jointly with different beta releases for JEFF-4.0, with the experimental data for the ^{235}U total and fission transmission.

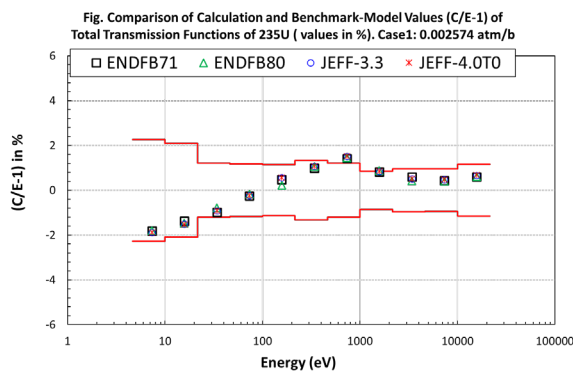


Figure 121. Values (C/E-1) in % of ^{235}U -Total Transmission Function for sample 1(0.002574 atm/b).

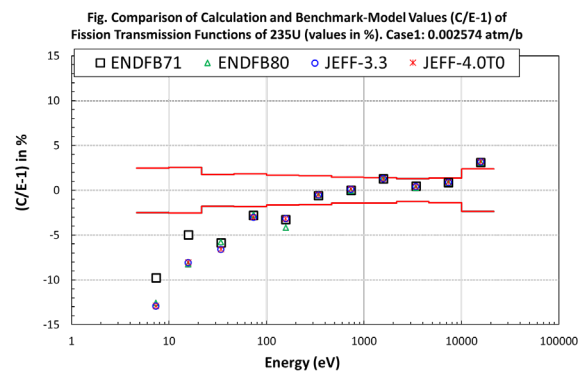


Figure 122. Values (C/E-1) in % of ^{235}U -Fission Transmission Function for sample 1(0.002574 atm/b).

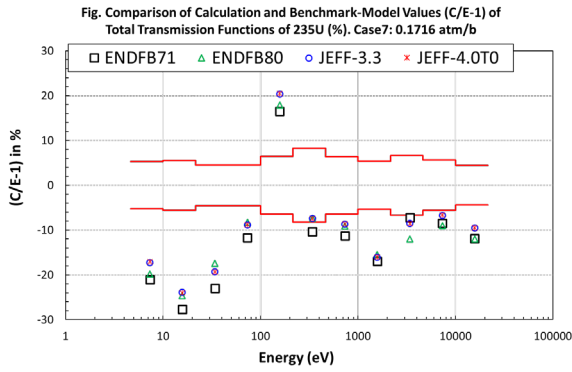


Figure 123. Values $(C/E-1)$ in % of ^{235}U -Total Transmission Function for sample 7(0.17160 atm/b).

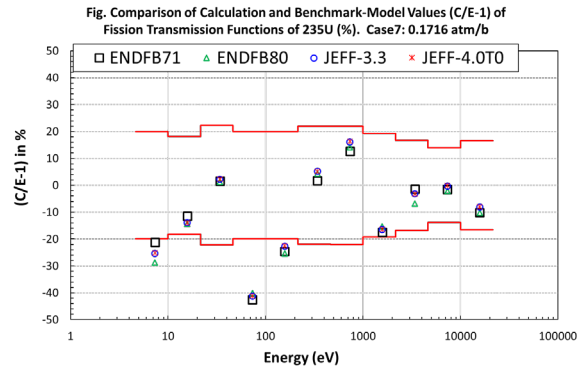


Figure 124. Values $(C/E-1)$ in % of ^{235}U -Fission Transmission Function for sample 7(0.17160 atm/b).

Therefore, transmission benchmarks provide insights for ^{235}U nuclear data in energy ranges differing from criticality applications.

7. Summary and Conclusions

A selection of reactor physics and shielding benchmark experiments was done by UPM, CEA/DES, JSI, UKAEA and NRG with the aim to test recent nuclear data evaluations. Concerning reactors, the selected benchmarks covered advanced LMFR reactors, thermal experimental reactors and commercial Light-Water Reactors. Regarding shielding benchmarks, Time-of-Flight integral benchmarks and neutron transmission experiments were analyzed.

The comparison between benchmark values and calculated values using recent evaluations generally indicates a better performance of JEFF-4T3 compared to JEFF-3.3. However, it suggests the need for revising some nuclear data. The following general conclusions can be drawn, with detailed conclusions on specific nuclear data needs compiled in Deliverable D5.9:

- For the liquid-metal fast reactors examined, the performance of JEFF-4T3 is better to that of JEFF-3.3. Nevertheless, the overall best agreement with the benchmark values correspond to ENDF/B-VII.1. The main contributors to k-eff deviations of JEFF-4T3 with respect to ENDF/B-VII.1 are ^{239}Pu and ^{238}U isotopes, with lots of opposite contributions. Impact of elastic cross-sections and elastic angular distributions for those isotopes caught attention for some benchmarks.
- For thermal spectrum benchmarks, results using JEFF-4T3 are in good agreement with the benchmark values taking into account the uncertainty margins, being the trends of C/E deviations as a function of temperature smaller than for JEFF-3.3.
- LWR simulations are very challenging and computationally expensive for nuclear data validation, as full-core calculations involve multi-physics phenomena (neutronics, thermal-hydraulic, and fuel behavior), as well as multi-scale phenomena (a two-step industrial approach) that may obscure the real impact of nuclear data. Additionally, LWR measurements are proprietary data, which adds difficulty to their use in nuclear data validation. Nevertheless, they are a valuable source of information and relevant conclusions on the performance of JEFF-x evaluations were drawn concerning:
 - Prediction of the reactivity loss along the cycle burnup of a PWR. A larger reactivity loss along burnup is predicted by JEFF-3.3 and JEFF-4x compared to ENDF/B-VII.1. The main responsible isotopes are ^{235}U , ^{238}U , ^{239}Pu , ^{240}Pu and ^{241}Pu . Additionally, some fission products can also be relevant in predicting the reactivity change during depletion.
 - Prediction of the fuel isotopic concentrations for consecutive burnup cycles of a PWR, suggesting the need of revision for capture cross sections of ^{239}Pu and ^{240}Pu in specific energy regions of the thermal range.
- Finally, different shielding benchmarks for nuclear data validation were examined. For iron, a degradation in C/E agreement was noted with JEFF-3.3 (and ENDF/B-VIII.0) compared to older evaluations, but his improved notably with recent JEFF-4T. Results for Time-of-Flight integral experiments provided additional insights above 2 MeV, that is, above the neutron energy of criticality benchmarks. Furthermore, neutron transmission benchmarks also gave valuable observations for ^{235}U nuclear data.

8. Acknowledgements

The ICSBEP, IRPHEP and SINBAD databases have been obtained through the Computer Programs Services of OECD/NEA Nuclear Data Bank; MCNP code through the Radiation Safety Information Computational Center (RSICC) of Oak Ridge National Laboratory (ORNL, USA), and SCALE6.3beta through Oak Ridge National Laboratory.

9. References

- [Ahnert, 1988] C. Ahnert, J.M. Aragonés et al., 1988. Validation of the pressurized water reactor core analysis system SEANAP. Nucl. Sci. Eng. 100, 305.
- [Alcouffe, 2009] R. E. Alcouffe and R. S. Baker. "PARTISN: A Time-Dependent, Parallel Neutral Particle Transport Code System", LA-UR-08-07258 (March 2009).
- [Ardura, 2019] A. Ardura et al. Comparison of JEFF-3.3 and ENDF/B-VIII.0 in PWR simulations, JEFF Nuclear Data Week, April 2019, JEFFDOC-1968.
- [Astigarraga, 2022] M. Astigarraga, O. Cabellos, Benchmarking and Validation with JEFF-4T2.2, JEFF Nuclear Data Week, April 25-28, 2022, JEFFDOC-2239.
- [Cabellos, 2018] O. Cabellos, Upgraded SEANAP-PWR core simulator with JEFF-3.3: Impact of ND uncertainties for PWR cycle operation, JEFF Nuclear Data Week, April 2018, JEFFDOC-1917.
- [Cabellos, 2020a] O. Cabellos, Feedbacks on JEFF-3.3 Evaluation: Uncertainty in keff for some ICSBEP Outliers, PWR Critical Boron Letdown Curve and Additional integral data testing using reaction rates in critical assemblies, JEFF Nuclear Data Week, April 2020, JEFFDOC-1991.
- [Cabellos, 2020b] O. Cabellos, M. García-Hormigos, B. Moreno and S. Sánchez-Fernández, The importance of using different integral benchmarks to provide valuable feedbacks to the evaluation process, JEFF Meeting and JEFF-CG, November 2020, JEFFDOC-2015.
- [Cabellos, 2021a] O. Cabellos, Overview of Processing, Verification and Benchmarking activities at UPM, JEFF Nuclear Data Week, April 28, 2021, JEFFDOC-2041.
- [Cabellos, 2021b] O. Cabellos, A. Jiménez-Carrascosa, N. García-Herranz, G. de Alcázar, Overview of Processing, Testing of the JEFF-3.3 with IRPhEP/LWR KRITZ Benchmarks, JEFF Nuclear Data Week, November 24, 2021, JEFFDOC-2091.
- [Cabellos, 2022] Course Handbook "Nuclear Data for Energy and non-Energy Applications", Great Pioneer EU project, 2022.
- [Cabellos, 2023] O. Cabellos, Feedback on ENDF/B-VIII.1b2 on a selection of Benchmarks, CSEWG Meeting, November, 2023.
- [Cervantes, 2024] E.Y. García-Cervantes, L. Buiron, N. García-Herranz, A. Jiménez Carrascosa, Y. Cao, Z.I. Böröczki, Status of the SEFOR benchmark Phase I: isothermal tests, BEPU 2024, Lucca, Italy, May 19-24, 2024.
- [FENDL3.2-2024] G. Schnabel, et al., "FENDL: A library for fusion research and applications", Nuclear Data Sheets, 193 (2024) 1–78 <https://doi.org/10.1016/j.nds.2024.01.001>
- [FUND-JINR-1/E-MULT-TRANS-001, 2019] International Handbook of Evaluated Criticality Safety Benchmark Experiments, OECD NEA (2019): "Neutron Transmission Through Samples of Depleted Uranium, Highly-Enriched Uranium, and Plutonium for Determination of Resonance Self-Shielding of Total Cross Section and Fission Cross Section of ²³⁸U, ²³⁵U, and ²³⁹Pu."
- [García-Herranz, 2022] García-Herranz N. et al., UPM contribution to D5.2: Report on ESRF, ASTRID and ALFRED sensitivity and impact studies. Appendix of D5.2 SANDA, October 2022.
- [García-Herranz, 2023] García-Herranz N., et al. On the use of SEFOR experiments for testing JEFF4T2.2. JEFF Nuclear Data Week, 24-28 April 2023, JEFFDOC2238.
- [García-Herranz, 2024] García-Herranz N., et al. Benchmarking of JEFF4T3 for liquid metal fast reactors. JEFF Nuclear Data Week, 22-26 April 2024, JEFFDOC2352.
- [Goorley, 2004] J. T. Goorley, J. S. Bull, F. B. Brown. Release of MCNP5_RSICC_1.30. Los Alamos National Laboratory Presentation LA-UR-04-8086. Los Alamos, NM, USA. 2004.

- [Goorley, 2012] Goorley, T., James, M., Booth, T., Brown, F., Bull, J., Cox, L. J., ... Zukaitis, T. (2012). Initial MCNP6 Release Overview. Nuclear Technology, 180(3), 298–315. <https://doi.org/10.13182/NT11-135>.
- [Goorley, 2013] Goorley, T. et al., (2013). Initial MCNP6 Release Overview - MCNP6 version 1.0. LA-UR-13-22934. <https://doi.org/10.2172/1086758>.
- [IAEA/INDEN-Nov 2020] O. Cabellos, Indications from integral benchmarks on U-235, U-238 and Pu-239 evaluations, IAEA CM of the INDEN on Actinide Evaluation in the Resonance Region, 17-19 Nov 2020.
- [IAEA-TEC-DOC 815, 1995] IAEA-TEC-DOC 815 “In-Core Fuel Management Code Package Validation for PWRs”, 1995 <https://inis.iaea.org/collection/NCLCollectionStore/Public/26/077/26077395.pdf>
- [ICSBEP, 2020] International Criticality Safety Benchmark Evaluation Project (ICSBEP), OECD Nuclear Energy Agency, 2020, <https://doi.org/10.1787/7e0ebc50-en>.
- [IRPhEP, 2019] International Handbook of Evaluated Reactor Physics Benchmarks Experiments (IRPhEP), OECD Nuclear Energy Agency, 2019, number NEA No. 7497, 2019.
- [Ivanova, 2014] T.T. Ivanova, E. Ivanov, G. E. Bianchi, Establishment of Correlations for Some Critical and Reactor Physics Experiments, Nuclear Science and Engineering 178, 1–15 (2014).
- [Ivanova, 2017] T.T. Ivanova, E. Ivanov, I. Hill, Methodology and issues of integral experiments selection for nuclear data validation, EPJ Web of Conferences 146, 06002 (2017).
- [Jiménez-Carrascosa, 2020] A. Jiménez-Carrascosa *et al.*, Joint UPM and CIEMAT contribution: Progress on ESFR, WPEC Subgroup 46 (SG46) WebEx meeting, 11 November 2020 (<https://www.oecd-nea.org/download/wpec/sg46/meetings/2020-11/>)
- [Jiménez-Carrascosa, 2021] A. Jiménez-Carrascosa *et al.*, Impact of Doppler calculation in SEFOR Benchmark due to the differences between JEFF 3.3 and JEFF 3.1.1, JEFF Nuclear Data Week, JEFFDOC-2097, November 22-26, 2021.
- [Jiménez-Carrascosa, 2021b] A. Jiménez-Carrascosa *et al.*, Processing of JEFF ND libraries for the SCALE Code System and testing with criticality experiments, JEFF Nuclear Data Week, JEFFDOC-2107, November 22-26, 2021.
- [Jiménez-Carrascosa, 2022] A. Jiménez-Carrascosa *et al.*, Processing and benchmarking of JEFF-4T1 library in the frame of the SCALE Code System, JEFFDOC-2144, April 2022.
- [Jiménez-Carrascosa, 2024] A. Jiménez-Carrascosa *et al.*, Feedback on AMPX processing and benchmarking of JEFF-4T3 using SCALE, JEFF Nuclear Data Week, JEFFDOC2347, 22-25 April 2024.
- [Kodeli, 2009] Kodeli *et al.*, Analysis of the KRITZ Critical Benchmark Experiments, NENE2009.
- [Kodeli, 2021] I. Kodeli, E. Sartori, SINBAD – Radiation shielding benchmark experiments, ANE, Volume 159, 1 September 2021, 108254.
- [Kodeli, 2022] I. Kodeli, XSUN-2022/SUSD3D n/ γ sensitivity-uncertainty code package with recent JEFF-3.3 and ENDF/B-VIII.0 covariance data, EPJ Web of Conferences 281, 00013 (2023), CW2022, <https://doi.org/10.1051/epjconf/202328100013>
- [Kodeli, 2023a] I. Kodeli, Sensitivity of gamma flux to n/ γ nuclear data - example of KFK gamma leakage benchmark analysis, M & C 2023 - The Int. Conf. on Mathematics and Computational Methods Applied to Nuclear Science and Engineering, Niagara Falls, Ontario, Canada, August 13 - 17, 2023
- [Kodeli, 2023b] I. Kodeli, S. van der Marck, Consistency Among the Results of the ASPIS Iron88, PCA Replica, and PCA ORNL Benchmark Experiments, Nuclear Science and Engineering, (2023), DOI: <https://doi.org/10.1080/00295639.2023.2199673>
- [Maekawa, 2000] F. Maekawa, Y. Ikeda, Decay heat experiment on thirty-two fusion reactor relevant materials irradiated by 14-MeV neutrons. Fusion Eng. Des. 47(4), 377–388 (2000).

- [Maekawa, 2002] F. Maekawa, K. ichiro Shibata, M. Wada, Y. Ikeda, H. Takeuchi, Comprehensive activation experiment with 14-MeV neutrons covering most of naturally existing elements: 5 min irradiation experiment. *J. Nucl. Sci. Technol.* 39(sup2), 990–993 (2002).
- [MacFarlane, 2010] R.E. MacFarlane and A.C. Kahler, Methods for processing ENDF/B-VII with NJOY, *Nuclear Data Sheets* 111 (2010) 2739–2890
- [Mennerdahl, 2021] D. Mennerdahl, KRITZ-1-MK Critical Measurements at temperatures from 20 °C to 250 °C, *PHYSOR2020* (2021), *EPJ Web of Conferences* 247, 09028 (2021), <https://doi.org/10.1051/epjconf/202124709028>.
- [Mikityuk, 2017] K. Mikityuk *et al.*, *ESFR-SMART: New Horizon-2020 Project on SFR Safety*. AQ6 474 Proc. IAEA FR2017, Ekaterinburg (Russian Federation).
- [Muir, 2018] D.W. Muir, R.M. Boicourt, A.C. Kahler (Ed.), J.L. Conlin, W. Haeck, The NJOY nuclear data processing system, Version 2016, LANL Report LA-UR-17-20093 (2018)
- [Plompen, 2020] A. Plompen *et al.*, The joint evaluated fission and fusion nuclear data library, JEFF-3.3, *Eur. Phys. J. A.*, pp. 1-107 (2020).
- [Rearden, 2016] Rearden, B. T., and Jessee, M. A., 2016, “SCALE Code System,” Oak Ridge National Laboratory (ORNL), Oak Ridge, TN, p. 2747, Report No. ORNL/TM-2005/39, No. 6.2.3.
- [Rimpault, 2018] G. Rimpault *et al.*, Current Status and Perspectives of the OECD/NEA sub-group on Uncertainty Analysis in Modelling (UAM) for Design, Operation and Safety Analysis of SFRs (SFR-UAM), ANS Best Estimate Plus Uncertainty International Conference (BEPU 2018).
- [Santamarina, 2009] A. Santamarina, D. Bernard, P. Blaise, L. Erradi, P. Leconte, R. Le Tellier, C. Vaglio, J-F. Vidal, APOLLO2.8: A validated code package for PWR neutronics calculations *Advances in Nuclear Fuel Management IV (ANFM 2009)*, Hilton Head Island, South Carolina, USA, April 12-15, 2009, on CD-ROM, American Nuclear Society, LaGrange Park, IL (2009), ANS2009
- [SINBAD, 2021] SINBAD database,, OECD/NEA, available online: <https://oecd-nea.org/science/wprs/shielding/sinbad/sinbadis.htm>
- [Talahashi, 1987] A. Takahashi, E. Ichimura, Y. Sasaki, H. Sugimoto, Double and single differential neutron emission cross sections at 14.1 mev. vol. 1. Osaka University Report OKTAVIAN A-87-03 (1987).
- [Ware, 2020] T. Ware, Pu-239 JEFF-3.3 data trends in MONK10 benchmark calculations, JEFDOC-1998, April 2020
- [Werner, 2018] Werner *et al.*, MCNP Version 6.2 Release Notes, LANL Report LA-UR-18-20808, 2018-02-05, 2018.
- [Wieselquist, 2020] W.A. Wieselquist, R.A. Lefebvre, M.A. Jessee, Editors. TSURFER: An adjustment code to determine biases and uncertainties in nuclear system responses by consolidating differential data and benchmark integral experiments, SCALE Manual, Version 6.2.4, April 2020, ORNL/TM-2005/39.
- [WPEC/SG47, 2019] O. Cabellos, “UPM contribution to WPEC/SG47” WPEC/SG47, June 24, 2019. OECD/NEA Headquarters, Boulogne-Billancourt, France (in-person).
- [WPEC-SG47,2022] I. Kodeli, M. Fleming, O. Cabellos, L. Leal, Y. Celik, Y. Ding, B. Jansky, D. Neudecker, E. Novak, S. Simakov, Y. Iwamoto, A. Valentine, Outcomes of WPEC SG47 on "Use of Shielding Integral Benchmark Archive and Database for Nuclear Data Validation", *EPJ Web of Conferences* 284, 15002 (2023), ND2022, <https://doi.org/10.1051/epjconf/202328415002>
- [Zwermann, 2022] W. Zwermann, I. Hill, Assessment of nuclear data libraries for fast reactor systems with MCNP and NDaST, *Annals of Nuclear Energy* 178 (2022) 109354.
- [Zwermann, 2024] W. Zwermann, MCNP inputs provided for SNEAK-7A, SNEAK-7B and ZPPR-13A Loading 24 (2024).